The Dissertation Committee for Emilio Alvarez II Certifies that this is the approved version of the following dissertation:

Hydrogen Determination in Chemically Delithiated Lithium Ion Battery Cathodes by Prompt Gamma Activation Analysis

Committee:

Arumugam Manthiram, Co-Supervisor

Sheldon Landsberger, Co-Supervisor

Steven R. Biegalski

Robert R. Greenberg

Erich A. Schneider

Hydrogen Determination in Chemically Delithiated Lithium Ion Battery Cathodes by Prompt Gamma Activation Analysis

by

Emilio Alvarez II, B.S., M.S.E.

Dissertation

Presented to the Faculty of the Graduate School of
The University of Texas at Austin
in Partial Fulfillment
of the Requirements
for the Degree of

Doctor of Philosophy

The University of Texas at Austin
August, 2007

Dedication

Para mis niñas, Daniella, Isabella, y Olivia.

Acknowledgements

First and foremost the author would like to gratefully acknowledge his co-supervisors Dr. Arumugam Manthiram and Dr. Sheldon Landsberger for their continual input and support throughout this project. The author would also like to express his gratitude to the rest of his Ph.D. committee members, Dr. Steven Biegalski, Dr. Robert Greenberg, and Dr. Erich Schneider for their valuable time and input concerning this work.

Also, further thanks are given to Dr. Landsberger for introducing the author to the Nuclear and Radiation and Engineering program and for always being in his corner and having confidence in him throughout his graduate years.

The author is also appreciative of newly appointed NETL Director Dr. Biegalski for always making himself available to discuss issues concerning work and life in general.

Special thanks are in order for Associate Director Sean O'Kelly for his valuable knowledge concerning all things NETL and for always taking the time to sit and chat about various topics. Thanks are also in order to Sean for acquiring the funds that supported part of this work and all of the author's Master's research work.

The author would like to thank the entire NETL reactor operations staff for their hard work and time spent running and maintaining the reactor facility. Thank you to Dr.

Donna O’Kelly for always finding a way to rearrange the reactor operations schedule in order to accommodate the author’s never ending requests for 8 hour, 950 kW days. Similarly, the author would like to express gratitude to the reactor operators, notably Mr. Jay Hedlund, Mr. Stephen Johnson, Mr. Michael Krause, Mr. Larry Welch, Mr. Art Wharton, and Mr. William Wilson for always willing to stay past 5:00 pm in order to help accomplish this work.

A special thank you is in order for Michael and Larry for always providing assistance on issues related to the maintenance of the beam port 3 facility and PGAA system throughout the author’s time as a graduate student.

The author would like to express his sincere gratitude and appreciation for the graduate students he has had the pleasure of working with and befriending over the last four years. In particular, the author would like to express his thanks to Mr. Tiruvannamalai Arunkumar, Dr. Jeh Won Choi, Dr. Wonchang Choi, Mr. Taylor Green, Mr. Derek Haas, Dr. Ki-Tae Lee, Mr. Dustin Reinert, Mr. George Sayre, and Mr. Scott Whitney for constantly providing positive energy at the work place and always offering whatever help they could provide regardless of the circumstances. Thank you to Mr. Rick Harrison for his help in improving the beam port 3 facility and his fresh ideas regarding PGAA.

The author wishes to extend his thanks to Dr. Richard Lindstrom, Dr. Elizabeth Mackey, and Dr. Zsolt Révay for always taking the time to pull from their vast knowledge and answer questions related to PGAA.

The author gratefully acknowledges the financial support provided by the DOE INIE program, the DOE NEER program, the Hispanic Scholarship Fund (General Motors Corporation Scholarship), and the John M. Scott Endowed Presidential Scholarship in

Mechanical Engineering. Without this funding, the author would have undoubtedly experienced a much more difficult trial during the compilation of this work.

Finally, the author would like to express his sincere gratitude to his family for their love, support, and unending words of encouragement. The author would like to thank both his mother and grandmother for reminding him to always follow his heart and to be humble in mind and spirit. The author will forever be thankful for the new light in his life, his two beautiful daughters Olivia and Isabella. The author is eternally grateful to his wife for her never ending motivation, patience, unconditional love, and inspiration through out this endeavor. He is forever indebted to her. The author would also like to thank God for giving him strength and patience so that he might be able to persistently press on.

Hydrogen Determination in Chemically Delithiated Lithium Ion Battery Cathodes by Prompt Gamma Activation Analysis

Publication No._____________

Emilio Alvarez II, Ph.D.
The University of Texas at Austin, 2007

Co-Supervisor: Arumugam Manthiram
Co-Supervisor: Sheldon Landsberger

Lithium ion batteries, due to their relatively high energy density, are now widely used as the power source for portable electronics. Commercial lithium ion cells currently employ layered $LiCoO_2$ as a cathode but only 50 % of its theoretical capacity can be utilized. The factors that cause the limitation are not fully established in the literature. With this perspective, prompt gamma-ray activation analysis (PGAA) has been employed to determine the hydrogen content in various oxide cathodes that have undergone chemical extraction of lithium (delithiation). The PGAA data is complemented by data obtained from atomic absorption spectroscopy (AAS), redox titration, thermogravimetric analysis (TGA), and mass spectroscopy to better understand the capacity limitations and failure mechanisms of lithium ion battery cathodes.

As part of this work, the PGAA facility has been redesigned and reconstructed. The neutron and gamma-ray backgrounds have been reduced by more than an order of

magnitude. Detection limits for elements have also been improved. Special attention was given to the experimental setup including potential sources of error and system calibration for the detection of hydrogen. Spectral interference with hydrogen arising from cobalt was identified and corrected for. Limits of detection as a function of cobalt mass present in a given sample are also discussed.

The data indicates that while delithiated layered $Li_{1-x}CoO_2$, $Li_{1-x}Ni_{1/3}Mn_{1/3}Co_{1/3}O_2$, and $Li_{1-x}Ni_{0.5}Mn_{0.5}O_2$ take significant amounts of hydrogen into the lattice during deep extraction, orthorhombic $Li_{1-x}MnO_2$, spinel $Li_{1-x}Mn_2O_4$, and olivine $Li_{1-x}FePO_4$ do not. Layered $LiCoO_2$, $LiNi_{0.5}Mn_{0.5}O_2$, and $LiNi_{1/3}Mn_{1/3}Co_{1/3}O_2$ have been further analyzed to assess their relative chemical instabilities while undergoing stepped chemical delithiation. Each system takes increasing amounts of protons at lower lithium contents. The differences are attributed to the relative chemical instabilities of the various cathodes that could be related to the position of the transition metal band and the top of the O^{2-}:2p band.

Chemically delithiated layered $Li[Li_{0.17}Mn_{0.33}Co_{0.5-y}Ni_y]O_2$ cathodes have also been characterized. The first charge and discharge capacities decrease with increasing nickel content. The decrease in the capacity with increasing nickel content is due to a decrease in the lithium content present in the transition metal layer and a consequent decrease in the amount of oxygen irreversibly lost during the first charge.

Table of Contents

List of Tables

List of Figures

Chapter 1: Introduction

Energy, now more than ever, has moved to the forefront of scientific interest as practical solutions are being heavily researched to help alleviate and possibly replace the high demands on petroleum products due to increasing population and industrial growth worldwide. In the United States (U.S.), for example, petroleum is the major contributor to energy production but the reserves are limited [1]. As reported in 2003, the U.S. imported 54 % of its petroleum, a value projected to rise to 68 % by 2025, where the primary consumer is the transportation sector as illustrated in Figure 1.1 [2]. Therefore, further development and advancement of hydrogen technologies and electrochemical systems such as lithium ion batteries present a tremendous opportunity for the U.S. to reduce its dependence on imported petroleum. In particular, the advancement and utilization of electric vehicles (EV) or hybrid electric vehicles (HEV) could help alleviate the strain on petroleum products imposed by the transportation sector.

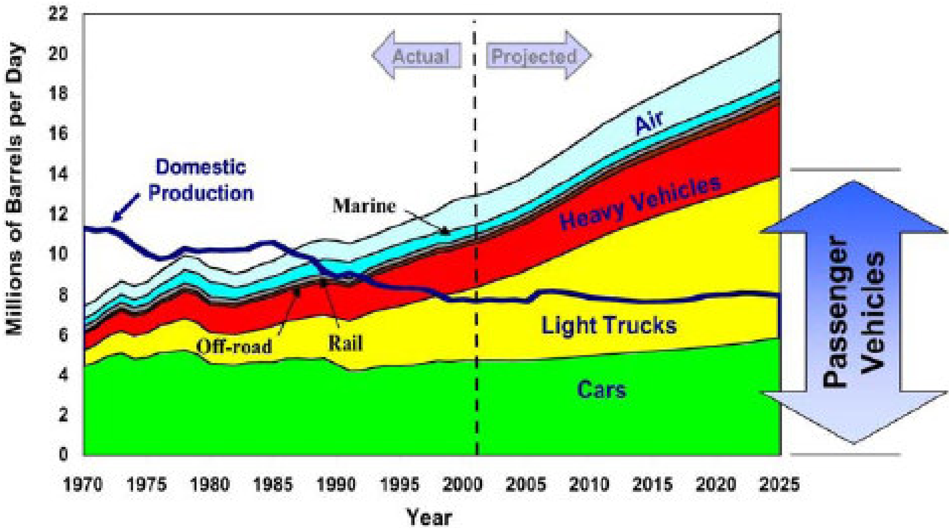

Figure 1.1: U.S. consumption and production of domestic petroleum products [3].

The use of fossil fuel also produces significant amounts of carbon dioxide that negatively impact the environment. In 2004, it was reported that CO_2 produced from energy production was contributing 82 % (weighted by global warming potential) of the greenhouse emissions in the U.S. Increased CO_2 emissions over the last 1,000 years, as illustrated in Figure 1.2, have caused a rise in atmospheric CO_2 levels associated with a rise in global temperature. According to Caldeira *et al.* (2003), in order to stabilize the global mean temperature increase due to CO_2-induced warming at 2 °C, it has been estimated that more than 30 % of the primary power producing energy sources must be noncarbogenic by 2020 [1]. Heavier reliance on electrochemical systems could play a crucial role in helping to reduce CO_2 emission levels.

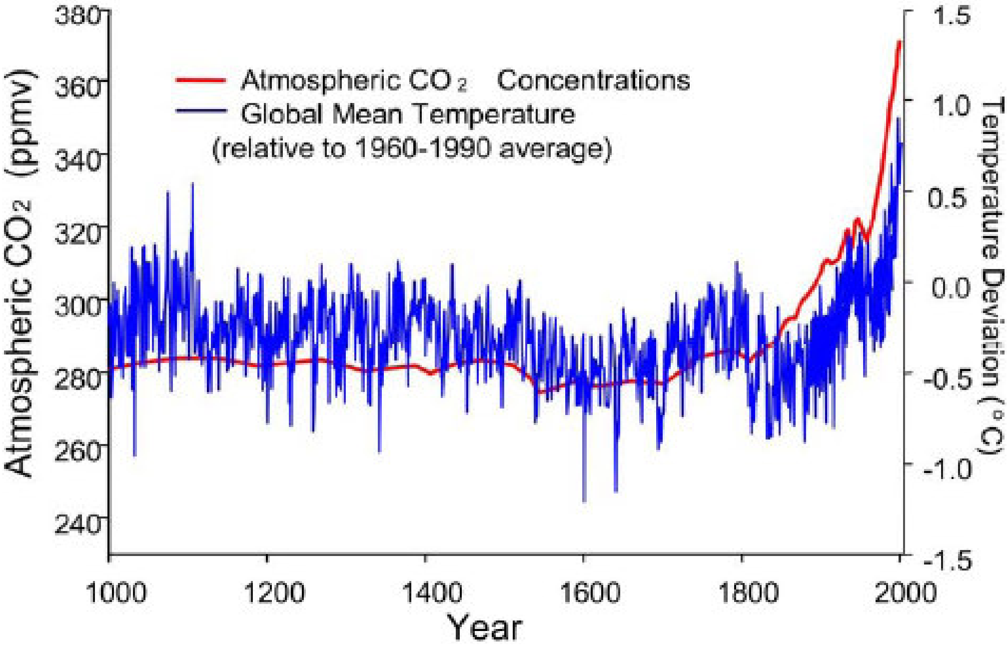

Figure 1.2: Increased CO_2 emissions causing a rise in atmospheric CO_2 associated with a rise in global temperature [1].

Furthermore, with a growing population also comes an increasing need for constant communication and thus a need for more portable, more reliable, more durable, and longer lasting communication devices and other small electronics. An explosion of these small electronic devices over the last couple of decades has been fueled by the tremendous growth of the semiconductor industry. The technological evolution has also caused larger energy demands on the battery systems powering the said devices as they have become increasingly multi-functional and the majority of them are now equipped with full-color screen displays. These advancements have lead to the exploration of high energy density batteries suitable for powering these advanced small electronics for relatively long periods of time. Starting in the early 1990s lithium ion batteries began moving to the forefront of battery technology and accomplishing that goal. Presently, the commercially used lithium ion batteries are still being heavily researched in order to improve upon a number of areas with an emphasis being placed on their practical reversible capacity.

1.1 Lithium Ion Batteries

Sony first introduced the commercial lithium ion battery in the early 1990's and the release was a culmination of three decades worth of research intensely focused on lithium insertion compounds (electrode materials) [4]. Since then, the exponential growth in portable electronic devices such as cellular phones and laptop computers has created an ever-increasing demand for compact, light-weight, rechargeable power sources offering high energy densities. In this regard, lithium ion batteries have become appealing as they provide higher energy density compared to other rechargeable systems such as lead-acid, nickel-cadmium, and nickel-metal hydride batteries as shown in Figure 1.3 [4, 5]. The higher energy density of lithium ion batteries also makes them attractive for EV and HEV applications and they are intensively being pursued at national laboratories, universities, and industry research facilities.

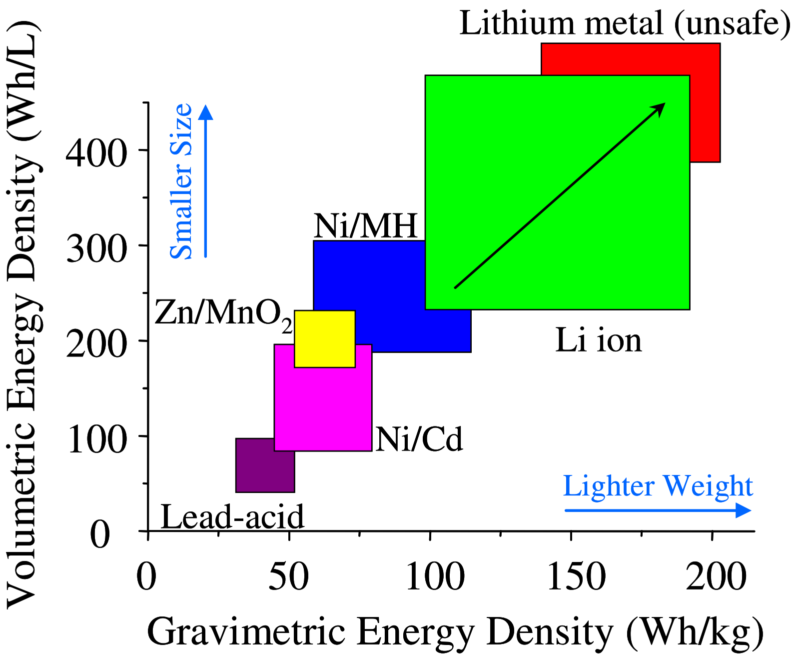

Figure 1.3: Comparison of the energy densities of different battery systems.

A typical lithium ion cell consists of an anode (negative electrode), a cathode (positive electrode), an electrolyte, and an external circuit for electron transfer. Both the anode and cathode are insertion compounds from/into which lithium ions can be reversibly extracted/inserted. While one insertion compound, such as the commercially used layered $LiCoO_2$, serves as the cathode due to its high electrode potential (~ 4 V versus Li), the other insertion compound, such as carbon, serves as the anode due its low electrode potential (< 1 V versus Li). The net cell voltage is given by the difference in the potentials of the two electrodes. The electrolyte solution, usually composed of a lithium salt (*e.g.* $LiPF_6$, $LiClO_4$, $LiBF_4$) in ethylene carbonate (EC) or diethyl carbonate

(DEC), should in theory be a perfect electronic insulator with good ionic conductivity. The electrolyte should also have a large thermodynamic/electrochemical stability window (stable potential domain). Since the electrolyte is a near perfect electronic insulator the electrons coupled to the lithium ions are transferred through the external circuit in the form of electrical energy. During the charge/discharge process, the lithium ions are transferred back and forth between the anode and cathode host sites by way of the electrolyte solution without it being consumed. Reduction occurs in the cathode while oxidation occurs in the anode during battery discharge. In order for the insertion compounds to be either a useful cathode or anode, they must posses a high degree of lithium insertion, high electronic and lithium conductivity, and good reversible insertion/extraction capability with good structural and chemical stability in order to support repeated recharge [4]. Figure 1.4 illustrates the general layout of a lithium ion cell and the charge/discharge process.

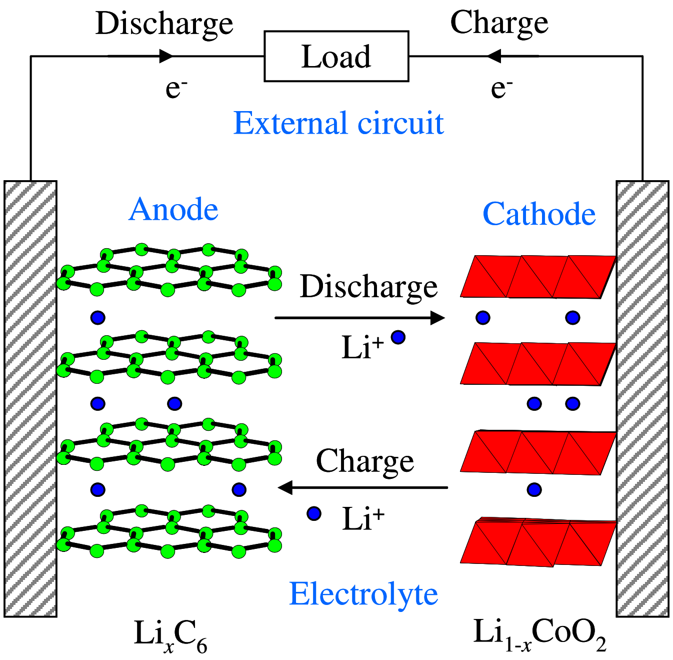

Figure 1.4: General lithium ion cell layout and the charge/discharge process [4].

1.2 Lithium Ion Battery Cathodes

Layered $LiMO_2$ (M = $Ni_{1-y-z}Mn_yCo_z$), spinel $LiMn_2O_4$, and olivine $LiFePO_4$ oxides have become attractive cathodes for lithium ion batteries as they provide good reversible extraction/insertion of lithium and possess relatively good charge/discharge properties [4]. Among them, the layered oxides offer higher capacities (~ 200 mAh g^{-1}) than the spinel or olivine oxides. The $LiMO_2$ layered oxides have an ordered rhombohedral structure in which the Li^+ and M^{3+} ions occupy the alternate (111) planes of the rock salt lattice, as shown in Figure 1.5, which is designated as the O3 structure since the Li^+ ions occupy the octahedral sites with three MO_2 formula units per unit cell [6, 7]. The structure allows for a 2-dimensional diffusion of the Li^+ ions between the edge-shared MO_2 sheets while the $M^{3+/4+}$ redox couples provide good electronic conductivity during the charge/discharge process.

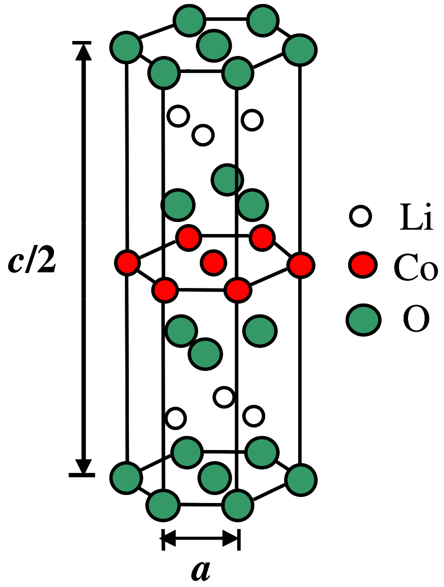

Figure 1.5: O3 crystal structure of layered $LiCoO_2$ [8].

While some systems like $Li_{1-x}Ni_{0.5}Mn_{0.5}O_2$ maintain the initial O3 structure during charging (lithium extraction) for the entire lithium content $0 \leq 1-x \leq 1$, other systems such as $Li_{1-x}CoO_2$ involve the formation of new phases with different structures like P3 or O1. As illustrated in Figure 1.6, the P3 and O1 structures have an oxygen stacking sequence of, respectively, …ABBCCA… and …ABABAB… along the *c* axis and are formed from the initial O3 phase having a sequence of …ABCABC… by a gliding of the CoO_2 sheets [6, 8]. Such a gliding does not require much energy as it does not involve the breaking of any Co-O bonds and so it occurs readily at ambient temperatures. While the O3 and O1 phases have an octahedral geometry for the alkali metal ions with, respectively, three and one MO_2 units per unit cell, the P3 phase has prismatic (trigonal bipyramidal) geometry for the alkali metal ions with three MO_2 units per unit cell [6].

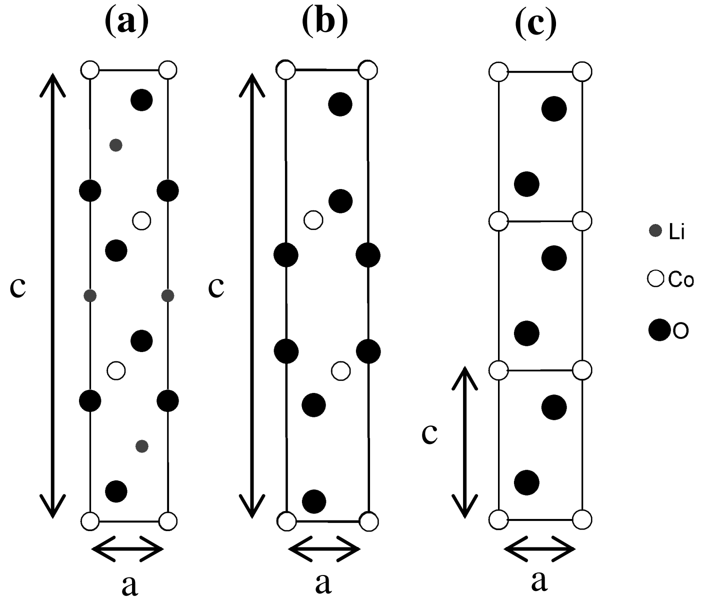

Figure 1.6: Crystal structures of (a) O3-type $LiCoO_2$, (b) P3-type CoO_2, and (c) O1-type CoO_2 viewed along the (100) plane. The oxygen stacking sequences of ABCABC, AABBCC, and ABABAB along the *c* axis, respectively, for the O3, P3, and O1 phases can be readily visualized.

Commercial lithium ion cells currently use the layered $LiCoO_2$ cathodes as it offers a high discharge voltage of around 4 V and exhibits good electrochemical performance (*e.g.* cyclability, rate capability, and high temperature performance). However, only 50 % of the theoretical capacity of $LiCoO_2$ can be utilized in commercial lithium ion cells, which corresponds to a reversible extraction of 0.5 Li per Co ion and a practical capacity of 140 mAh g^{-1} [8]. In contrast, the analogous layered $LiNi_{0.5}Mn_{0.5}O_2$ and $LiNi_{1/3}Mn_{1/3}Co_{1/3}O_2$ cathodes have recently been shown to deliver much higher capacities of close to 200 mAh g^{-1}, which corresponds to around 70 % of the theoretical capacity and a reversible extraction of around 0.7 lithium per transition metal ion [9-16]. More recently, the lithium-rich layered compositions $Li[Ni_xLi_{(1/3-2x/3)}Mn_{(2/3-x/3)}]O_2$ have been found to exhibit even much higher capacities of around 250 mAh g^{-1} (corresponds to a reversible extraction of 0.85 lithium per transition metal ion) with a large plateau at higher voltages in the first charge profile and a huge irreversible capacity loss (> 50 mAh g^{-1}) in the first cycle [17-19]. Despite the same O3 structure (Figure 1.5), the layered oxides differ significantly in their practical capacities and energy densities, and the factors that cause the limitation are not fully established in the literature.

1.3 Chemically Delithiated Cathodes

The lack of a clear understanding of the factors that control the practical capacities of the layered $LiMO_2$ oxide cathodes in lithium ion cells is partly due to the fact that most of the literature investigations have focused invariably on the *in situ* and *ex situ* structural characterization by x-ray diffraction (XRD) of electrochemically charged samples. Based on the structural characterization, the formation of a monoclinic phase at $x = 0.5$ in $Li_{1-x}CoO_2$ due to the ordering of lithium ions has been proposed to be the reason for the limited capacity [20]. However, the analogous $LiNi_{0.5}Mn_{0.5}O_2$,

$LiNi_{1/3}Mn_{1/3}Co_{1/3}O_2$, and $Li[Ni_xLi_{(1/3-2x/3)}Mn_{(2/3-x/3)}]O_2$ cathodes that adopt the same O3-type structure exhibit a higher degree of reversible lithium extraction $0 \leq x \leq 0.85$ (capacities up to 250 mAh g^{-1}) without apparently suffering from the order-disorder transition at $x = 0.5$ [10-19]. More importantly, recent experiments show that the degree of reversible lithium extraction in $Li_{1-x}CoO_2$ can be increased to $0 \leq x \leq 0.7$ (200 mAh g^{-1} capacity) by coating its surface with inert oxides such as Al_2O_3 and ZrO_2 [21-25]. While one group [23] claimed that the improved cyclability is due to the suppression of the monoclinic distortion at $x = 0.5$, another group [24] recently found that the monoclinic distortion is present in the coated samples as well. Thus, it appears that the limitation in the reversible capacity of $Li_{1-x}CoO_2$ cathode may not be due to the monoclinic distortion occurring at $x = 0.5$.

Despite the recognition that the highly oxidized redox couples such as $Co^{3+/4+}$ and $Ni^{3+/4+}$ are characterized by a near-equivalence of the metal:3d and O^{2-}:2p energies particularly in the case of perovskite oxides such as $La_{1-x}Sr_xCoO_3$ and $La_{1-x}Sr_xNiO_3$, little attention has been paid in the literature to the possible oxidation of O^{2-} ions during the charge/discharge process and the consequent chemical instability of the charged $Li_{1-x}MO_2$ lattice. The lack of knowledge on the chemical instability is partly due to the difficulties in chemically characterizing the electrochemically charged layered $Li_{1-x}MO_2$ cathodes as they are contaminated with binder, carbon, and electrolyte used during cathode fabrication and charge/discharge process.

To overcome this difficulty, Dr. Manthiram's group at The University of Texas at Austin (UT), during the past few years, has focused on synthesizing bulk samples of $Li_{1-x}MO_2$ that are free from carbon, binder, and electrolyte by chemically extracting lithium (delithiation) from $LiMO_2$ with an oxidizer in non-aqueous media (acetonitrile) followed by assessing the chemical instability by monitoring the oxidation state of the transition metal ions with the lithium content in $Li_{1-x}MO_2$ through the employment of quantitative wet-chemical analyses (redox titrations) [8, 26-30].

The chemical delithiation was accomplished by stirring the $LiMO_2$ powders with an acetonitrile solution of the powerful oxidizer nitronium tetrafluoroborate (NO_2BF_4) that has an oxidation potential of 5.1 V versus metallic lithium [31] under argon atmosphere using a Schlenk line [8, 26-30]:

$$LiMO_2 + xNO_2BF_4 \rightarrow Li_{1-x}MO_2 + xNO_2 + xLiBF_4 \quad (1.1)$$

The use of an inert atmosphere and non-aqueous medium are strictly essential to prevent the incorporation of water and/or the spontaneous reduction of the highly oxidized $Li_{1-x}MO_2$ samples in contact with the ambient air. After the reaction, the samples were washed with fresh acetonitrile under argon atmosphere to remove $LiBF_4$ and any unreacted NO_2BF_4, dried under vacuum, and stored in an argon-filled glove box before further characterization.

The chemically delithiated $Li_{1-x}MO_2$ samples were then analyzed by a redox iodometric titration to determine the oxidation state of the transition metal ions [32]. The titration involved the dissolution of the sample in a mixture of 10 wt% potassium iodide and 3.5 N hydrochloric acid solution, followed by titrating the liberated iodine with sodium thiosulfate using starch as an indicator. Figure 1.7 compares the variations of the average oxidation state of the transition metal ions thus obtained with the lithium content determined by atomic absorption spectroscopy (AAS) for a few layered oxide systems. While the oxidation state of cobalt in the $Li_{1-x}CoO_2$ system deviates from the theoretically expected value (solid line) and remains constant for $1-x < 0.5$, the average oxidation state of the transition metal ions in the other systems deviates from the theoretical value at a lower lithium content of $1-x < 0.4$. The deviation (lowering) of the oxidation state from the expected value implies a charge imbalance in the system while extracting the positively charged lithium ions and this charge imbalance could be accommodated by either a loss of oxygen from the lattice or an exchange of lithium ions by hydrogen from the reaction medium. While an ion exchange by H^+ may be preferred if enough hydrogen is present, a loss of oxygen from the lattice could occur in the absence of hydrogen as may be the case in the actual lithium ion cells. Either situation (ion exchange by hydrogen or oxygen loss) may reflect the onset of chemical instability in the system. Thus the chemical delithiation experiments may serve as a tool to assess the relative chemical stability of the layered $LiMO_2$ cathodes with various transition metal ions. The deviation of the oxidation state from the theoretical value at a higher lithium content $1-x < 0.5$ in $LiCoO_2$ compared to that in the Ni- and Mn-rich systems ($1-x < 0.4$) in Figure 1.7 suggests a greater chemical instability for the $LiCoO_2$ system compared to the Ni- and Mn-rich systems. Thus the lower reversible capacity of $LiCoO_2$ (140 mAh g^{-1}) as compared to that found with some of the Ni- and Mn-rich systems (180 – 250 mAh g^{-1}) could be related to the onset of chemical instability at a higher lithium content in the $LiCoO_2$ system [33].

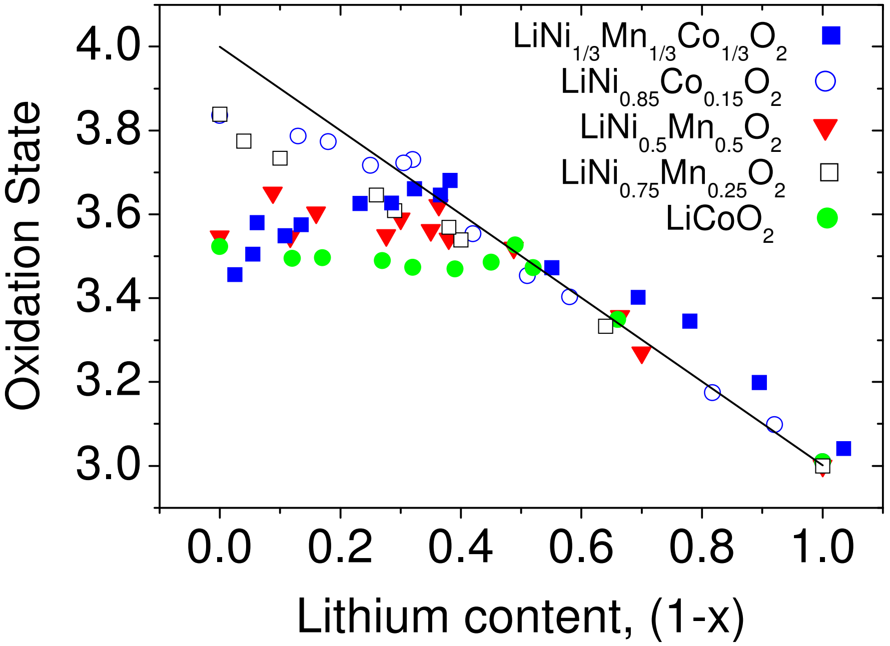

Figure 1.7: Comparison of the variations of the average oxidation state of the transition metal ions with lithium content (1-x) in $Li_{1-x}Ni_{1-y-z}Mn_yCo_zO_2$. The solid line refers to the theoretically expected oxidation state value assuming the oxygen content remains as 2.0 and no ion exchange of Li^+ by H^+ occurs during lithium extraction [8, 28, 30, 33].

Although the chemical characterization data presented above provides new insight into the factors that limit the practical capacities and energy densities of the lithium ion battery cathodes, the exact charge compensation mechanism (oxygen loss from the lattice versus an exchange of lithium by hydrogen) that occurs, while the oxidation state value deviates from the theoretical value, is yet to be resolved. Additionally, whether such a deviation of the oxidation state in fact occurs during the over-charging (deep lithium extraction) of actual lithium ion cells is not known. It is possible that protons generated in the acetonitrile medium in the presence of the powerful oxidizer NO_2BF_4 may lead to a deviation of the oxidation state of the transition metal ions at deep lithium extraction in the chemically delithiated samples due to an ion exchange of Li^+ by H^+ and such a deviation may not occur in electrochemically charged samples. However, recent reports indicate that an ion exchange of Li^+ by H^+ ions occurs on charging beyond Mn^{4+} in electrochemical cells fabricated with the layered Li_2MnO_3 or $Li_x[Mn_{1-y}Li_y]O_2$ ($0 \leq y \leq 0.33$) and $LiPF_6$ in ethylene carbonate/dimethyl carbonate electrolyte at 55 °C [34-36]. The report was based on a mass spectroscopic analysis of the charged cathodes, and the protons in this case were perceived by the authors to be electrochemically generated from the electrolyte solvent at higher potentials of around 4.5 V [34-36]. The authors reported that both an ion exchange of Li^+ by H^+ as well as a loss of oxygen from the lattice takes place on deep charging of Li_2MnO_3 or $Li_x[Mn_{1-y}Li_y]O_2$ beyond Mn^{4+} [34-36]. However, the exchange of Li^+ by H^+ in the case of Li_2MnO_3 and $Li_x[Mn_{1-y}Li_y]O_2$ could be due to the forced oxidation beyond Mn^{4+} since it is generally hard to obtain oxidation states greater than Mn^{4+} in oxides. In contrast, oxidation states such as Co^{4+} and Ni^{4+} are known to occur in oxides, and therefore, the situation with $Li_{1-x}CoO_2$ could be different from that of Li_2MnO_3.

With the present state of the knowledge in the literature, four possibilities exist for the electrochemical redox process occurring at deep charging of the layered $Li_{1-x}MO_2$ cathodes: (i) oxidation of M^{3+} to M^{4+} as one would normally anticipate, (ii) oxidation of O^{2-} ions leading to a loss of oxygen from the lattice, (iii) ion-exchange of Li^+ by H^+ that was generated by an electrochemical oxidation of the electrolyte solvent, or (iv) the combination of two or all the three of the above processes. The only way this can be resolved is by a careful and quantitative analysis of the proton content in electrochemically charged and chemically delithiated samples and coupling the hydrogen content data with the oxidation state data obtained from the redox titration. However, quantitative analysis of the hydrogen content is not a trivial task. Being a light element, the available techniques to precisely determine hydrogen content are limited. Generally, the hydrogen content may be determined by heating the samples and monitoring the weight loss as H_2O by way of thermogravimetric analysis (TGA) and/or detecting hydrogen by mass spectroscopic analysis of the evolved gas. These types of procedures involving heating could potentially lead to erroneous results because of the organic binders and carbon black used in fabricating the cathode and organic solvents used in the electrolytes and a misconception of the operating mechanisms at deep charge. Therefore, a more careful and diligent analysis of the hydrogen content in the charged $Li_{1-x}MO_2$ cathodes is essential to clearly establish the operating mechanism without any ambiguity. An identification of the actual reaction mechanism among the various four possibilities suggested above can help to: (i) establish a firm basic scientific understanding of the failure mechanisms of the lithium ion battery cathodes and (ii) design and develop high performance cathodes for future generation powers sources for consumer, military, and space applications.

Thus, use of an analysis technique to precisely determine the hydrogen content in various oxide cathode samples obtained by chemical lithium extraction and complemented by AAS, wet-chemical redox titration studies, and analysis of the evolved gas on heating (*i.e.* TGA and/or mass spectrometry) would be of great benefit. A comparison of the hydrogen data with the data obtained from other techniques would clearly establish the issue of proton insertion at deep charge in lithium ion battery cathodes.

1.4 Objectives

With this in mind, the aim of this work was to quantitatively determine the hydrogen content in various lithium ion battery cathodes by way of prompt gamma activation analysis (PGAA) in order to assess their relative chemical stability while undergoing chemical extraction of lithium and thus provide insight into the factors that limit the reversible capacity of lithium ion batteries. PGAA of lithium ion battery cathodes is a novel study that to date has only been undertaken and accomplished at UT. Such a study will help to: (i) broaden the understanding of the structure-property-performance of lithium ion battery cathodes and (ii) design and develop newer, better performing lithium ion batteries that will have a significant impact in the area of power sources for both portable electronic devices and EV or HEV.

During the course of this study, a number of lithium ion battery cathode materials were characterized using PGAA. The PGAA data was complemented by other, more traditional, analytical, chemical, and structural characterization techniques such as XRD, AAS, wet chemical redox titration, TGA, and mass spectrometry, respectively, all of which are available at UT. As mentioned, the utilization of PGAA for the analysis of lithium ion battery cathodes had never been undertaken before this study was conducted. It has proven to be a novel approach for the purposes of developing a better understanding of the behavior of lithium ion battery cathodes.

This project is a multidisciplinary investigation involving aspects of materials science and nuclear engineering. The facilities available at both the Nuclear Engineering Teaching Laboratory (NETL) and the Texas Materials Institute (TMI) located at UT were instrumental in carrying out this investigation. This research has helped to identify the type of mechanism(s) (*i.e.* proton insertion, oxygen loss, and/or complete transition metal ion oxidation) occurring during chemical delithiation of various oxide cathodes, where chemical delithiation is a process that simulates the electrochemical charging of lithium ion batteries.

This study was divided into four major objectives: (i) PGAA facility improvement for hydrogen analysis, (ii) PGAA facility characterization for hydrogen analysis, (iii) synthesis of lithium ion battery cathodes, and (iv) analysis of lithium ion battery cathodes. Furthermore, the investigation was divided into two phases. Phase I included PGAA facility improvements to the system detection limits, suppression of background noise, and preliminary experiments using samples with known hydrogen concentrations for the purposes of system calibration. Phase II involved the synthesis of samples, collection of data, and interpretation of results. Initially, at least 20 different oxide cathode compositions, predominately layered, before and after lithium extraction were expected to be tested. In the end, more than 200 oxide compositions were prepared (some were provided to the author by others in Dr. Manthiram's group) by chemical delithiation and analyzed by PGAA but not all of them produced reasonable results either due to incomplete reactions or structural breakdown during the delithiation process.

It should be noted that while all of the data presented in this dissertation is only relevant for chemically delithiated lithium ion cathodes, it is a fundamental study that provides valuable information towards the failure mechanisms that may be occurring in practical lithium ion cells. Nevertheless, a complete analysis and characterization of actual electrochemical lithium ion cathodes would be of great interest to the battery community as it would help to better understand some of the issues in the lithium ion battery area. In this regard, an attempt was made during this investigation to analyze a few electrochemically charged cathodes. However, due to a combination of the hydrogen detection limitations of the PGAA facility and the relatively small amount of active material present in the electrochemically charged cathodes, the determination of hydrogen with practical lithium ion cathodes was not feasible. Nonetheless, in short, all the major objectives were accomplished in a reasonable and timely fashion and the accompanying results are presented as detailed below.

Chapter 2 of this dissertation presents a comprehensive look at the theory and fundamentals of PGAA. Some of the more prominent facilities dedicated to PGAA will also be presented and described. Applications of PGAA and the theory behind the detection of hydrogen are also divulged. Prominent PGAA sources of error and how to best suppress them is also discussed.

Chapter 3 provides a description of the NETL and its experimental facilities. In particular, the PGAA system in association with the Texas Cold Neutron Source (TCNS) facility is described in great depth.

Chapter 4 reveals the experimental methods utilized throughout this investigation. The general lithium ion oxide cathode sample synthesis techniques are described along with the PGAA relative standardization method used for the direct determination of hydrogen content in the oxide samples. Spectral interference with hydrogen arising from cobalt is discussed. Attention is given to the experimental setup including the precautions taken during sample preparation and analysis to suppress PGAA sources of error encountered during this study. Brief descriptions of the other materials characterization techniques used during this study are also provided.

Chapter 5 focuses on the upgrades and subsequent calibration and characterization recently performed on the PGAA facility as part of this work. Special attention is paid to the types of shielding materials chosen, why they were chosen, and where they were placed throughout the PGAA facility. The measured thermal equivalent flux, fluence variation at the PGAA sample position, effective beam temperature, and identified background elements are given. System calibration for the detection of hydrogen and limits of detection as a function of cobalt mass present in a given sample are also discussed.

Chapter 6 details the results obtained from the characterization experiments performed on the lithium ion battery cathode materials of interest. A discussion on the significance of the obtained data as well as any direct correlations between these findings and cathode performance is revealed.

Chapter 7 provides the conclusions taken from this investigation and recommendations for future work concerned with these types of studies.

Chapter 2: Prompt Gamma Activation Analysis

2.1 Theory

PGAA is a nuclear, nondestructive technique typically used to measure elemental concentrations of elements such as H, B, S, Cl, Si, Al, N, and C that de-excite with an appropriate gamma-ray immediately following neutron capture [37-41]. In general, PGAA investigations can be performed in a straightforward manner as one only needs a source of neutrons, a sample of interest, neutron and gamma-ray shielding to suppress background noise, a gamma-ray detector, and electronics to properly analyze the signals generated by the detector. PGAA utilizes a gamma-ray detector usually composed of high purity germanium (HPGe) for acquiring a spectrum of prompt gamma-rays released immediately after neutron capture reactions with isotopic constituents present in the sample being irradiated. The compound nuclei that are formed de-excite via emission of these prompt gamma-rays in less than a nanosecond [37-41]. The energy associated with the individual prompt gamma rays being emitted is characteristic of the interacting isotope. Often times, PGAA contains hundreds of gamma-ray peaks and thus produces complicated spectra. Figure 2.1 illustrates a typical PGAA experimental setup and the following presents the nuclear reaction used by PGAA:

$$
{}_{Z}^{A}X + {}_{0}^{1}n \rightarrow {}_{Z}^{A+1}X^{*} \rightarrow {}_{Z}^{A+1}X + {}_{0}^{0}\gamma(E_{\gamma}) \tag{2.1}
$$

where X is the element of interest, A is the mass number, Z is the atomic number, n represents the impinging neutron, X^{*} is the compound nucleus, $\gamma(E_{\gamma})$ represents the emitted gamma-ray that has a characteristic energy E_{γ}.

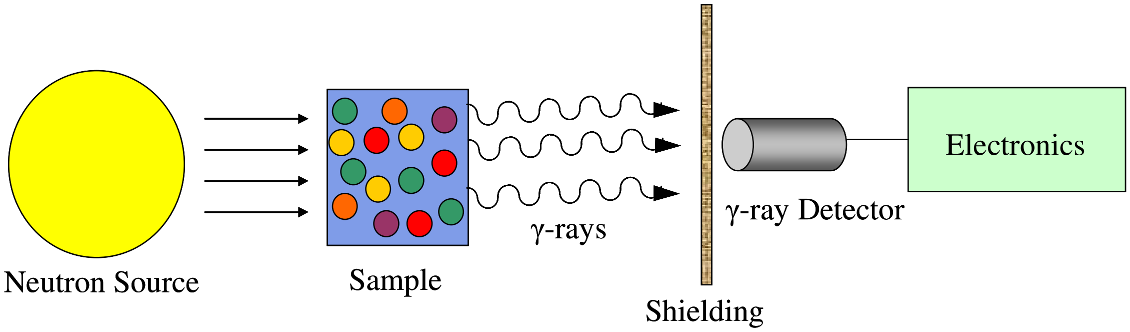

Figure 2.1: Typical PGAA experimental setup.

PGAA is complementary to conventional instrumental delayed neutron activation analysis (INAA). The characteristics shared by the analytical techniques are: independence of matrix and chemical state, good sensitivity for many elements, and highly penetrating probe and response radiations [38]. PGAA is used to complement INAA in situations where the formed radioactive capture products are stable, very short-lived, or don't decay with an appropriate gamma-ray. Through the combined use of PGAA and INAA all major and minor elements may be determined. The main difference between PGAA and INAA is that while PGAA acquires data related to the prompt release of gamma-ray radiation, INAA acquires data related to the delayed release of gamma-ray radiation. Typically, the samples are exposed to lower neutron fluxes compared to INAA and so the activation of the sample is lower, which permits immediate use of the same sample for other experiments.

Challenges involved with PGAA include the shielding of neutrons, reduction of background, scattering of neutrons, and detector calibration [37-39]. The HPGe detector must be shielded from stray neutrons and gamma-rays in order to effectively reduce background noise. The shielding that directly surrounds the HPGe is generally composed of lead covered by efficient neutron absorbers. By arranging the detector shielding in this manner incoming neutrons are captured by the absorbing material and the lead acts to eliminate the secondary radiation that is subsequently produced. Boron, cadmium, and lithium containing materials seem to be good choices for neutron absorbers because they are economical and posses relatively large capture cross-sections [37, 38].

The efficiency of PGAA relies on the strength of the prompt gamma-ray peak. Any steps that can increase the prompt gamma-ray emission rate will increase the system sensitivity. Therefore, since neutron absorption cross-sections are typically proportional to the inverse of neutron velocity at low energies:

$$\sigma(v) = \sigma_0 \frac{v_0}{v} \tag{2.2}$$

where $\sigma(v)$ is the neutron absorption cross-section (cm^2) corresponding to an arbitrary neutron velocity v ($m\ s^{-1}$), σ_0 is the neutron absorption cross-section (cm^2) that corresponds to a neutron velocity v_0 ($m\ s^{-1}$) with a typical value of 2,200 $m\ s^{-1}$ that is representative of the thermal neutron energy $E_0 = 0.0253$ eV. A source of cold neutrons can be used to enhance the prompt gamma-ray signal for light nuclides. When traveling at sub-thermal velocities ($< 1400\ m\ s^{-1}$), neutrons exhibit wave characteristics and can be transported using guide beams [37, 42-44]. This results in minimal loss of neutron beam intensity, which is common in conventional beams due to $1/r^2$ loss. Neutron beams can also be preferentially bent away from the beam centerline to reduce the background gamma-ray noise produced in the reactor. If the incoming neutron beam is not filtered, then the shielding adjacent to the reactor beam port should serve to moderate the epithermal neutrons emerging from the reactor core [37, 38]. This directly leads to background reduction, increased gamma-ray emission by the irradiated sample, and greater overall system detection limits.

PGAA can be performed on samples of any form: solid, liquid, or gas. Sample size and shape can, theoretically, be completely arbitrary. The only limitations on sample geometry depend on the specific PGAA facility being used for experimental purposes. Preparation of samples is also fairly straightforward and uncomplicated [37-41].

2.2 Facilities and Applications

PGAA has been used for the purposes of analysis in a large number of scientific and technology related fields where some examples are: analysis of standard reference materials (SRM), isotopic and chemical composition research, chemical matrix studies, analysis of ores, metal alloys and construction materials, glass and semiconductor studies, nuclear technology applications, analysis of fossil fuels, geology, geochemistry and cosmochemistry studies, investigation of art and archeology, analysis of food, human and animal studies, examination of atmospheric gases and particles, water and sediment pollution investigation, and medical studies [37].

There are a number of PGAA facilities in operation throughout the world. Some of the better known reactor based PGAA facilities are located at: the National Institute of Standards and Technology Center for Neutron Research (NCNR), the Institute of Isotope and Surface Chemistry Budapest Research Reactor (BRR), the Seoul National University-Korea Atomic Energy Research Institute (SNU-KAERI) High-flux Advanced Neutron Application Reactor (HANARO), the Vietnam Atomic Energy Commission Dalat Nuclear Research Reactor (DNRR), the Japan Atomic Energy Research Institute (JAERI) Research Reactor (JRR-3M), and the Paul Scherrer Institute (PSI). Non-reactor based neutron sources have also been used to perform PGAA experiments and their application is primarily focused on developing portable detector capability for specific applications. The neutron flux at such facilities is lower and hence their application to materials research is limited. For the purposes of this report, the above mentioned PGAA facilities will be discussed in limited description.

The NCNR, located in Gaithersburg, Maryland, utilizes both thermal and cold neutron PGAA facilities, each of which uses a 20 MW research reactor as its neutron source [45]. The PGAA facilities at the NCNR have been used for many applications including improving the PGAA techniques themselves [46-48]. The NCNR thermal PGAA facility has been in operation since 1979 and has recently undergone several modifications that have greatly reduced the limits of detection compared with those of the original instrument due to reduced Compton and scattered gamma-ray backgrounds, increased sensitivities, and reduction of background gamma-ray photopeak intensities. The thermal PGAA facility has predominately been used for determination of elements contained within biological, environmental, and industrial materials. The thermal facility has recently been used to determine concentrations of elements such as B, Ca, Cl, Cd, H, K, N, Na, P, S, and Zn in food-related matrices as well as in several SRM and botanical samples [49].

A new NCNR cold PGAA facility is in the process of being designed and built as part of plans to modify the cold neutron guide (NG7) on which the cold PGAA instrument has been operating since 1991 [50]. The incoming neutrons, after being moderated by liquid hydrogen at 20 K, pass through a ^{58}Ni coated guide to the PGAA sample position. The current cold PGAA facility has a thermal equivalent neutron flux of 9×10^{8} cm^{-2} s^{-1}. A 35 % efficient, relative to sodium-iodide, HPGe detector with a 1.7 keV resolution at 1333 keV is used for counting gamma-rays emitted from irradiated samples. The detector has lead shielding surrounding it in all directions with cadmium covering the front face and is positioned vertically inside a horizontal bismuth germanate

(BGO) Compton-suppression detector with its axis perpendicular to the neutron beam [51].

Another leading PGAA facility is at the Institute of Isotope and Surface Chemistry in Budapest, Hungary [52, 53]. From 1996 to 2000, the 10 MW BRR was equipped with a thermal neutron PGAA facility capable of producing a thermal equivalent flux of 2×10^6 cm^{-2} s^{-1} at the sample position [54]. In 2001, a reconstructed neutron wave guide and a 20 K liquid hydrogen moderator were installed, effectively transforming the thermal neutron facility into a cold neutron facility. The modifications have proved useful as the average thermal equivalent flux at the PGAA sample position has increased by an order of magnitude to 5×10^7 cm^{-2} s^{-1}. The reconstructed guide is equipped with a beam chopper as well as a split beam at the end of the guide in order to serve both the cold PGAA facility and a neutron induced prompt gamma-ray spectroscopy (NIPS) facility. Chemical analysis is the PGAA facility's primary application while NIPS is dedicated to all other nuclear spectroscopic measurements involving the detection of prompt gamma-ray radiation from materials activated in the neutron beam [54]. The PGAA facility at the BRR is also used for analysis related to archeology, material testing, geology, chemistry, industrial applications, and the investigation of nuclear materials [54]. In collaboration with Lawrence Berkeley National Laboratory, the BRR has been in the process of developing a comprehensive prompt gamma-ray library [55-58]. The Budapest facility has also demonstrated the use of PGAA to analyze hydrogen and other metals [59-61].

The 30 MW HANARO located in Daejeon, South Korea is home to the thermal PGAA facility that was jointly developed by SNU and the KAERI in 2001 [62]. The SNU-KAERI PGAA facility became operational as the result of an effort to characterize ^{10}B in order to develop boron neutron capture therapy capabilities at HANARO [63]. A nearly pure thermal neutron beam is present at the PGAA sample position with a flux of 7.9×10^{7} cm^{-2} s^{-1} through the use of a polychromatic beam that is extracted by the diffraction technique and directed by pyrolytic graphite crystals [62, 64]. Gamma-rays are detected by a 43 % efficient n-type HPGe detector that is extensively surrounded by ^{6}LiF in order to minimize background neutron radiation [65]. This PGAA facility has been used for the determination of boron concentration in several SRMs [62].

The DNRR, made operational in 1984, is maintained by the Vietnam Atomic Energy Commission. The DNRR is a pool type TRIGA Mark II research reactor that was initially installed in 1963 to operate at a power level of 250 kW. The reactor was reconstructed in 1982 and upgraded to operate at a power of 500 kW. A maximum thermal flux of 2.1×10^{13} cm^{-2} s^{-1} is produced by the reactor that is used for research, isotope production, neutron activation analysis, and training. A PGAA experimental area was brought online in 1989. It utilizes a filtered thermal beam that is capable of producing a flux of 2.1×10^{7} cm^{-2} s^{-1} [66]. The DNRR facility has recently been used to develop k_0 factors for several elements in partnership with other facilities [55]. The PGAA at the DNRR has also recently been configured for in-vivo determination of various toxic elements in organs such as kidney and liver [66].

The PGAA instrument at the JRR-3M 20 MW reactor is designed in such a manner that it can be moved and repositioned at the end of either a cold or thermal neutron guide. The cold guide delivers a flux of 1.1×10^{8} cm^{-2} s^{-1} while the thermal guide provides a flux of 2.4×10^{7} cm^{-2} s^{-1}, respectively [67]. The heart of the PGAA system is a BGO Compton suppressed HPGe detector shielded with LiF tiles. The PGAA sample position is located in a Teflon® sample chamber that can be purged with helium [68]. PGAA at JRR-3M has been used to analyze marine oil, sediment, and bivalve samples [69]. Agricultural samples have been studied using PGAA for purposes of analyzing contaminants present in them [70]. The PGAA facility has also been used for boron determination in marine samples [71] and heavy metal uptake in rats [72].

The PSI in Villigen, Switzerland is home to the 10^{14} cm^{-2} s^{-1} continuous spallation neutron source (SINQ). As the name suggests, neutrons are produced through spallation caused by protons accelerated through a 590 MeV accelerator into a deuterium cooled array of zircaloy rods positioned in an aluminum container. The PSI also houses a 25 K deuterium moderated cold neutron PGAA facility with an available flux of 6.9×10^{7} cm^{-2} s^{-1}. The detection system includes a Compton-suppression spectrometer and a pair spectrometer. An interesting feature of this PGAA facility is the capillary-based neutron focusing optics that permits scanning of samples and nuclear spectroscopy of isotopes having small capture cross-sections [73]. The PGAA facility has been useful for materials research, investigation of biological substances, and the elemental analysis of standards [74, 75].

2.3 Hydrogen Detection

PGAA relies on measurement of the nearly instantaneous de-excitation excess energy, through the emissions of one or more gamma rays, present in a nuclide formed by neutron capture. These gamma ray(s) are emitted even if the daughter nuclide is stable. Natural hydrogen is composed of ^{1}H (99.985 %) and ^{2}H (0.015 %). Hydrogen analysis using INAA is not possible as the principal activation product, ^{2}H, is stable. A small amount of ^{3}H, is produced in minute quantities, however, it does not decay by delayed gamma-ray emission, an essential characteristic for INAA [39]. Although ^{2}H is stable, when ^{1}H absorbs a neutron, the resulting ^{2}H nucleus contains excess energy compared to its ground state and so immediately de-excites via a single, 100 % yield, prompt gamma-ray. This gamma ray can be used for PGAA measurement of H.

Prompt gamma-ray spectra generally cover a wide range of energies and individual gamma rays are well separated even for spectra with many prompt gamma-ray energies. Qualitative analysis of samples for hydrogen content is quite simple in most cases (complications with ^{59}Co are discussed in Section 2.4.2) although quantitative analysis can be complex. The reaction shown below illustrates the neutron capture by ^{1}H:

$$ {}_{1}^{1}H + {}_{0}^{1}n \rightarrow {}_{1}^{2}H^{*} \rightarrow {}_{1}^{2}H + {}_{0}^{0}\gamma(2223.25 \text{ keV}) \tag{2.3} $$

The above reaction may also be represented as such: ${}_{1}^{1}H(n,\gamma){}_{1}^{2}H$. In this case, the nucleus decays by releasing only one characteristic 2223.25 keV gamma-ray [37].

PGAA has been used at a number of leading research facilities to determine hydrogen and other low atomic number materials nondestructively. For example, the cold neutron PGAA facility at the NCNR has been used to determine hydrogen content in niobium [41], doped $SrCeO_3$ [76], titanium [77], and H-ZSM-5 zeolites [78]. The NCNR has also applied PGAA to certify many light elements including hydrogen and boron concentrations in SRMs [78] and has also been used to measure boron content in various mineral separates such as sillimanites (Al_2O_3-SiO_2), muscovites (K_2O-$3Al_2O_3$-SiO_2-$2H_2O$), and biotites $K_2(Mg,Fe)3AlSi_3O_{10}(OH,O,F_2)_2$ [51].

2.4 Sources of Error

2.4.1 Gamma-Ray Background

Gamma-ray background should be kept as low as possible in order to reduce interferences. Background gamma rays originate from a number of sources: detector and facility shielding materials, sample environment, reactor produced decay products, naturally occurring radionuclides found in surrounding materials, and cosmic radiation. The direct gamma-ray background is enhanced when targets with a large neutron scattering power are irradiated. The scattered neutrons will interact with the sample chamber and other surrounding materials often including the detector, and enhance the count rates for some of the elements in the background spectrum. This effect can be quantified for most elements except hydrogen by irradiating a sample with a scattering power equal to that of the sample to be measured, and then determining the background.

Unwanted gamma-ray signals can also originate from within the sample of interest and one of the drawbacks associated with PGAA is the inability to determine the origin of specific elemental gamma-ray signals unless proper experimental techniques are put into place. An example of this is the inability to distinguish between hydrogen embedded in the sample matrix and hydrogen that could be adsorbed in the form of water on the surface of the sample.

Modifying the sample's environment during irradiation can help alleviate some of the gamma-ray noise originating in its vicinity. Some of the more typical techniques for suppressing background gamma-ray noise include the use of a purge or evacuation chamber in order to displace the air immediately surrounding the sample of interest. Also, the use of low gamma-ray emitting materials as sample holders and supports such as aluminum and Teflon® can be selected to further reduce background.

2.4.2 Spectral Interference

Due to the complex nature of PGAA spectra, spectral interferences often contribute to analytical error [37]. As presented in Table 2.1, there are several gamma lines that could potentially overlap with the hydrogen signal. However, taking into account the partial gamma-ray production cross-section ($\sigma_{\gamma}^{Z}(E_{\gamma})$) of other isotopes in the target and the types of structural materials directly surrounding the PGAA experimental station, only ^{59}Co presents any significant interference issues given the HPGe detector's energy resolution for the samples analyzed in this study.

Table 2.1: Gamma-ray lines near 2223.25 keV [79].

E_{γ}(keV)	Isotope	$\sigma_{\gamma}^{Z}(E_{\gamma})$	Decay type	Half-life
2220.00(23)	^{115}Sn	0.0019(5)	prompt	s
2220.05(4)	^{23}Na	0.00093(10)	prompt	s
2220.47(6)	^{167}Er	0.13(6)	prompt	s
2220.49(3)	^{41}K	0.00054(10)	prompt	s
2220.88(3)	^{39}K	0.0038(5)	prompt	s
2221.61(4)	^{59}Co	0.261(8)	prompt	s
2221.80(9)	^{73}Ge	0.0013(8)	prompt	s
2222.1(7)	^{179}Hf	0.0035(7)	prompt	s
2222.5(4)	^{94}Mo	0.0050(11)	prompt	s
2223.25	^{1}H	0.3326(7)	prompt	s
2223.5(3)	^{102}Ru	0.009(15)	prompt	s
2224.49(9)	^{70}Ge	0.0034(11)	prompt	s
2224.65(10)	^{35}Cl	0.050(17)	prompt	s
2225.40(3)	^{115}Sn	0.0082(5)	prompt	s
2225.5(8)	^{115}In	0.080(13)	delayed	54.41 m
2225.5	^{115}In	0.002000(4)	delayed	14.10 s

As alluded to previously, commercial lithium ion batteries currently use the $LiCoO_2$ cathode and a quantitative assessment of whether or not an ion exchange of lithium by hydrogen occurs at deep lithium extraction will be valuable. However, the determination of hydrogen concentration in $Li_{1-x}CoO_2$, or any other cobalt-containing compound for that matter, poses an additional challenge in the form of peak interference from a ^{59}Co prompt gamma-ray line.

^{59}Co has a prompt gamma-ray signal at 2221.61 keV, which is very close in proximity to the hydrogen signal at 2223.25 keV. The HPGe is unable to distinguish between the two signals and sums both into one peak, making it difficult to directly resolve the area associated with the hydrogen peak (Figure 2.2) and complicated to quantify the amount of hydrogen present in the sample matrix. If uncorrected, this interference would be the biggest source of error in regards to the analysis of lithium ion battery cathodes using PGAA at UT. As discussed later, this interference can be identified, quantified and subtracted through a ratio technique with another ^{59}Co gamma-ray.

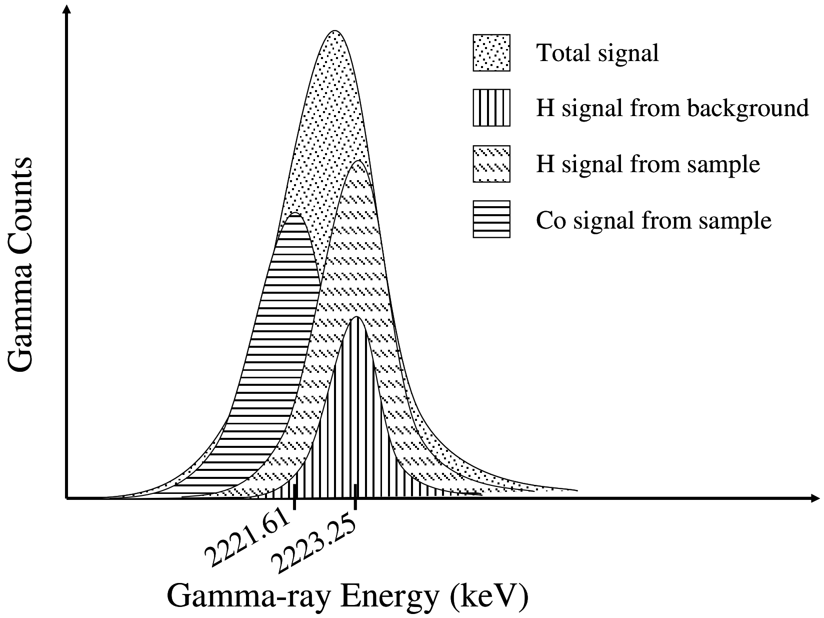

Figure 2.2: Illustration of ^{59}Co-2221.61 keV peak interference with ^{1}H-2223.25 keV peak.

2.4.3 Sample Self-Absorption

Neutron and gamma-ray self-absorption (self-shielding) are problems that can arise depending on the matrix composition of the sample of interest. When considering this study, lithium, cobalt, and boron arising from the use of NO_2BF_4 are some of the more problematic elements in regards to their relatively large absorption cross-sections. In particular, because of boron's large absorption cross-section, even trace amounts of this element present in a given sample could adversely affect data obtained from PGAA measurements. In an effort to reduce the possibility of these errors occurring during this study special attention was paid to the experimental setup and sample preparation for PGAA. Errors due to self-absorption can be remedied by closely matching the geometries and elemental composition of the samples and standards when using the relative standardization method (discussed in Section 4.2) [37]. Precautions maintained during this study are divulged in Section 4.4.

2.4.4 Neutron Scattering

Neutrons scattering within the sample of interest and neutrons scattered out of the sample into materials that are present in the sample environment influence elemental sensitivities and cause an increase in gamma-ray background. Thus, samples that contain elements with large scatter cross-sections can be difficult to analyze. Hydrogenous samples are the most likely to be effected by neutron scattering due to its large incoherent scattering cross-section. The effect of scattering on the analytical sensitivity depends on the characteristics of the neutron beam (*e.g.* effective beam temperature) [37].

Using the thermal beam at NIST, it was shown that analytical sensitivities of H obtained using 1.27 cm disk-shaped tri-hydroxymethyl-aminomethane (THAM) samples set at an angle of 45° increased with increasing disk thickness from 0 to 3 mm but decreased beyond 3 mm. However, sphere-shaped THAM samples of varying size showed constant hydrogen sensitivities. Similar studies measuring the effects of neutron scattering on elements other than H demonstrated that identical changes in sensitivity were obtained for all 1/*v* elements present in the samples as the hydrogen concentration was varied. From these investigations, it was concluded that elastic scattering changes the mean free path length of the neutrons traveling through the target and therefore changes the probability of neutron absorption [37].

Neutron scattering studies were also performed with the cold neutron beam at NIST. It was shown that, when irradiating room-temperature (300 K) THAM targets with a cold neutron beam, H analytical sensitivities decreased with increasing sample size for both disks and spheres. However, when the same samples were cooled to 77 K and then irradiated with the cold beam, the effects of neutron scattering on the H sensitivities were similar to that of room-temperature samples irradiated in a thermal neutron beam. In addition, when irradiating room-temperature samples with a cold neutron beam, the thermalizing effect of neutron scattering increases the average neutron temperature and thus decreases the capture cross-section according to the 1/*v* law [37].

The effects of neutron scattering can be offset by maintaining a spherical sample geometry or similar to that of a sphere and keeping constant geometries between samples and standards [37]. Ideal sample sizes for the purposes of PGAA have been reported to be less than 10-mm thick with a mass of 0.1 to 1.0 g [39].

Chapter 3: Experimental Facility

3.1 Nuclear Engineering Teaching Laboratory

The NETL, located on the J.J. Pickle Research Campus, is designed with two main experimental areas; the first area is a 335 m^2 bay that houses a TRIGA Mark II research reactor and the second area is an 84 m^2 bay for external core radiation experiments and facilities [80]. The UT-TRIGA is a General Atomic designed water-cooled pool type 1.1 MW reactor with 19.7 % enriched uranium-zirconium hydride fuel for producing neutrons via fission. When the reactor is initially off, the chain reaction is initiated with the help of a 2 Ci AmBe source that produces approximately 10^6 neutrons/second. The UT-TRIGA is equipped with a rotary specimen rack, a pneumatic transfer system, an in-core central thimble, an epithermal tri-element irradiator, and five horizontal beam ports. The TRIGA reactor, which has been fully operational at the current site since 1992, has recently undergone several modifications, most notably the replacement of the reactor core graphite reflector [81]. Figure 3.1 presents the UT-TRIGA reactor housing (also serves as the primary shielding), the core, and the original reflector. The nuclear reactor's purpose is for conducting research related to all topics concerning nuclear radiation and engineering.

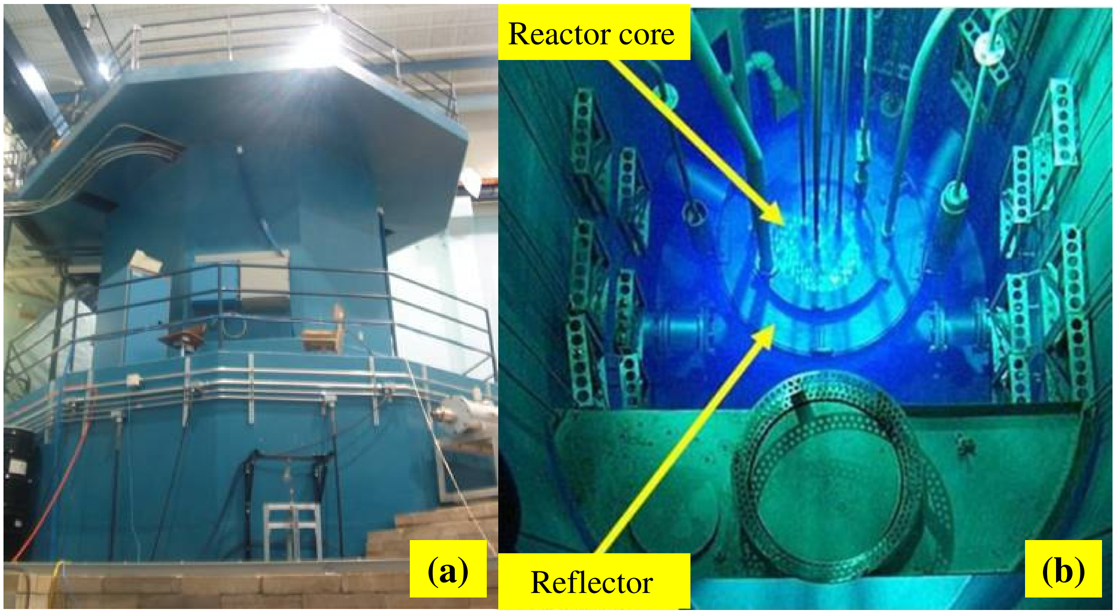

Figure 3.1: UT-TRIGA: (a) reactor housing and (b) core and reflector.

One of the prominent experimental facilities that has been setup at the NETL is the TCNS that is primarily used for PGAA [82, 83]. The TCNS facility is located at the reactor's beam port #3 (BP3) as shown in Figure 3.2. Also seen in Figure 3.2 are the other NETL beam port facilities. Beam port #1 (BP1) is currently being used for the Texas Intense Positron Source (TIPS) [84]. Beam port #2 (BP2) is dedicated to the Neutron Depth Profiling (NDP) facility which has undergone maintenance over the last few years and is now fully operational [85, 86]. Beam port #4 (BP4) is currently vacant but studies have recently been conducted in order to investigate the feasibility of utilizing it as a fast PGAA facility [87]. Beam port #5 (BP5), primarily used as the Neutron Imaging Facility (NIF) [88], has also been used in conjunction with the Reactor-Accelerator Coupling Experiments (RACE) project as of late [89].

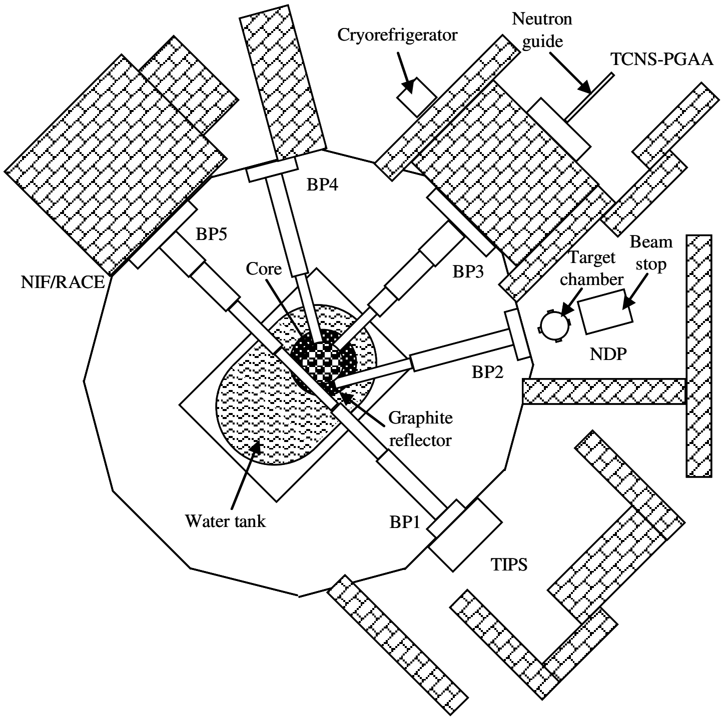

Figure 3.2: NETL layout of experimental facilities (top view; not to scale).

3.2 Texas Cold Neutron Source

The TCNS was first operational in 1994 after undergoing design, construction, and testing phases at the NETL with support from the Texas Advanced Research Program and the Department of Energy [82, 90].

The TCNS is used primarily in conjunction with the PGAA system that was installed in 1995 [82]. The TCNS was originally installed to effectively moderate the high energy (> 1 MeV) neutrons from the reactor core to very low energies, transport the low energy neutrons away from the high gamma and neutron fields using a series of neutron wave guides, and utilize these subthermal neutrons for purposes of PGAA [82].

Since then, several system upgrades have been performed on the TCNS [91] and, more recently as part of this research work, the PGAA system (discussed in Chapter 5) [92]. The TCNS system upgrades have allowed for faster cooling of the cold-head and of the moderator chamber as well as more reliable and efficient data acquisition while the PGAA improvements have reduced background noise and enhanced overall detection capabilities. During the experiments conducted for this study, the cold source was not in operation in order to reduce the possible effects of neutron scattering, which become prevalent when analyzing hydrogenous samples with cold neutron beams [39, 46, 93].

The TCNS consists of a vacuum system, a cryorefrigerator system, a thermosyphon, and a moderator chamber [94]. The purpose of the TCNS is to maintain the temperature of the moderator chamber, designed to be filled with mesitylene (1, 3, 5-tri-methylbenzene; C_9H_{12}), at cryogenic temperatures of 45.4 ± 0.2 K when the reactor is operating at 950 kW and 36.4 ± 0.2 K when the reactor is shutdown in order to effectively moderate incoming thermal neutrons produced in the core of the NETL's 1.1 MW Triga Mark II research reactor [91]. In theory, incoming neutrons will approach the frozen mesitylene's temperature as they travel through the moderator. It is expected that a large fraction of the neutrons entering the moderating medium will exist at a lower energy once they exit the chamber [37].

The mesitylene temperature is maintained through the use of a gravity driven thermosyphon that uses neon as its working fluid to transfer heat from the moderator to a copper heat exchanger. In turn, the copper heat exchanger is coupled to a cold-head that is cryogenically cooled by a helium cryorefrigerator.

The heart of the vacuum system is a vacuum box manufactured by Cryomech, Incorporated and designed for the purpose of housing the cold-head (Cryomech, Inc.), which must be operated in an evacuated environment of approximately 10^{-6} torr. The vacuum box is located within a concrete bunker adjacent to the exit face of BP3. Required vacuum levels within the vacuum box are obtained through the combined use of a roughing pump and a Leybold manufactured TURBOVAC 50 (DN 63 ISO-K/DN 16 KF; Turbotronik/NT 50 controller) turbo-molecular pump attached to a port on the right face of the vacuum box (as looking out from the reactor core).

Since the turbo pump's initial installment, it has failed a number of times and had to be replaced. The pump's bearing system is always the point of failure. In an attempt to determine the reason for the failures two type "E" Chromel-Constantan thermocouples have recently been installed for the purposes of monitoring the turbo pump's surface temperature and the ambient temperature within the concrete bunker housing the vacuum box. One diode is directly mated to the turbo-pump's outer casing and the other is suspended near the upper front left corner of the bunker (as looking out from the reactor). It was found that their temperature did not vary significantly from room temperature and thus overheating is not the cause of the pump's failures.

Therefore, it has been hypothesized that the pump is failing due to overexposure in a high radiation environment. It is thought that the bearing lubricant is being damaged by high levels of neutron and gamma-ray radiation. For that reason, during the course of this work, the turbo pump was relocated below the vertical centerline of the vacuum box as that is the highest radiation area since it lies on the same plane as the beam port opening. A 90° stainless steel elbow piece (MDC Vacuum Products, LLC; NW63, 82300) and an 8-in stainless steel nipple (MDC Vacuum Products, LLC; NW63, 82100) were installed to reposition the turbo pump and reduce radiation exposure (Figure 3.3). Components adjacent to the turbo pump were repositioned accordingly and the roughing pump was placed external to the bunker to gain accessibility for maintenance purposes.

Figure 3.3: Newly installed elbow and nipple mated to the turbo pump.

The TCNS vacuum system is also equipped with two remote control gate valves (DN 63 and DN 16, respectively) manufactured by the Swiss company VAT. The gate valves are used for isolating the vacuum system during TCNS startup and shutdown procedures. One gate valve (GV1) is located between the vacuum box and the turbo-molecular pump and the other (GV2) is located between the turbo-molecular pump and the roughing pump. Both valves are pneumatically actuated and have position indicator switches at each extent. The gate valves are monitored and controlled by a Keithley PDISO-8 that contains 8 optically isolated inputs and 8 electromechanical relay outputs with 3A ratings. The PDISO-8 plugs into the system computer backplane.

The vacuum levels are monitored by an ion gauge (Bayard-Albert IGT 274) and two model CGT 275 convectron gauges. The ion gauge and one of the convectron gauges (CG1) are located on the left face of the vacuum box (from the point of view of the core) in order to monitor the evacuated volume in the vacuum box. The other convectron gauge (CG2) is located on the opposite side of the vacuum box between the turbo pump and the roughing pump. All of the vacuum sensors are connected to an extended capability vacuum gauge controller (307-VGC) that has an operating range of 5×10^{-12} to 760 torr. The 307-VGC connects to the system computer through an RS-232C serial port.

The cryorefrigerator system consists of a compressor package and a cold-head that is vertically inserted into the vacuum box, as previously discussed. The compressor, located external to the concrete bunker, is used for the purpose of compressing and purifying the helium working fluid used to cool the cold-head. Chilled water is used to cool the compressor during cryorefrigerator operation. The original TCNS system was designed with a helium cryorefrigerator (Cryomech GB04) capable of removing a 9 W heat load at a temperature of 20 K [90, 94].

The cold-head, cooled by helium that is transferred back and forth from the cryorefrigerator by way of stainless steel braided lines, consists of two groups of parts; the motor assembly and the base tube assembly. The heat exchanger, made of oxygen free high conductivity copper, is attached to the bottom of the 304 stainless steel tube assembly. The copper heat exchanger is in direct contact with the neon-filled thermosyphon that acts to keep the mesitylene chamber at its target temperature. Originally, a silicon diode attached to the heat exchanger served as the temperature indicator and controller for a Scientific Instruments Model 9600 heater used to maintain the neon contained in the thermosyphon above its critical temperature (24.5 K). The diode's operation range is 1.5 to 450 K and has a selected sensor excitation current of 100 μA that can be switched to 10 μA. The heater provides 25 W of heating (25 V @ 1 A) and connects to the system computer through a RS-232C serial port.

The thermosyphon is constructed of aluminum with a total length of 3 m, an outer diameter of 19 mm, and 1.6-mm thick walls. The gravity driven thermosyphon is inclined with a slope of 2.5° [94]. One end of the thermosyphon is mated to the heat exchanger, as previously mentioned, by an aluminum yoke and the other is welded to the moderator chamber. Neon is transferred in and out of the thermosyphon by way of a 6.4-mm stainless steel tube. The neon contained within the thermosyphon, by way of gravity and a two phase transformation, transfers the heat generated by the moderator, due to gamma-ray heating, to the end where the cold-head is located. The two phase transformation performed by the neon consists of condensation and subsequent vaporization.

The original TCNS design made use of a temperature controlled heater that would activate whenever the heat exchanger's temperature would approach neon's critical point of 24.5 K in order to keep the neon from freezing [94]. A diaphragm pressure transducer (Omega PX302-100G V) is located on the neon handling system feed line to measure neon's pressure during TCNS operation. The signal is conditioned by an IOTech Model DBK16 and connected to a DAQ2000 acquisition board.

The moderator chamber is made of aluminum and is cylindrical in shape with a 3.75-cm radius and a width of 2 cm. The chamber can hold a volume of approximately 80 ml of mesitylene [90]. The mesitylene serves to moderate incoming thermal neutrons produced in the reactor core and effectively shift their energies to the subthermal region. Mesitylene was chosen as the moderating material due to its favorable neutron interaction properties, similar to other common moderating materials (*i.e.* liquid H_2, D_2O, methane, etc.). Also, due to its high ignition point (823 K) and large separation between its boiling point (437 K) and melting point (228 K), mesitylene is a safe material in regards to its ability to be handled in liquid form at room temperature thus reducing potential hazards when compared to the other moderating materials.

Mesitylene also has a relatively low atomic mass, low capture cross-section, and high scatter cross-section as it is composed of carbon and hydrogen [82, 90, 94]. It has also shown good resistance to radiation exposure and its effects as recent studies suggest that mesitylene does not undergo spontaneous reaction of recombination (burp) due to its relatively low energy accumulation (< 1 J g^{-1}) as compared to other moderator materials such as frozen water and methane [95]. This feature reduces the potential for moderator chamber damage. Mesitylene has also been shown to produce favorable moderated neutron spectra due to its abundance of low lying energy levels [96]. Solid mesitylene can exist in a variety of crystalline phases depending on the type of cooling condition and temperature control [97, 98]. Disordered phase II mesitylene seems to be the most promising as a cold source moderator [97].

As part of this work, an experiment was conducted to verify that the mesitylene will not substantially corrode the interior surface of the aluminum moderator chamber over time. In this experiment six small pieces of 6061 aluminum were submerged in liquid mesitylene. Three of the pieces were placed in a small beaker containing fresh mesitylene and the other three pieces were placed in a beaker with pre-irradiated mesitylene to better simulate the moderator environment. Each set of three was composed of various sized aluminum pieces to observe the effects that might occur on a given volume where the smallest piece in each set was a metal shaving that was assumed to be comparable to an already deteriorated/damaged aluminum metal surface. The aluminum pieces were cleaned to remove any surface debris and then weighed before being submerged in their respective mesitylene-filled beakers. The aluminum was allowed to sit in its mesitylene environment for two years before being extracted, cleaned, and reweighed to measure the weight loss (if any). Each piece was allowed to undergo this process. The results of the investigation are presented in Table 3.1.

Table 3.1: Mesitylene corrosion test results.

Fresh Mesitylene				**Irradiated Mesitylene**			
Al sample	Mass before (g)	Mass after (g)	Δ (g)	Al sample	Mass before (g)	Mass after (g)	Δ (g)
1	0.06139	0.06137	0.00002	1	0.06362	0.06352	0.00010
2	0.02389	0.02387	0.00002	2	0.03242	0.03232	0.00010
3	0.00275	0.00274	0.00001	3	0.00332	0.00330	0.00002

From the data given in Table 3.1, it is evident that there was no significant weight loss and thus no corrosion of the material due to the interaction of the aluminum metal with either the fresh mesitylene or irradiated mesitylene. These results are promising and provide proof that the mesitylene will not substantially corrode or degrade the structural integrity of the aluminum moderator chamber over prolonged periods of time.

A closed loop system consisting of a glass reservoir, a peristaltic pump, an absorption trap, transfer lines, and a series of flow control valves are used to insert and extract liquid mesitylene into the moderator chamber [90]. A diaphragm pressure transducer (Omega PX302-50G V) is positioned on the mesitylene handling system feed line. The signal is conditioned by an IOTech Model DBK16 and connected to a DAQ2000 acquisition board. Three type “E” Chromel-Constantan thermocouples are attached to the mesitylene moderator chamber. The first sensor is located on the flat face of the moderator chamber closest to the reactor core while the other two sensors are located on the flat face of the moderator furthest from the core [94]. All three thermocouples are attached to an IOTech Model DBK81 – Built-in Cold Junction Compensation board. These temperature sensors support up to seven thermistors per board. Their measuring capabilities support 0.1 degree of precision and 0.5 degree of accuracy from 270 to 650 K. All three sensors connect to an IOTech Model DAQ2000 16-bit 200 ksps ADC (64k 5 μs conversion) that in turn plugs into the system computer's backplane.

The moderator chamber, thermosyphon, and mesitylene and neon transfer lines are all encased within a stainless steel vacuum jacket [90]. Figure 3.4 illustrates the TCNS vacuum box and its interior components including: the vacuum box, cold-head, heat exchanger, thermosyphon, curved neutron guide, and moderator chamber. Figure 3.4 is not to scale and excludes the vacuum jacket casing, straight neutron guide piece, vacuum system accessories, and associated diodes in order for the main components to be better visualized. Figure 3.5 presents an actual image of the vacuum box and the exterior components that are coupled to it (prior to facility reconstruction). A wire diagram of the TCNS system can be found in Appendix A.

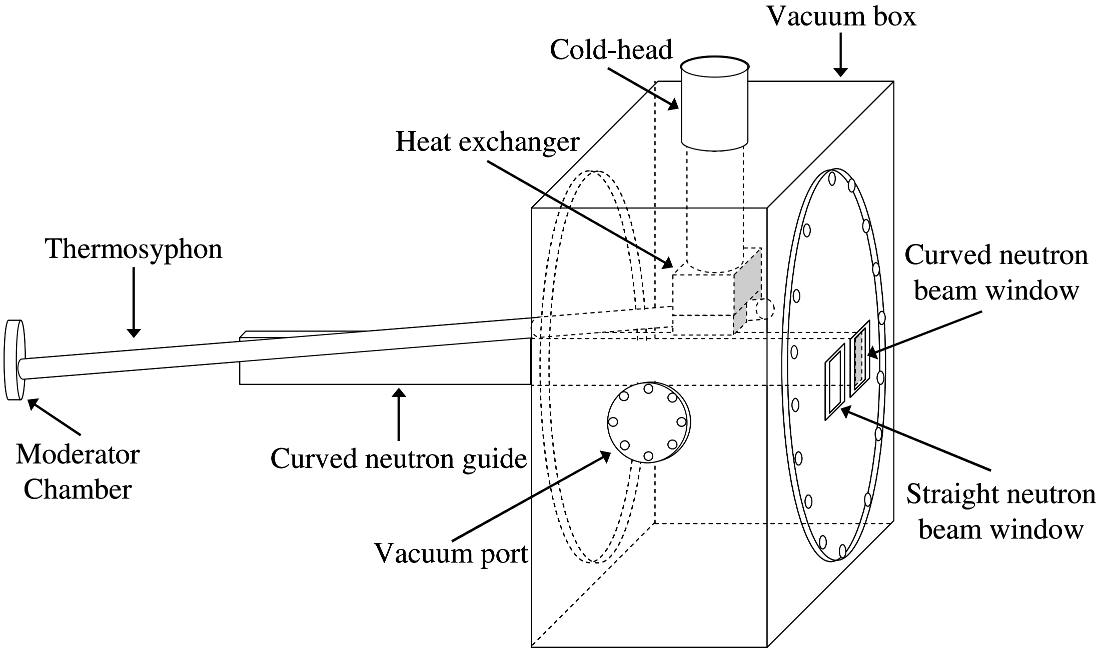

Figure 3.4: TCNS vacuum box and interior components (not to scale).

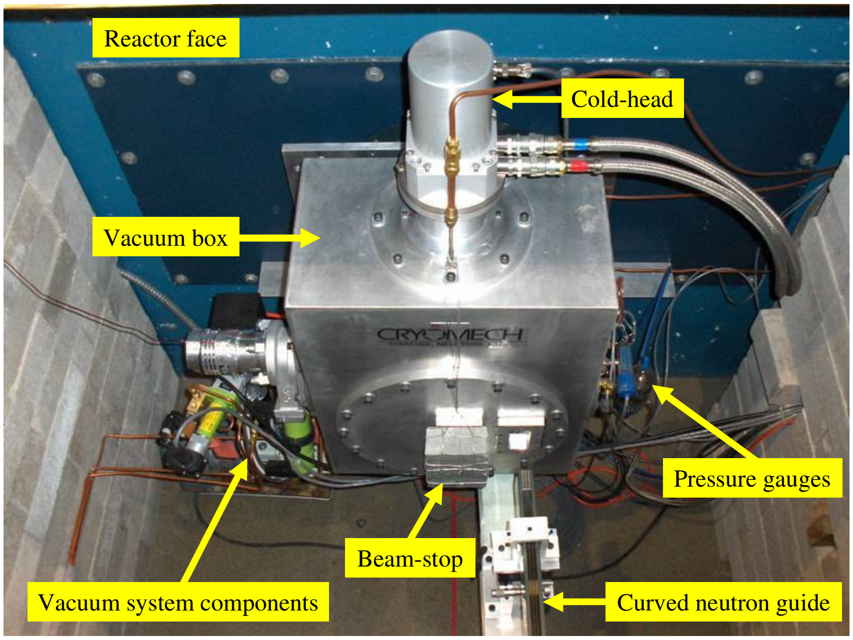

Figure 3.5: TCNS vacuum box and exterior components.

Thermal neutrons, produced in the UT-TRIGA core via fission, are filtered and transported by two in-pile guides, a curved and a straight one. At the reactor face, the straight beam is stopped within a bunker, made of a massive biological shielding and built of concrete blocks. The thickness of the concrete shielding around the bunker is 76 cm. The curved guide continues as an out-of-pile section, as shown in Figure 3.6, and transmits the neutrons to the PGAA sample irradiation position located within the same hall. The evacuated, bender-type guide has a total length of 6 m (consisting of three 2-m long sections), a cross-section of 5.0×1.5 cm^2, and is divided into three vertical channels. The guide has a curvature radius of 300 m with inner walls that are 1000 Å thick and coated with ^{58}Ni [90, 99]. The guide is designed with a characteristic wavelength of 2.7 Å, which corresponds to an average neutron energy of 11 meV [94]. Due to the curved nature of the guide, the fast neutron and gamma-ray background is extremely low [42, 100]. The beam shutter, made of Boral, a boron containing aluminum sheet [37], is driven by an electric motor and located between the second and third guide sections outside the bunker (Figure 3.6). The shutter is used to turn off the neutron beam when facility access is desired, while the reactor is operating. The beam stop after the sample position was also originally made of Boral (Figure 3.7) [92].

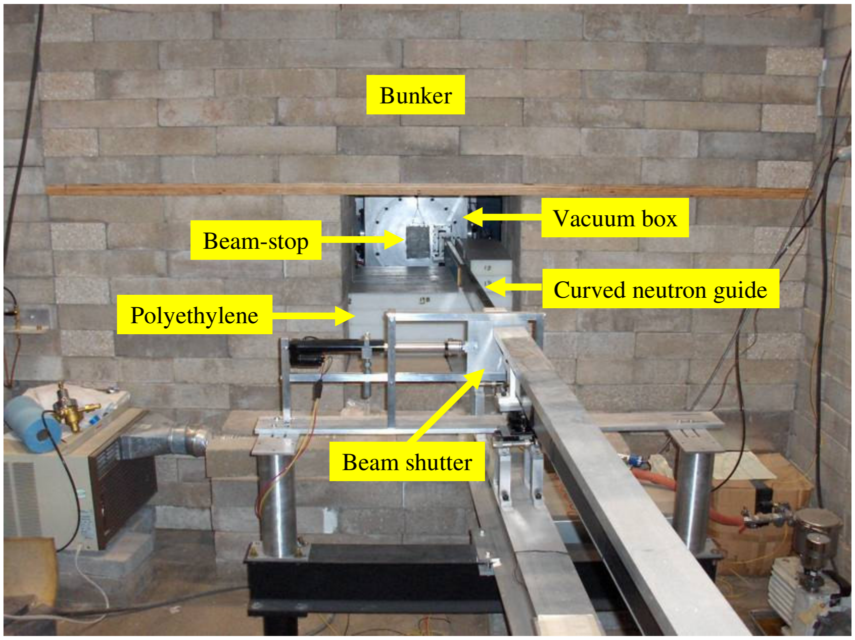

Figure 3.6: View of open bunker and components located in the proximity.

In the original design, a focusing guide element with a length of 80 cm (cross-sections of 5.0×1.5 cm^2 and 2.57×0.87 cm^2 at the entry and exit, respectively) made of $3\theta_c$ supermirror could optionally be introduced in the beam path between the end of the curved guide and the sample position [42]. Recently, the focusing guide piece has been replaced by a windowless, float glass (containing no boron), supermirror coated ($m = 3$), converging, doubly focusing, parabolic flight tube, manufactured by SwissNeutronics.

The new flight tube, seen in Figure 3.7, has a length of 75 cm, an entrance size of 5.0×1.5 cm^2 and an exit size of 2.57×0.87 cm^2. Originally, the variation of the neutron-beam intensity was followed using a ^{3}He counter at the end of the focusing guide [101]. Since then, the ^{3}He counter has been relocated and perpendicularly positioned between the exit of the curved guide and the entrance of the new focusing guide (Figure 3.8) [92].

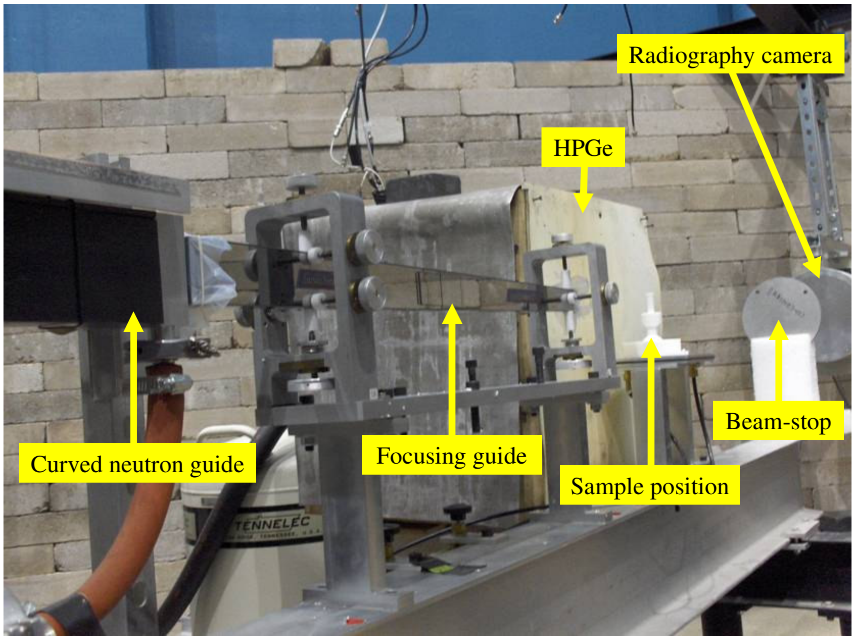

Figure 3.7: Photograph of the curved neutron guide, focusing guide, shielded HPGe detector, beam-stop, and radiography camera, respectively, relative to the sample position.

The sample position is located at a distance of 33.5 cm from the end of the focusing guide (Figure 3.8). A set of different sample holders are available for different measurements: the samples can be put in Teflon® vials on Teflon® supports, or affixed among Teflon® strings, tightened in aluminum or Teflon® frames, similarly to other PGAA facilities worldwide [92, 100, 102]. The thermal flux at the sample position, originally reported to be (9±2)×10^6 cm^{-2} s^{-1}, was measured at low reactor power by using the ^3He counter and then extrapolating the results to 1 MW [90, 92].

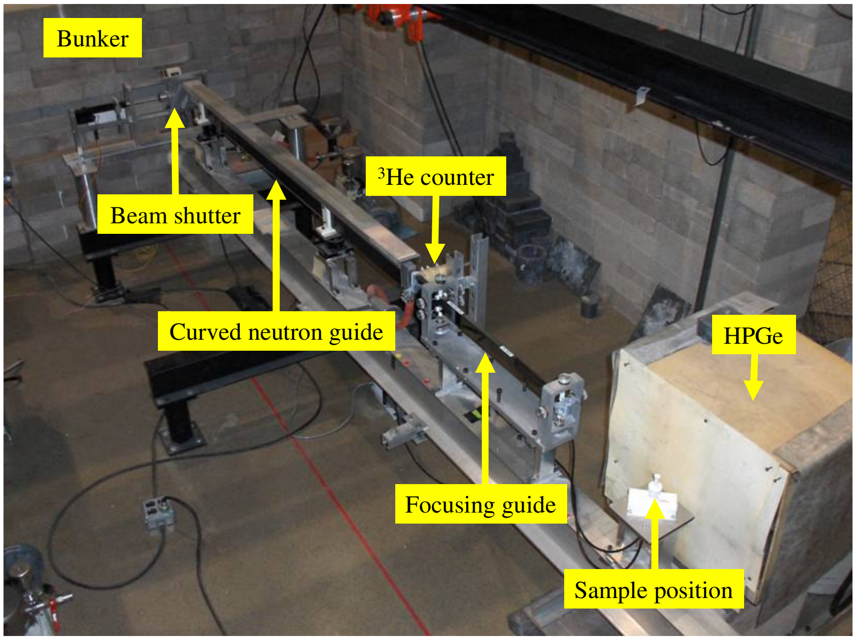

Figure 3.8: Photograph of the PGAA components, located external to the bunker, as situated relative to each other.

A newly installed p-type, 65 % efficient ORTEC HPGe detector with 1.95-keV resolution has replaced the original n-type, 25 % efficient, 1.9-keV ORTEC HPGe detector [101]. The HPGe specifications can be found in Appendix B. The HPGe detector is covered with lead shielding and neutron absorbers and is used to detect the gamma-rays emitted by the sample of interest. Gamma-rays from the sample pass through a hole in the lead casing. The HPGe is shielded in this manner in order to adequately reduce background noise and improve detection limits. A spectroscopic amplifier (Tennelec TC 244) and a 16k ADC (Canberra 8713) process the signals, which are collected by an AIM (Canberra 556A) unit controlled by the Canberra Genie 2000 V2.1A Gamma Acquisition and Analysis software [92].

The HPGe detector is situated perpendicular to the neutron beam and sits on an aluminum platform fitted with aluminum wheels that allow for back and forth movement, relative to the neutron beam, along a stationary rail. The HPGe detector setup provides the ability of varying the position of the sample and detector as it can be translated with respect to the sample while maintaining constant line of sight. Detector sensitivity and dead time can be increased or decreased depending on the detector's distance from the sample. There are a variety of configurations that may be used to hold a given sample in the focal region of the beam while positioned on the aluminum sample table. The complete setup of the TCNS-PGAA facility, before reconstruction, is shown in Figure 3.9.

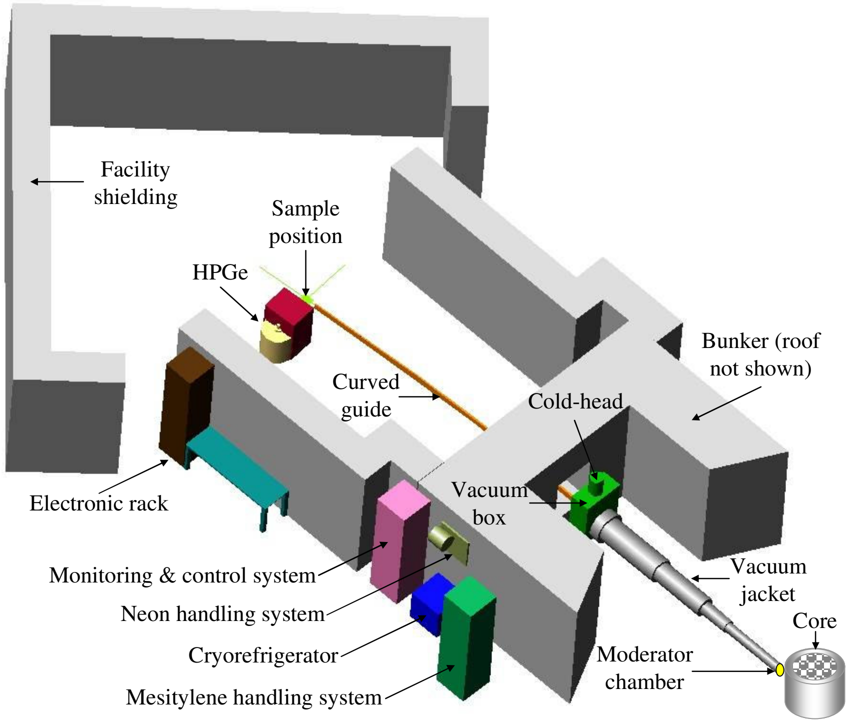

Figure 3.9: Illustration of the complete TCNS-PGAA facility before reconstruction.

Chapter 4: Experimental Methods

4.1 Sample Synthesis

In general, all parent oxide cathodes utilized for the purposes of this study were synthesized by co-precipitation methods. Only $LiCoO_2$ was synthesized by a solid-state reaction where required amounts of Li_2CO_3 (Alfa Aeasar) and Co_3O_4 (GFS Chemicals) were ground together and then fired at 900 °C for 24 h in air. All other nickel and manganese containing compounds were synthesized by a co-precipitation method where required amounts of metal acetates such as $Ni(CH_3CO_2)_2{\cdot}xH_2O$ (Alfa Aesar), $Mn(CH_3CO_2)_2{\cdot}xH_2O$ (Acros Organics), and $Co(CH_3CO_2)_2{\cdot}xH_2O$ (Alfa Aesar) were dissolved in de-ionized water and then slowly dripped into a stirred solution of 0.1 M LiOH (Fischer Scientific) solution using a burette. This procedure allows for the co-precipitation of the metal ions as fine hydroxides ($Ni_{1-y-z}Mn_yCo_z(OH)_2$) with a homogeneous cation distribution. The precipitate was then filtered and repeatedly washed with water to remove residual lithium salts, if any, and oven dried in air at 100 °C for at least 24 h. Required amounts of $LiOH{\cdot}H_2O$ (Fischer Scientific) were then ground with the dried mixed metal hydroxide precipitate and subsequently fired, depending on the compound, at a specified temperature. Controlled delithiation of the parent compounds was then carried out using the same technique as previously described in Section 1.3.

4.2 PGAA Relative Standardization Method

For purposes of this study, the hydrogen concentration in the various oxide cathode samples was determined by way of the PGAA relative standardization method

[37]. In this case, the measured mass, m_x, of element x in the sample is determined from a comparison of the observed counting rate of a specific gamma-ray peak of that element with that of a standard that contains a known mass, m_{std}, of the same element. Therefore, by analyzing a standard with a well known hydrogen concentration, one can determine the hydrogen mass in an unknown sample. For this type of comparison, both the sample and standard should be composed of a similar matrix with similar scattering power (*i.e.* H content) to normalize the effects of neutron scattering and a limited amount of highly neutron absorbing constituents in order to minimize self-shielding. Also, both the sample and the standard should be irradiated under nearly identical environmental conditions [93]. The prompt gamma-ray emission rate (R) for a particular sample is given by:

$$R = m\theta N_A \phi_{avg} \sigma_{avg} \Gamma \varepsilon \big/ MW \tag{4.1}$$

where m is the mass of the element of interest (g), θ is the isotopic abundance of the target isotope (dimensionless), N_A is Avogadro's number (mol^{-1}), ϕ_{avg} is the average neutron fluence rate within the sample (cm^{-2} s^{-1}), σ_{avg} is the spectrum-averaged neutron capture cross-section (cm^2), Γ is the gamma-ray yield (photons/capture), ε is the detector efficiency (counts/photon), and MW is the atomic weight of the element of interest (g mol^{-1}) [93].

When a sample to standard prompt gamma-ray emission rate ratio is taken, the parameters N_A, θ, Γ, and M cancel out. Further, for a well thermalized neutron beam σ_{avg} is not significantly affected and its ratio cancels out as well [93]. A correction must be made, however, for the differences in average neutron fluence rate for each sample being irradiated. The differences are primarily due to: (1) temporal and spatial variations in neutron fluence rate, (2) neutron self-shielding, and (3) neutron scattering [93]. A correction factor is usually determined by utilizing an in-beam fluence monitor or by approximating a fluence rate by measuring the count-rate of a titanium foil at regular intervals over the course of an experiment [37, 93]. For the purposes of this study, the variation of the average fluence rate was followed by way of the ^{3}He neutron counter mentioned in Section 3.2. In this case, the sample to standard prompt gamma-ray emission rate ratio is equal to the ratio of the masses multiplied by the fluence correction factor and thus, after some rearrangement, the following is obtained:

$$m_x = \frac{R_x}{R_{std}} \frac{m_{std}}{f_\phi} \tag{4.2}$$

where m_x is the mass of the element of interest in the sample, R_x is the prompt gamma-ray emission rate of the element of interest in the sample (counts/second), m_{std} is the mass of the element of interest in the standard (g), R_{std} is the prompt gamma-ray emission rate of the element of interest in the standard (counts/second), and f_ϕ is the fluence correction factor (*i.e.* $f_\phi = \phi_{avg,x}/\phi_{avg,std}$; dimensionless).

Since prompt gamma-rays are being used and not decay gamma-rays, counts/second can be directly used instead of activity and decay time does not have to be accounted for, which is common in INAA. Therefore, once the spectrum is collected, the net emission rate under the hydrogen peak is evaluated by subtracting the hydrogen count rate of the background spectra from the sample spectra. This information is then used in the above equation to calculate the hydrogen mass of the sample.

4.3 Cobalt Interference Correction

The ^{59}Co interference was addressed by utilizing the PGAA reference peak method [37]. In this case, a 99.9 % pure cobalt foil was irradiated under the same experimental conditions as the cathode samples. A ratio was then taken for two ^{59}Co gamma-ray peaks found within the same gamma spectrum where one of the peaks is the 2221.61 keV line that interferes with hydrogen at 2223.25 keV and the other is an interference free peak. For the purposes of this study, the cobalt 447.71 keV peak was selected as the interference free peak. In theory, the measured cobalt ratio should remain constant from sample to sample regardless of the amount of cobalt present in the matrix, provided that the amount of gamma-ray attenuation does not change. Figure 4.1 shows the background corrected ^{59}Co-2221.61 keV interference gamma peak .

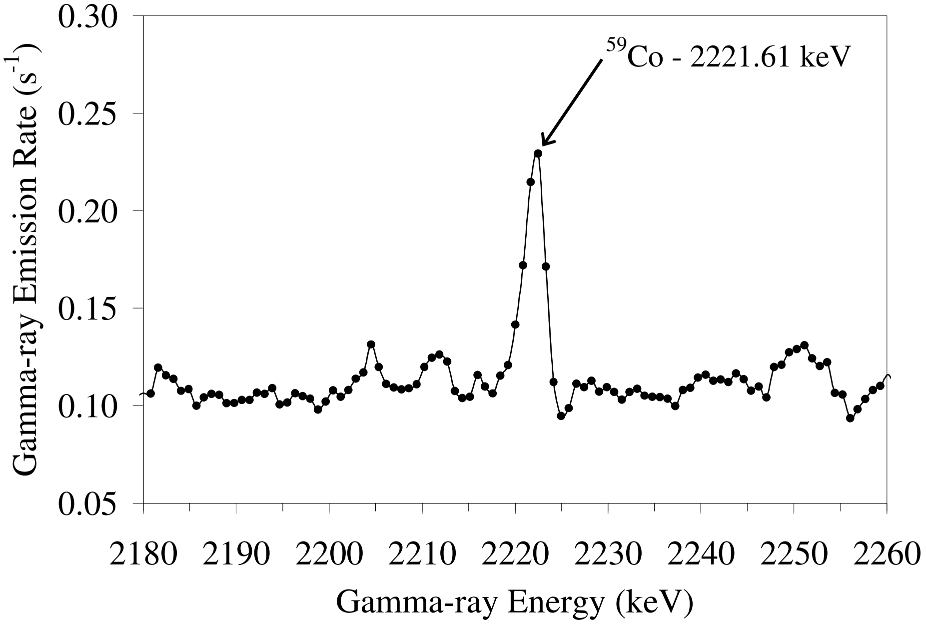

Figure 4.1: ^{59}Co-2221.61 keV interference gamma-ray.

When taking ratios of the particular cobalt gamma peaks, the gamma-ray energy dependent variables such as detector efficiency and gamma-ray yield cancel out; the microscopic cross-section and neutron fluence also drop out of the equation. Using the measured cobalt ratio, the area under the 2221.6 keV can then be directly calculated and properly subtracted from the total peak area in order to accurately quantify hydrogen. This calculation is visualized in Figure 4.2. An example of this calculation and the associated equations using a variation of the prompt gamma-ray emission rate (*R*) given by Equation 4.1 is presented below:

$$\frac{R_{1,foil}(2221.61\,\mathrm{keV})}{R_{2,foil}(447.71\,\mathrm{keV})} = \frac{\phi_{1,foil}\sigma_{\gamma 1,foil}N_{1,foil}\varepsilon_{1,foil}}{\phi_{2,foil}\sigma_{\gamma 2,foil}N_{2,foil}\varepsilon_{2,foil}} \tag{4.3}$$

$$\frac{R_{1,samp}(2221.61\,\mathrm{keV})}{R_{2,samp}(447.71\,\mathrm{keV})} = \frac{\phi_{1,samp}\sigma_{\gamma 1,samp}N_{1,samp}\varepsilon_{1,samp}}{\phi_{2,samp}\sigma_{\gamma 2,samp}N_{2,samp}\varepsilon_{2,samp}} \tag{4.4}$$

$$\frac{R_{1,foil}(2221.61\,\mathrm{keV})}{R_{2,foil}(447.71\,\mathrm{keV})} = \frac{R_{1,samp}(2221.61\,\mathrm{keV})}{R_{2,samp}(447.71\,\mathrm{keV})} \tag{4.5}$$

rearranging, where: $\begin{bmatrix} \phi_{1,foil} = \phi_{2,foil} & N_{1,foil} = N_{2,foil} \\ \phi_{1,samp} = \phi_{2,samp} & N_{1,samp} = N_{2,samp} \\ \sigma_{\gamma 1,foil} = \sigma_{\gamma 1,samp} & \varepsilon_{1,foil} = \varepsilon_{1,samp} \\ \sigma_{\gamma 2,foil} = \sigma_{\gamma 2,samp} & \varepsilon_{2,foil} = \varepsilon_{2,samp} \end{bmatrix}$

$$R_{1,samp}(2221.61\,\mathrm{keV}) = \frac{R_{1,foil}(2221.61\,\mathrm{keV})}{R_{2,foil}(447.71\,\mathrm{keV})} R_{2,samp}(447.71\,\mathrm{keV}) \tag{4.6}$$

where $N = m\theta N_A/MW$ is the number of atoms of the element of interest (dimensionless), $\sigma_\gamma = \sigma\Gamma$ is the partial capture cross-section (cm^2-photons/capture), $R_{1,samp}$, $R_{2,samp}$, $R_{1,foil}$, and $R_{2,foil}$ refer to the background subtracted gamma-ray emission rates measured at the given gamma-ray energies for the sample and foil (counts/second), respectively, ϕ is the average neutron fluence rate within the sample (cm^{-2} s^{-1}), and ε is the detector efficiency (count/photon).

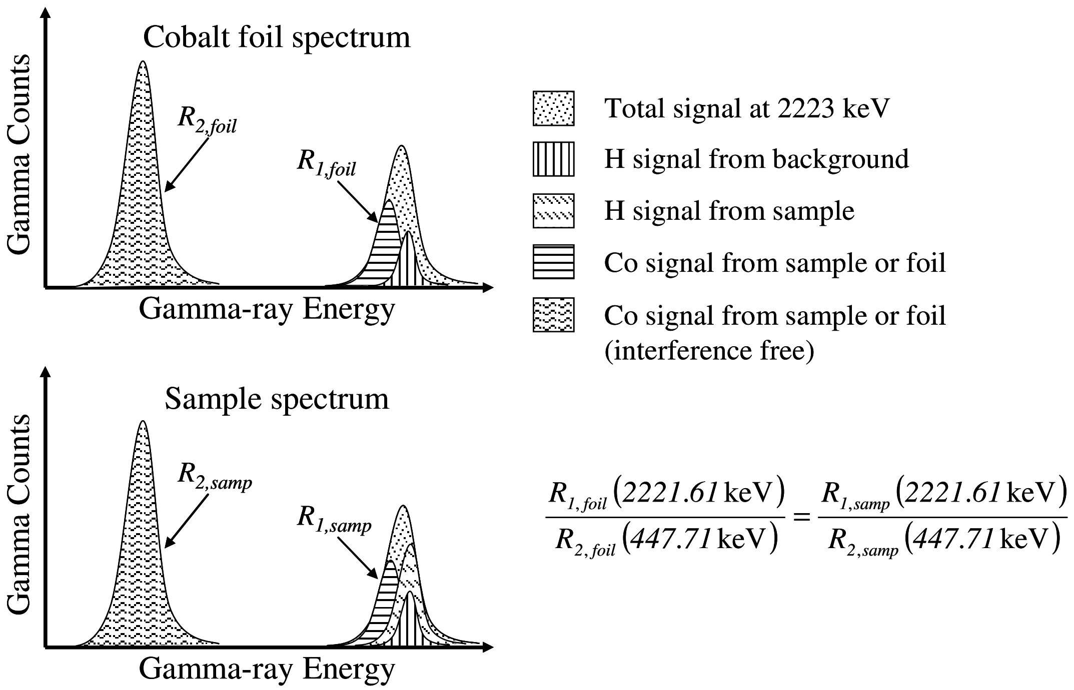

$$\frac{R_{1,foil}(2221.61\,\mathrm{keV})}{R_{2,foil}(447.71\,\mathrm{keV})} = \frac{R_{1,samp}(2221.61\,\mathrm{keV})}{R_{2,samp}(447.71\,\mathrm{keV})}$$

Figure 4.2: Illustration of ^{59}Co-2221.61 keV interference peak area determination by utilization of cobalt peak area ratios.

Therefore, the net hydrogen signal for the sample is simply calculated by subtracting the hydrogen background count rate and the calculated cobalt count rate (using Equation 4.6) from the sample's gross hydrogen count rate. Error propagation must be accounted for during this type of net signal determination. The $R_{1,foil}$ (2221.61

keV) to $R_{2,foil}$ (447.71 keV) ratio determined and utilized during this study was equal to 0.0237 ± 0.0001.

4.4 PGAA Sample Preparation and Analysis

In order to avoid moisture adsorption onto the surface of the samples, they were carefully handled under argon atmosphere during the delithiation process. During irradiation, all samples were in ground-powder form (for purposes of homogeneity) and packaged in custom made Teflon® sample vials rather than in other more traditional holders, like polyethylene vials, to avoid direct activation of background sources such as hydrogen and other low atomic number species. The vial geometry is specially designed to accommodate the neutron beam profile and assure that the sample is completely immersed in the beam. The vials were machined in the chemistry machine shop located on the UT campus.

Also, to reduce the effects of neutron scattering, neutron and gamma-ray self-absorption, and maintain uniformity, all batch samples were irradiated at the same geometrical location under the same environmental conditions. The position of the sample and its holder was optimized relative to the neutron beam and the HPGe through the utilization of neutron radiography imaging. Sample weight was usually between 0.3 and 0.5 g and the sample geometry was cylindrical in shape with a diameter of 8 mm and thickness of 8 mm, respectively. It should be noted that during this study an α-ionizer was employed during the weighing and packaging of samples to reduce the static repulsion created by the fluorine in the Teflon® vials.

Further, boron contamination or other impurities that could arise from any remaining $LiBF_4$ after delithiation and washing, was qualitatively monitored by PGAA and XRD to assure that the analyzed samples were clean and contained only the expected constituents. Figure 4.3 shows PGAA spectra containing the background boron signal and an example of what was found to be an acceptable range of boron signals using a number of $Li_{1-x}Ni_{0.5}Mn_{0.5}O_2$ samples.

The boron signal in most instances is likely elevated due to an increase in the Compton continuum as well as forced neutron scattering by the sample and subsequent neutron capture by the surrounding Boroflex material used as neutron shielding for the detector. A ^{58}Ni gamma-ray peak originating from the $Li_{1-x}Ni_{0.5}Mn_{0.5}O_2$ samples but absent in the background spectrum is also shown in the spectra plot. Current studies performed at UT have shown that the presence of boron concentrations greater than 1 to 2 wt% introduce significant self-attenuation effects.

The PGAA experimental setup utilized during this investigation involved the use of a helium filled Teflon® bag to displace the surrounding air and reduce the possibility of spontaneous cathode reduction. The Teflon® bag setup will be fully described in Section 5.1. During PGAA, samples were irradiated for ≤ 2 h at a reactor power of 950 kW. The stationary ^{3}He proportional neutron counter wrapped in Boroflex was used to collect the real time neutron fluence impinging on the sample [102]. Various 8 h long PGAA background counts with only the Teflon® sample stand and an empty Teflon® vial were routinely collected to carefully characterize the PGAA background hydrogen content and correct the sample spectra. It should be noted that some samples were analyzed before the PGAA facility was reconstructed while others were analyzed after the facility was redesigned. It will be indicated as needed whether the given samples were analyzed before or after PGAA facility reconstruction.

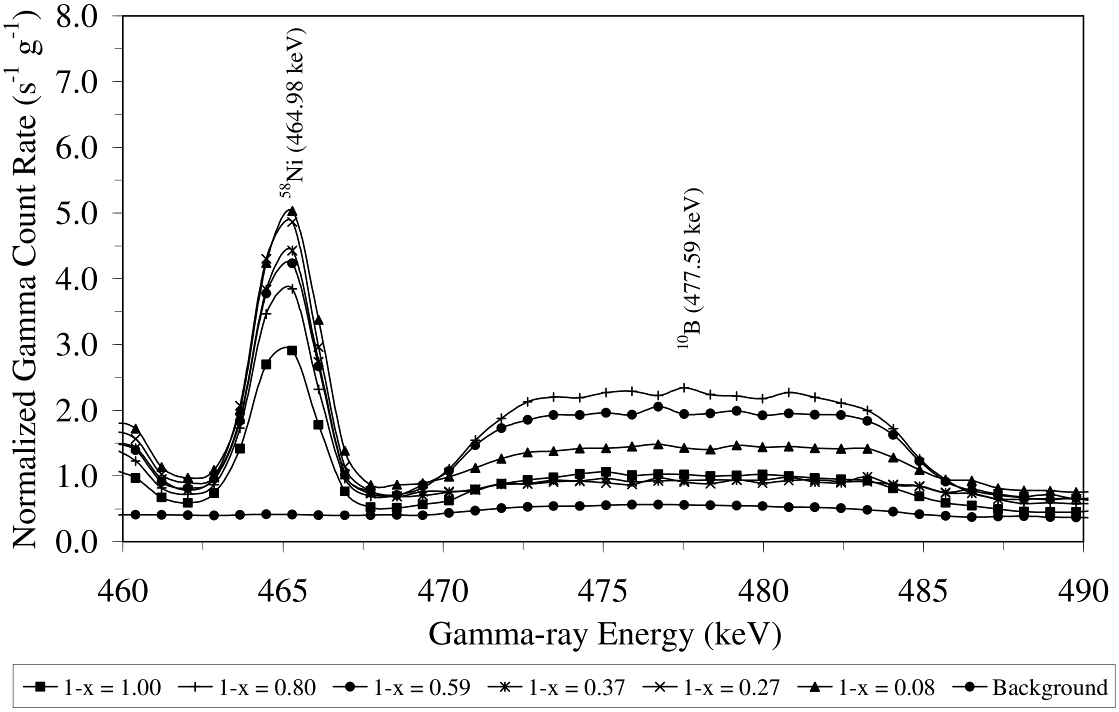

Figure 4.3: PGAA spectra of the background and the $Li_{1-x}Ni_{0.5}Mn_{0.5}O_2$ system revealing the nickel 464.98 keV peak and the boron 477.59 keV peak resulting from the Doppler broadened $^{10}B(n,\alpha)^7Li$ reaction.

4.5 Other Materials Characterization Techniques

4.5.1 X-Ray Powder Diffraction

Structural characterization was accomplished by XRD using Cu$K\alpha$ radiation with a Philips 3550 diffractometer (Figure 4.4). The XRD patterns were typically collected at a scan rate of 0.02° per 5 seconds covering a range of 10 to 80°. Samples used for XRD analysis were in ground-powder form and prepared by mixing with amyl acetate binder and thinly spreading over a microscopic glass slide. Recorded XRD patterns were then compared to an electronic materials data base composed of JCPDS files using the JADE software for purposes of phase identification.

Figure 4.4: Philips 3550 diffractometer.

4.5.2 Atomic Absorption Spectroscopy

Lithium content (1-x) in the $Li_{1-x}MO_2$ samples was determined, as previously mentioned, by AAS with a Perkin-Elmer 1100 atomic absorption spectrometer (Figure 4.5). AAS requires the use of solutions containing relatively low concentrations of the element of interest. These solutions are typically prepared by dissolving approximately 20 to 30 mg of the $Li_{1-x}MO_2$ sample into 10 ml of concentrated HCl contained in a 50 ml beaker. The mixture is heated for about half an hour at a temperature of about 60 °C in order to completely dissolve the sample. After being dissolved, the $Li_{1-x}MO_2$ solution is diluted with de-ionized water to obtain the required lithium concentration. AAS also requires the utilization of a lithium standard solution. In this case, a lithium standard with a 2.000 mg/l concentration was prepared using dehydrated lithium carbonate.

Figure 4.5: Perkin-Elmer 1100 atomic absorption spectrometer.

4.5.3 Redox Titration

Determination of the average oxidation states of the transition metal ions was accomplished by either iodometric titration [32] or by treating with a known excess of sodium oxalate and titrating the unreacted $Na_2C_2O_4$ with potassium permanganate.

In the case of iodometric titration, usually about 35 to 40 mg of $Li_{1-x}MO_2$ sample is dissolved in a solution containing 15 ml of 10 wt% KI and 10 ml of 3.5 N HCl. The KI should be mixed with the sample before the HCl is added in order to properly liberate iodine. The liberated iodine is then titrated against a 0.03 N sodium thiosulfate solution. Starch is used as the indicator where a color change from dark purple to clear signifies the endpoint. The average oxidation state $(2+n)+$ can then be calculated based on the amount of thiosulfate consumed during the titration:

$$n = (0.03 \times V \times MW)/W \tag{4.7}$$

where V is the volume of thiosulfate consumed (ml), MW is the molecular weight of the sample (g mol^{-1}), and W is the sample weight (mg).

In the case of permanganate titration, 25 to 35 mg of $Li_{1-x}MO_2$ sample is dissolved in a 20 ml solution 0.05 N $Na_2C_2O_4$ and 20 ml of 4.0 N H_2SO_4. The sodium oxalate should be added to the sample before the sulfuric acid. The unreacted sodium oxalate is then titrated against a 0.05 N $KMnO_4$ and a color change from clear to light pink is the endpoint indicator. The average oxidation state $(2+n)+$ can then be calculated based on the amount of $KMnO_4$ needed to consume the unreacted $Na_2C_2O_4$ during the titration:

$$n = (0.05 \times (20ml - V) \times MW)/W \tag{4.8}$$

where V is the volume of potassium permanganate consumed by the unreacted $Na_2C_2O_4$ (ml), MW is the molecular weight of the sample (g mol^{-1}), and W is the sample weight (mg).

4.5.4 Thermogravimetric Analysis

A Perkin-Elmer series 7 thermogravimetric analyzer (Figure 4.6) was used to study the thermal behavior of the samples. The sample mass typically used is about 50 mg. The sample is situated in a platinum crucible and subsequently heated up to a temperature of 600 °C at a rate of 3 °C/min.

Figure 4.6: Perkin-Elmer series 7 thermogravimetric analyzer.

4.5.5 Mass Spectrometry

Mass spectrometric analysis was performed on a few samples to identify the elements that evolve in the form of gas from the chemically delithiated samples while heating up to 600 °C at a rate of 20 °C/min using a Micromass AutoSpec – Ultima instrument. The gas-phase ions produced from the samples are separated with respect to their mass-to-charge ratio (m/z) by a combination of electric and magnetic fields. The mass spectrum is generated by measuring the ion currents or the flux of ions at each value of m/z over a certain mass range.

Chapter 5: PGAA Facility Reconstruction and Characterization

5.1 PGAA Facility Reconstruction

The free-standing curved neutron guide did not provide ideal background conditions, though it made possible reproducible prompt gamma measurement for several important elements, like hydrogen or boron in different materials. The relatively good characteristics and the unexploited possibilities of the facility provided encouragement for a redesign and reconstruction of the whole PGAA system to reduce both the neutron and gamma-ray backgrounds to achieve lower detection limits. The reconstruction work was accomplished with the assistance of Mr. Harrison and the guidance of Dr. Zsolt Révay [92].

Since the TCNS-PGAA facility is close to the reactor face, the shielding needs to be designed in a different way than in the case of PGAA instruments located in separate guide halls with low radiation backgrounds. The following materials were used during the reconstruction of the facility shielding [92]:

1. ^{6}Li-loaded polymer manufactured by PNPI, Saint-Petersburg, Russia [37] (also referred to as Lithoflex), for the absorption of the low-energy (especially thermal) neutrons. The material contains about 24 % of Li with 80 % enrichment of ^{6}Li. Roughly 1 m^2 of this material was available.
2. Natural Li_2CO_3 and LiF powders, readily available as fine chemicals, sealed in fluoroethylene propylene (FEP) [37] foils. They were used for the attenuation of low-energy neutrons. About 2 kg of these materials were used.
3. Borated polyethylene, manufactured by King Plastic Corporation [103] (also referred to as King Plasti-Shield® Industrial Grade). The material contains 5

wt% of boric acid and has a distinctive purple color. It was available in 2.5-cm thick sheets, and was used for the thermalization and absorption of epithermal neutrons, and also for the absorption of thermal neutrons. Approximately 12 m^2 of these sheets were used.

4. Borated polyethylene in granulated form. Its boron content is 2.6 ± 1.0 % (as determined using the UT-PGAA system). Approximately 10 kg was built in from this material.
5. Boron loaded flexible sheets (also referred to as Boroflex). It has a thickness of 1 cm and its boron content is 4.3 ± 1.0 % (as determined using the UT-PGAA system). About 2 m^2 of this material was available.
6. Concrete brick with the dimensions of $9.5 \times 19 \times 39.5\ cm^3$. It is used as a complex shielding material. Due to its water content, it is good for partial thermalization of epithermal neutrons and in greater thicknesses also for the attenuation of neutron and gamma radiations. Approximately 500 additional bricks with the total mass of about 10 tons were used and many more moved during the construction.
7. Lead bricks with the dimensions of $5 \times 10 \times 20\ cm^3$. They were used in the areas with a relatively high gamma radiation level. Altogether 200 lead bricks with a total mass of more than 2 tons were used and rearranged several times.
8. Five-cm thick polyethylene sheets were used for the attenuation of the epithermal neutrons.
9. Boral [37] sheet was used as a beam-shutter.

As a first step, the shielding within the bunker was modified to reduce the intensity of the radiation originating from the horizontal channel of the reactor. The beam-stop of the unused straight channel was originally made of a polyethylene block covered with cadmium sheets (Figure 3.5). After removing the shielding from the top, a new beam-stop was installed. It consists of four Lithoflex (item 1 in the above list) layers to eliminate the slow component of the beam. The epithermal component is attenuated using 6 layers of borated polyethylene (item 3). The 478-keV gammas, born in this shielding, due to the capture of thermalized neutrons, are then absorbed in lead bricks (item 7) with a thickness of at least 10 cm on all sides and 5 cm on the top. The gap between the end window of the in-pile guide and the beginning of the out-of-pile guide was surrounded by 5-cm thick borated polyethylene (item 3). Figure 5.1 presents the modifications discussed above [92].

Figure 5.1: Internal bunker shielding modifications.

The whole front surface of the vacuum box and cold-head components of the cold source system was also covered with one layer of borated polyethylene sheet (item 3) to attenuate the scattered neutrons (Figure 5.2). Then the top shielding of the bunker was rebuilt similar to its original form from the following layers: a 14-cm thick wooden support fixed on the concrete wall, 10 cm of polyethylene, addition of 5.0 cm of borated polyethylene (item 3), and 5 layers of concrete bricks with a total thickness of 47.5 cm. On the exit wall of the bunker, the shielding is also built from concrete bricks with a minimum thickness of 76 cm. Around the exiting guide a polyethylene block (item 8) is placed into the bunker wall to reduce the dose from epithermal neutrons, which is followed horizontally by layers of 10-cm thick lead bricks and of 28.5-cm thick concrete bricks. The polyethylene block is also roofed by at least 1 m of concrete bricks and covered by no less than 1.5 m of concrete bricks on the sides. As a result of these modifications, the gamma-ray dose on the top of the bunker dropped by a factor of five, *i.e.* from 1.2 mRem/h (12μSv/h) to 0.2 mRem/h (2μSv/h) [92].

Figure 5.2: Borated polyethylene wall built in the bunker to attenuate scattered neutrons.

The next step was the reconstruction of the shielding of the PGAA facility itself. The experimental area is surrounded by 38-cm thick by 1.9-m high concrete walls, while the bunker provides shielding on the reactor side. The major sources of radiation inside the facility were presumed to be the beam shutter, the neutron guides (especially the focusing element), the sample environment (sample holders and the air), and the construction materials in the vicinity of the detector. They were shielded as described below [92].

The beam shutter, previously unshielded, was completely covered by a concrete wall with a minimum thickness of 38 cm in the direction of the beam. A plug of lead bricks was built around the guide with a minimum thickness of 20 cm to attenuate gamma radiation. The concrete walls, accommodating the shutter, were covered by 2.5 mm of borated polyethylene (item 3) and about 20 cm of lead. This first modification alone reduced the total count rate of the beam background in the gamma spectrum at full reactor power by more than a factor of 3. A switch has also been connected to the beam shutter to indicate its fully closed or open status. These modifications are shown in Figure 5.3 [92].

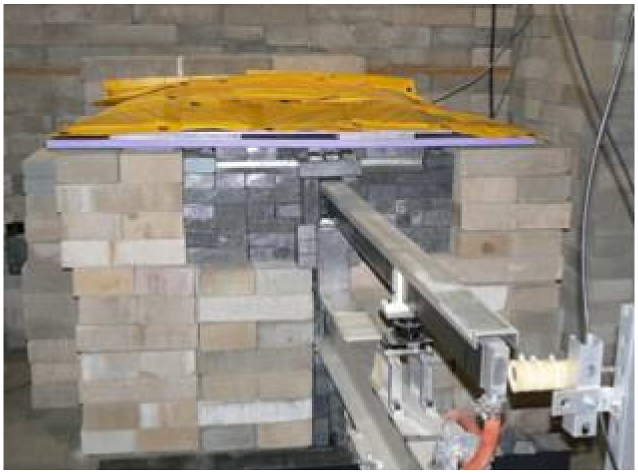

Figure 5.3: Shielding around the beam shutter and neutron guide adjacent to the bunker.

Next, the neutron guides were covered by granulated boron-loaded polyethylene sealed in polyethylene bags (item 4). The whole guide system was then covered with a concrete-brick tunnel (item 6) with a thickness of 39.5 cm on the sides and 19 cm on the top as shown in Figure 5.4. A neutron collimator, made of one layer of Lithoflex sheet (item 1), was fixed at the end of the curved neutron guide. The focusing neutron guide was covered by 5 cm of borated polyethylene sheets (item 3) to attenuate the out-scattered, low-energy neutrons and any remaining epithermal neutron radiation from the direction of the reactor channel (Figure 5.5). This section of the guide was also completely covered by a concrete wall with thicknesses of 39.5 cm on the sides, 19 cm on the top, and 19 cm in the direction of the sample (Figure 5.6). Only a small hole was left open at the end of the tunnel to accommodate a 15-cm long neutron collimator with a 5.0×1.5 cm^2 beam channel (Figure 5.7). The collimator is made of borated polyethylene (item 3) sandwiched between two sheets of 2.5-mm thick Lithoflex (item 1), and it is surrounded by lead bricks on all sides [92].

Figure 5.4: Concrete-brick tunnel constructed around the whole neutron guide system.

Figure 5.5: Borated polyethylene shielding surrounding the focusing guide.

Figure 5.6: Neutron collimator located in the opening at the end of the concrete tunnel.

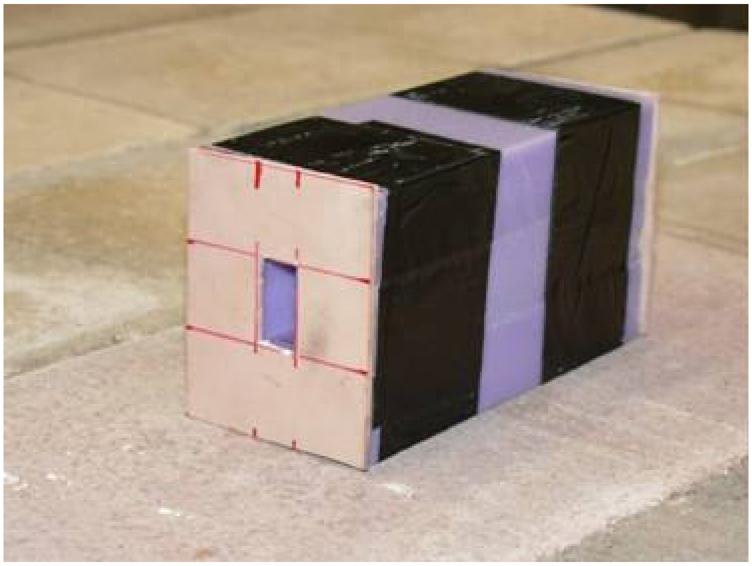

Figure 5.7: Neutron collimator made of borated polyethylene sandwiched between two sheets of Lithoflex.

The sample area was completely lined with Lithoflex (item 1). It consists of a Lithoflex tube after the neutron collimator, a 14.5 × 14.5 cm^2 Lithoflex-covered aluminum base plate (fixed on an aluminum support), a removable house constructed of four 14.5 × 17.5 × 0.25 cm^3 Lithoflex walls that sit on the base plate, and a Lithoflex end-tube with three 2.5-mm thick layers of Lithoflex serving as a beam-stop (Figure 5.8). The sample chamber is opened from the top to change samples. The sample holders, which can be exchanged for different types of samples, are mounted to the Lithoflex-covered aluminum base plate (Figure 5.9). The sample house has a removable 14.5 × 14.5 × 0.25 cm^3 Lithoflex roof and two properly aligned openings parallel to the beam (Figure 5.10). The whole structure is completely surrounded by lead with a minimum thickness of 10 cm. Thus the detector cannot "see" any construction material outside the sample chamber (Figure 5.11) [92].

Figure 5.8: Lithoflex-lined sample chamber (Lithoflex roof not shown).

Figure 5.9: Teflon® sample holder mounted on Lithoflex-covered aluminum base plate.

Figure 5.10: Lithoflex-lined sample chamber with Lithoflex roof.

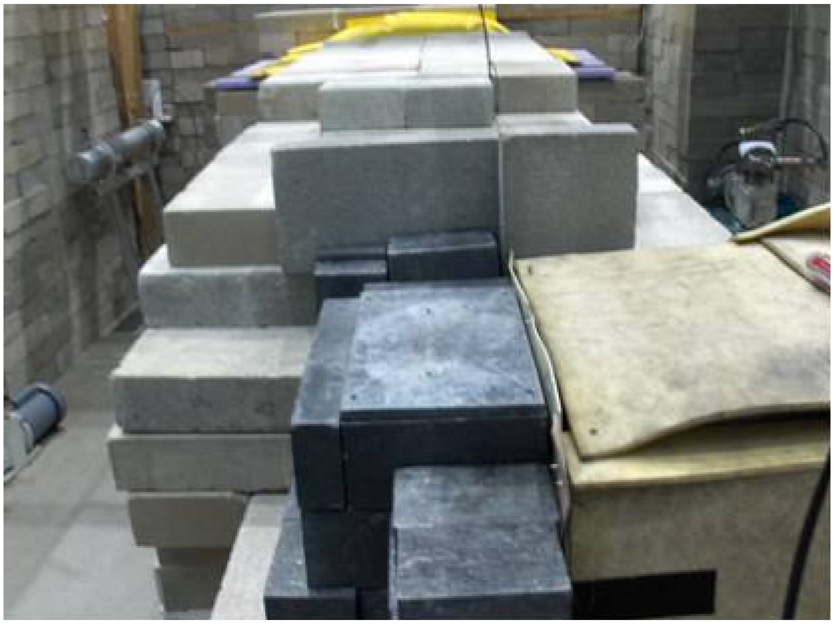

Figure 5.11: Sample chamber surrounded by lead.

The side and the neck of the HPGe detector are covered by lithium carbonate powder sealed in FEP foil (item 2) with a thickness of approximately 1 cm to reduce the activation of detector components. In the original configuration, a brick base supported the lead shielding surrounding the detector. In addition to this, an aluminum table was constructed above the Dewar flask. This table supports the lead shielding behind the detector to reduce significant background components coming from behind the HPGe (Figure 5.12). The entire detector assembly above the Dewar flask is thus shielded with at least 10-cm thick lead against gamma radiation. The lead housing is covered by Lithoflex in the front and Boroflex (item 5) on every other side (Figure 5.13). There are two extra sheets of Lithoflex shielding between the HPGe detector and the sample position to minimize activation of the detector components by sample-scattered neutrons [92].

Figure 5.12: Lead shielding supported by an aluminum table directly behind the HPGe.

Figure 5.13: Complete HPGe shielding setup.

The sample area within the Lithoflex house can be lined with a 13 × 12 × 0.0025 in^3 Teflon® bag (Welch Fluorocarbon, Inc.) and purged with helium to reduce the nitrogen and hydrogen background components found in air. The Teflon® bag is positioned and held in place by a thin aluminum frame that slides onto four end-threaded, vertically-set aluminum poles, which have a diameter of 5 mm and are set at each corner of the aluminum base plate. Four threaded aluminum knobs are used to clamp down the frame at the four corners (Figure 5.14). The Lithoflex house then surrounds the entire setup (Figure 5.15) [92].

Figure 5.16 illustrates the layout of the facility and the arrangement of the shielding materials for both the: (a) original and (b) redesigned PGAA facility, respectively. Figure 5.17 shows actual images of the PGAA facility: (a) before and (b) after reconstruction, respectively. Due to the shielding reconstruction, the different background components have been reduced by about an order of magnitude [92].

Figure 5.14: Helium purged Teflon® bag at the sample position.

Figure 5.15: Helium purged Teflon® bag surrounded by Lithoflex house (Lithoflex roof not shown).

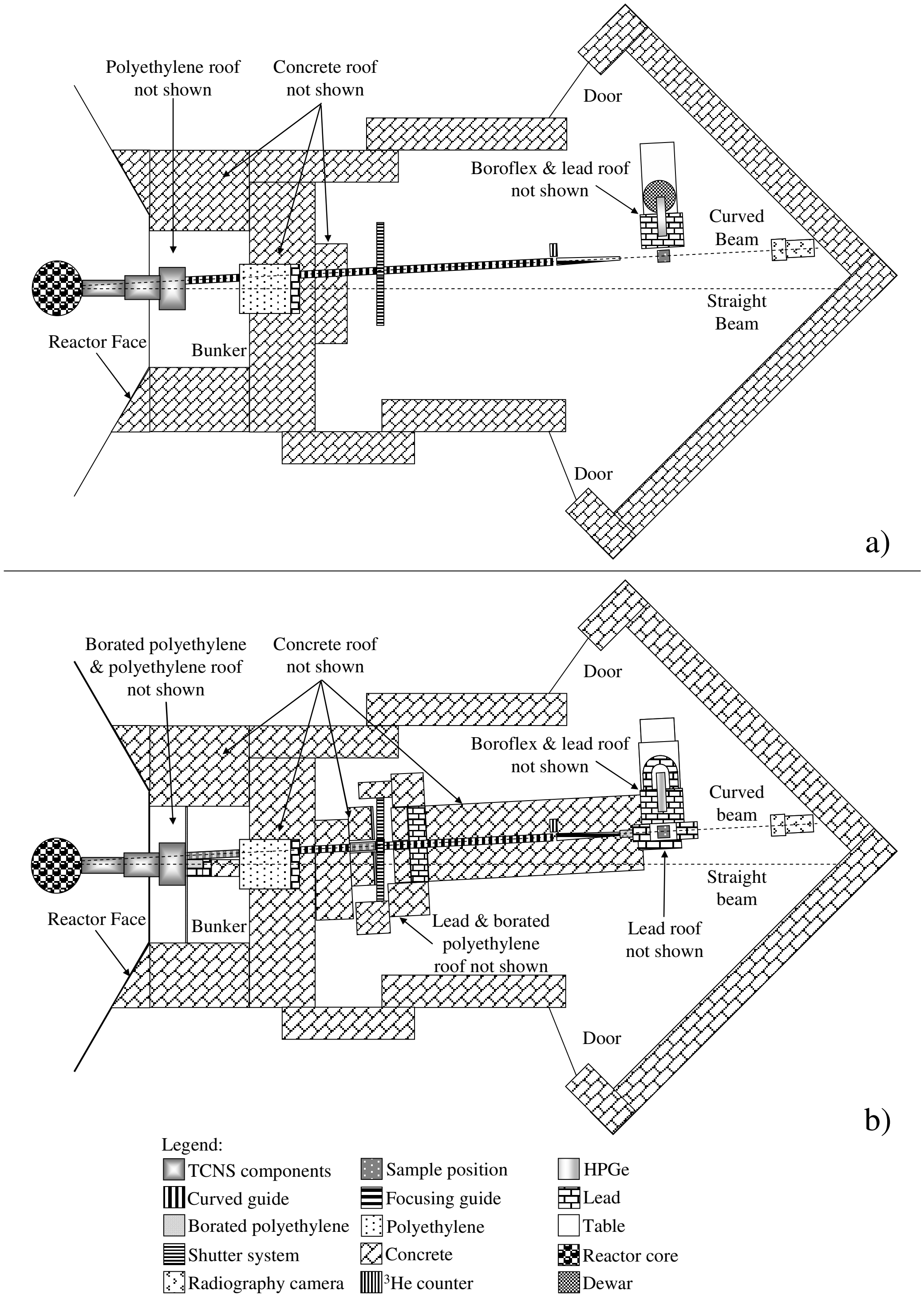

Figure 5.16: UT-PGAA facility: (a) before and (b) after reconstruction (Lithoflex house and Li_2CO_3 powder surrounding HPGe detector not shown).

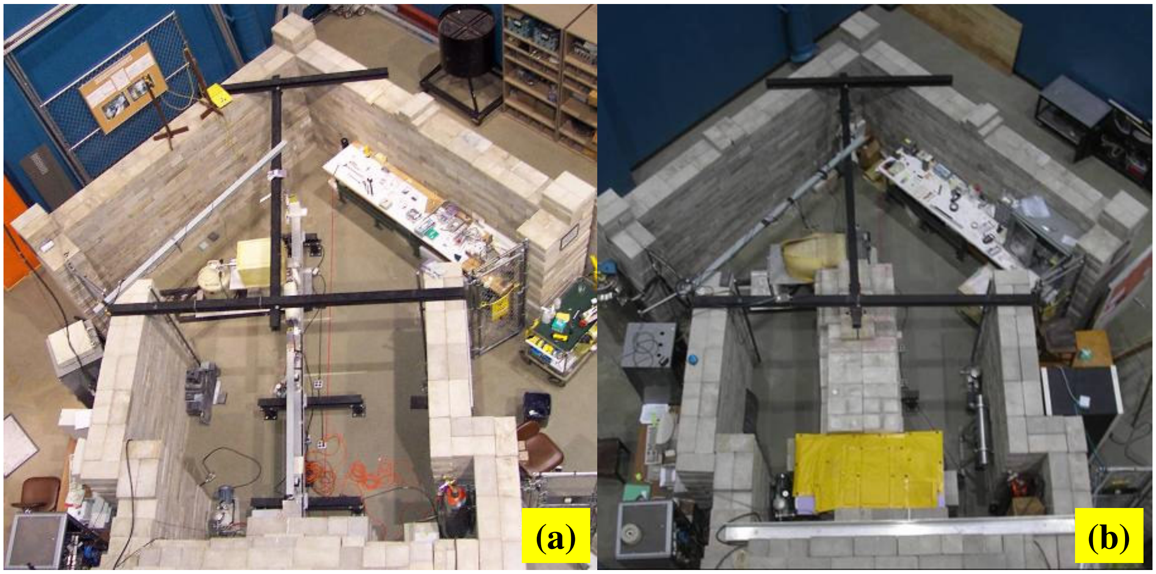

Figure 5.17: UT-PGAA facility: (a) before and (b) after reconstruction.

5.2 PGAA Instrument Calibration

The full width at half maximum (FWHM) peak resolution was determined with a low activity ^{60}Co source counted over a period of 16 hours. The FWHM value of 2.49 ± 0.06 keV at the ^{60}Co 1332 keV peak was calculated using a built-in FWHM module in the gamma spectrum evaluation code Hypermet-PC [104]. The counting efficiency of the system was determined with the method described in [105]. A calibrated ^{152}Eu source, a melamine sample as a ^{14}N (n,γ) source and an ammonium chloride sample as a ^{35}Cl (n,γ) source were counted. The peak areas were determined using Hypermet-PC. A 6th order polynomial was fitted on a log-log scale to count rates of the sources, again using the Hypermet-PC software [106]. The fitted function and the measured data are plotted in Figure 5.18. The lowest-energy section of the curve, which is not confirmed by several calibration points, is not used in the routine analysis, while the mid part (approximately

200–8000 keV) the curve is well defined. Its low value is due to the absorption of the gamma radiation in the dead layer of the p-type detector [92].

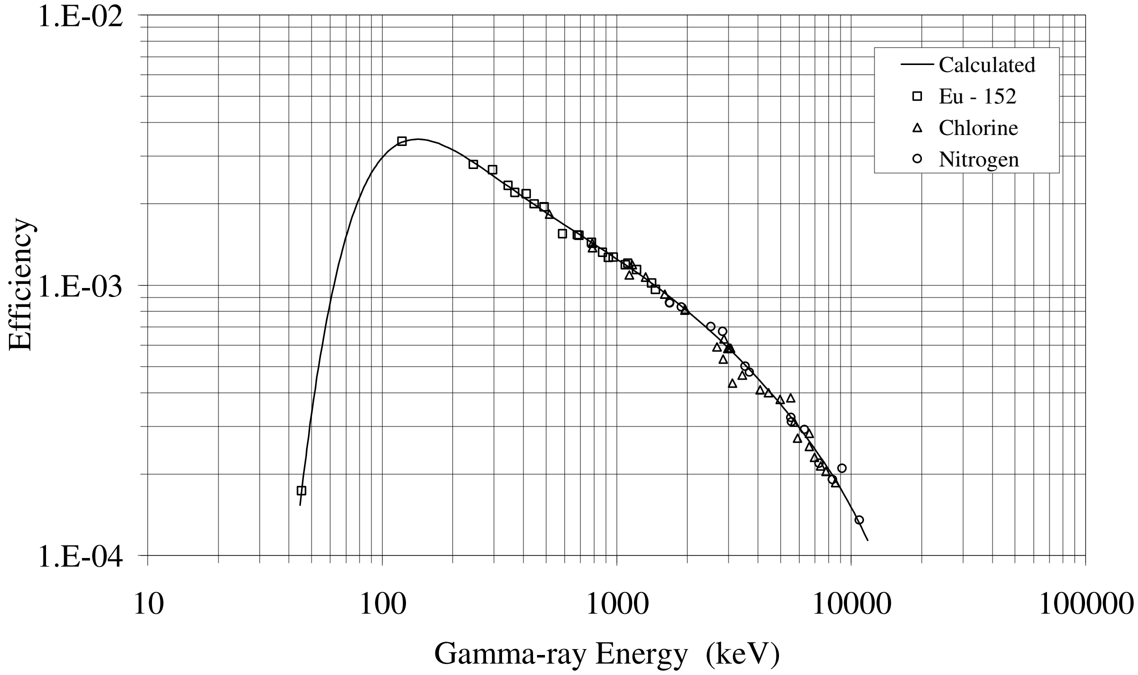

Figure 5.18: The counting efficiency of the UT-PGAA system.

The nonlinearity of the counting system was also determined using the same software, as described in [107]. The well-known energies of the ^{152}Eu decay gamma lines and ^{36}Cl prompt gamma lines [37, 108] were used to determine the discrepancies from the ideal linear energy calibration. High-energy prompt gamma lines of nitrogen were also added to improve the reliability of the nonlinearity function in the high-energy region where the number of calibration points is lower. A 6th order polynomial was fitted to these data in a similar fashion to the above-mentioned procedure. Figure 5.19 shows the measured and fitted nonlinearity data [92].

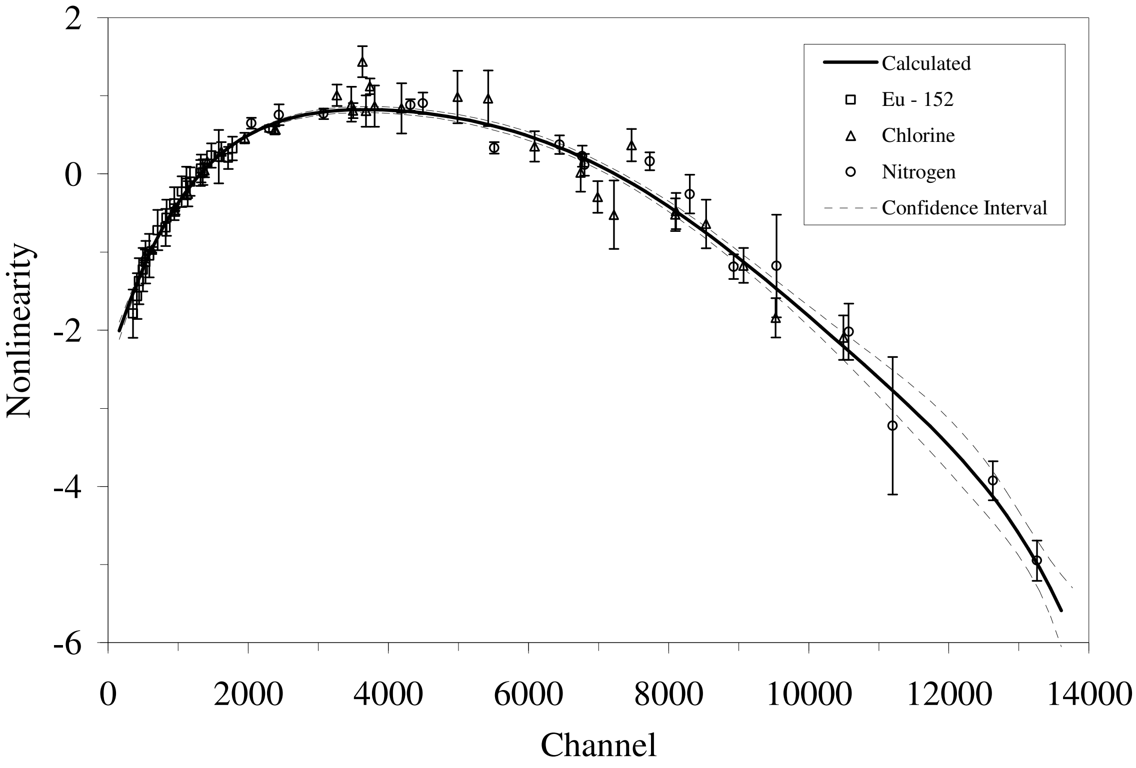

Figure 5.19: Nonlinearity function of peak positions as determined for the UT-PGAA system.

5.3 PGAA System Parameters Characterization

5.3.1 Neutron Flux

The thermal equivalent neutron flux was determined at the sample position using gold-foil activation at near full power of the reactor (950 kW). From the spectroscopic data of gold [37], the count rate of the 411-keV decay peak, and the counting efficiency at this energy, the thermal flux was calculated to be 5.32×10^{6} cm^{-2} s^{-1}. This value replaces the previously reported estimation [92].

The epithermal flux was determined using a gold foil packed in 0.5-mm thick cadmium foil. The thermal-to-epithermal ratio was found to be $8.1\times10^{4} \pm 10$ % [92].

The time dependent variation in neutron fluence was also observed and characterized in order to compare its behavior to the results previously reported for the PGAA facility before undergoing reconstruction [109]. The prior study hypothesized that fission product buildup, changes in temperature, and changes in control rod position were some of the parameters expected to contribute to the variation in neutron fluence at the sample location [109]. Understanding the fluence behavior at the sample position is important for accurate quantitative measurements especially when employing the relative standardization method (detailed in Section 4.2).

Similar to the previously performed investigation, the neutron fluence was qualitatively followed using the proportional ^{3}He counter positioned perpendicular to the neutron guide in the gap between the curved guide and the focusing element (Figure 3.8). The ^{3}He detector measures neutron leakage that is proportional to fluence in the guide. Several fluence measurements were recorded as a function of time on various days with the reactor operating at 950 kW. The measurements were taken on a regular basis throughout the day as count rates averaged over relatively short time intervals of about 1 h.

Experiments were also run with a sucrose sample located at the sample position in order to survey the influence that neutron backscatter due to high concentrations of hydrogen might have on the fluence values measured by the ^{3}He counter. The sucrose sample was placed at the sample position during the each of the last two measurements performed on the dates of 06/27/06 and 03/23/07. The ^{3}He counter is located about 1 m from the sample position.

Data obtained a few months preceding the facility reconstruction is compared to data obtained after the reconstruction. The focusing guide was not installed during the fluence measurement experiments performed prior to the facility redesign. Figure 5.20

presents the results for the neutron fluence data measured before and after the PGAA facility underwent facility redesign and reconstruction.

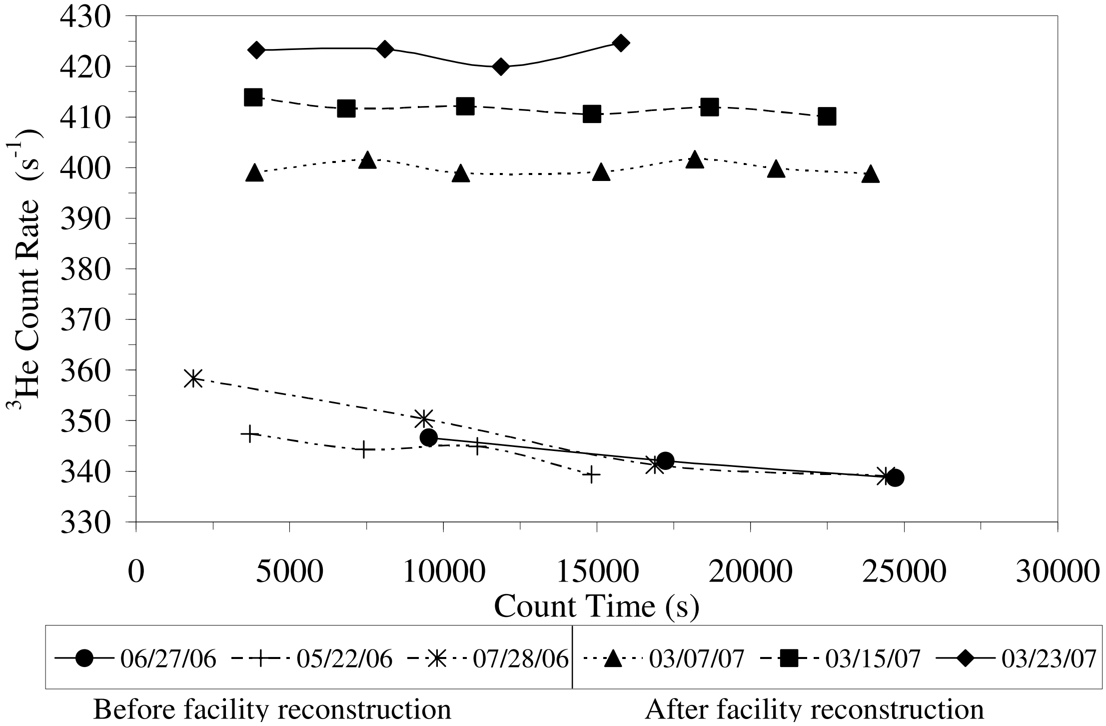

Figure 5.20: Neutron fluence rate variation as measured with the ^{3}He counter for the UT-PGAA facility before and after undergoing reconstruction.

Several differences are noted from the observed data. The most notable feature is that prior to reconstruction, decreases of between 2.3 and 5.4 % in neutron fluence were measured over the course of entire days. This depression in the fluence is similar to the 3.42 – 5.10 % deviation observed in the previous study while operating at a reactor power of 950 kW [109]. This type of variation has been eliminated due to the addition of the new facility shielding as the fluence depression is no longer observed in the post reconstruction measurements. The neutron fluence variation in a given day is not more than 1.00 % and therefore, can be assumed to be constant for the purposes of PGAA measurements as it relates to neutron fluence.

However, while the neutron fluence remains relatively constant over the course of a given day due to the facility modifications, the fluence values still vary significantly from day to day. In both cases (*i.e.* before and after reconstruction) the data indicates that the initial neutron fluence on any given day may vary from 3 to 5 %. This disparity is consistent with what was initially reported [109]. This variation is expected to come from the reactor operational history through the week. The buildup of ^{135}Xe in the reactor core is thought to be the primary cause of the fluence reduction. It should be noted that, in general, higher fluence rates were detected for the experiments conducted after the facility's reconstruction due to the installation of the new focusing guide as neutrons exiting the curved guide are now scattering off of the focusing element's entranceway materials.

Further, as mentioned above, to show the possible influence that neutron backscatter may have on the fluence variation a sucrose sample was located at the sample position during the last two measurements taken on the dates of 06/27/06 and 03/23/07. Relatively high levels of backscatter would be expected to increase the fluence as measured by the ^{3}He counter. From Figure 5.20, it is clear that no significant changes are observed on either day due to neutron backscatter.

These experiments suggest that the neutron leakage rates measured with the ^{3}He counter are adequate as a qualitative comparison to neutron fluence rates and can be used for normalizing the count rates between different irradiations as systematic and statistical errors are of great concern for PGAA analysis.

5.3.2 Neutron Beam Profile

The beam profile at the sample position was determined by a neutron radiography system using a TH 49424 HX tube manufactured by Thales Electron Devices (formerly called Thomson Tubes Electroniques) with a thin, 21.5-cm diameter gadolinium input screen and a vidicon camera [110]. The images are acquired by a National Instruments PCI-1409 8-bit black and white frame grabber card. The camera signal data is controlled and deconvoluted by a program written in LabVIEW™ using National Instrument IMAQ software. The radiography system is able to take and average a specified number of pictures in succession to improve counting statistics and provide better resolution [111]. Figure 5.21 shows the plot of the beam intensity along the cross-section of the beam at the sample position as measured with the neutron camera at a reactor power of 100 kW to avoid saturation of the camera. A MatLab program was written by a graduate student in the Nuclear and Radiation Engineering program (Mr. Richard Harrison) to normalize the pixels to width and height dimensions. A rectangular piece of cadmium, giving a strong shade in the camera, was used to determine the positions relative to the sample holder. As can be seen, horizontal and vertical stripes appear in the flux profile due to the reflections in the neutron guide [92].

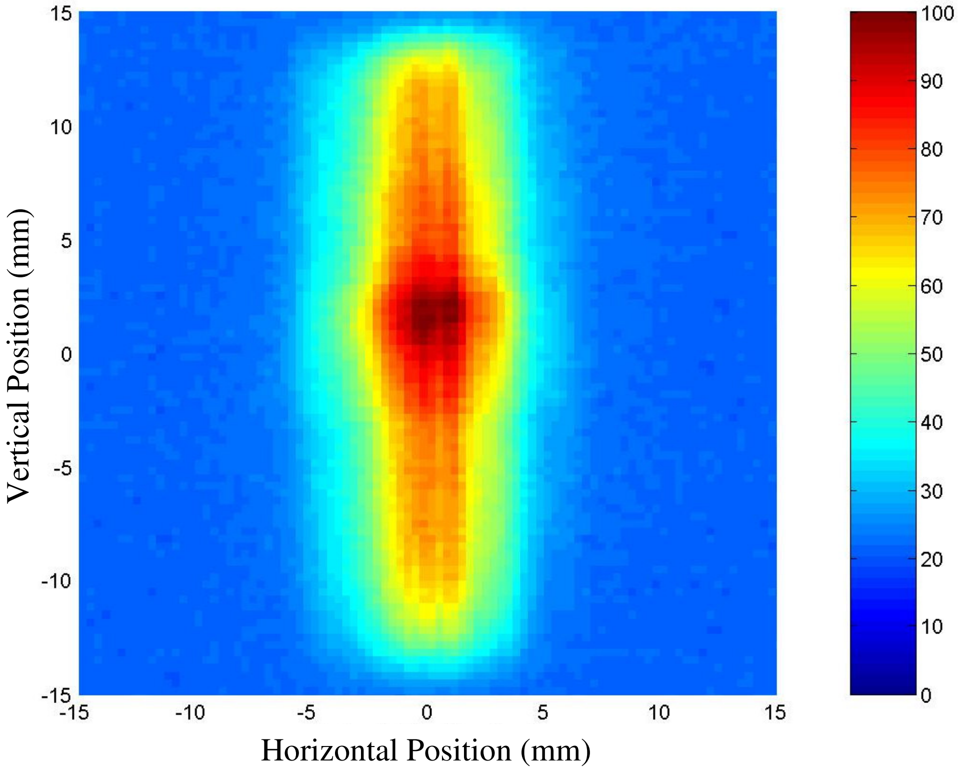

Figure 5.21: Two-dimensional neutron flux density radiograph at the sample position.

5.3.3 Neutron Temperature

The effective beam temperature was determined using the method described in [37, 112]. The real neutron flux was determined using a 0.5-cm^2 surface cadmium sheet with the “black sample” approximation [37]. From its ratio relative to the thermal equivalent flux, as determined using a thin iron foil of the same surface, the average wavelength of the beam was found to be 4.35 ± 0.35 Å, which corresponds to an effective temperature of 39 ± 6 K [92].

5.3.4 Background Characterization

After the redesign and reconstruction of the shielding, the background conditions improved significantly. The overall count rate in the beam-on, no-sample background spectrum, which is one of the most important characteristics, was reduced by a factor of 26, from 1300 cps to 50 cps. Other background characteristics improved by almost an order of magnitude, such as the fast and thermal neutron activation of the detector, as determined from the "germanium triangles" and germanium characteristic peaks [37], respectively. A series of characteristic background lines from elements frequently used in the analyses, like B, H, and Cd, were also reduced significantly. Figure 5.22 shows the PGAA background spectra before and after the facility reconstruction. Table 5.1 presents the different background components before and after the reconstruction [92].

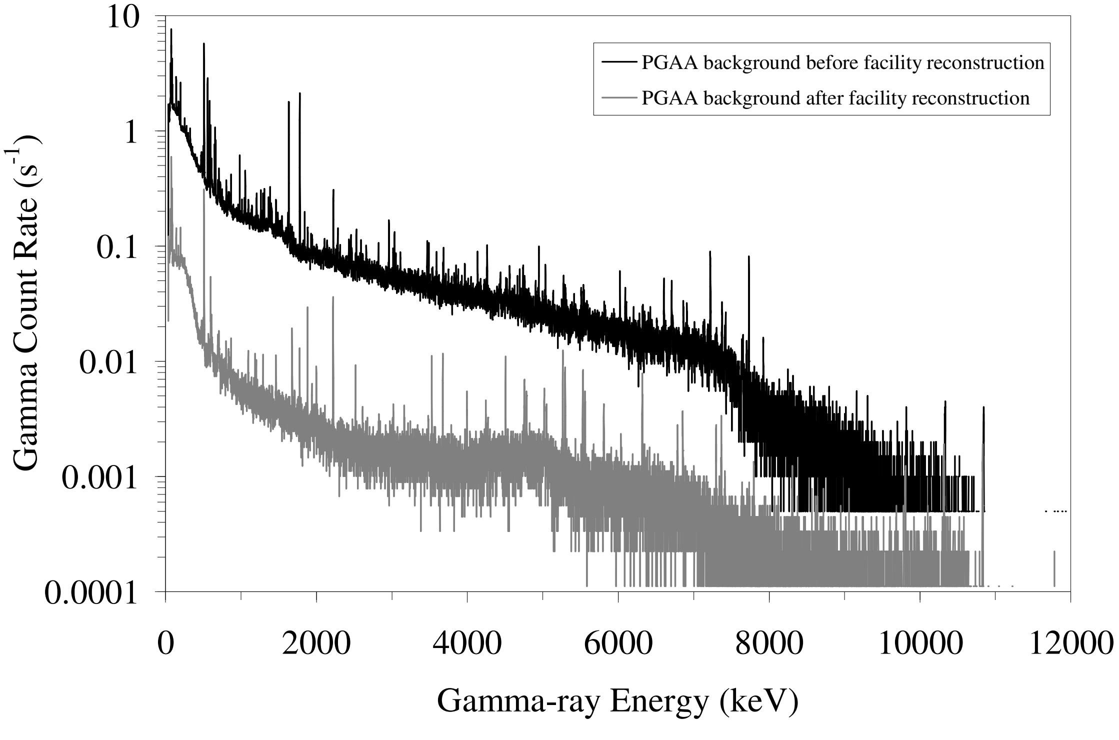

Figure 5.22: PGAA background spectra before and after facility reconstruction.

Table 5.1: Count rates of the beam background as measured with an empty sample chamber before and after the facility reconstruction.

Element	Energy (keV)	Count rate before reconstruction (s^{-1})	Count rate after reconstruction (s^{-1})	Factor of Improvement
Ge	141.1	3.558	0.174	20
Fe	352.8	0.251	0.014	18
B	477.6	2.892	0.065	44
Ge	499.9	0.703	0.025	28
Cd	558.3	6.647	n.d.	N/A
Ge	595.9	2.402	0.096	25
Ge triangle	592 – 627	3.937	0.236	17
Ge triangle	690 – 720	1.702	0.140	12
F	1633.5	5.908	n.d.	N/A
Al	1778.9	6.601	0.036	183
N	1884.8	0.198	0.101	2
Ca	1942.7	0.176	0.013	14
H	2223.2	0.825	0.128	6
Si	4933.9	0.089	n.d.	N/A
C	4945.3	0.306	n.d.	N/A
Pb	7367.8	0.122	0.018	7
N	10829.1	0.025	0.013	2

n.d. not detectable
N/A not applicable

There are several different sample environments that are routinely used for PGAA analysis, depending on the sample form and composition. The count rates were measured for the room (*i.e.* reactor-off), for the reactor (*i.e.* reactor-on, beam-off) and for the beam background in air (*i.e.* beam-on without any sample holder in the Lithoflex chamber). The beam background in helium was also observed without a sample holder, but with a Teflon® bag encompassing the sample position that is purged with helium to decrease neutron attenuation and background counts from the air. The helium gas used for this purpose has a purity of 99.9 %. There are also several different kinds of sample holders. A Teflon® base with Teflon® support spool and rigid vials is used for liquid samples and for samples where spatial repeatability is very important. Another common setup is an aluminum frame with Teflon® strings that can be used to suspend Teflon® sample pouches in the beam. This setup is used primarily for k_0-based analysis and for flat geometries. The sample holders are designed for quick interchangeability [92].

The characteristic peaks in the background spectra measured under different conditions were also examined carefully, *i.e.* the room background (reactor-off), the reactor background (beam-off, reactor-on at full power), and beam backgrounds in air and in helium atmosphere were compared. Table 5.2 shows the identified background peaks and Table 5.3 presents the equivalent masses of the activated construction materials [92].

Table 5.2: Count rates of background lines under different conditions.

E (keV)	Nuclide	Room	Reactor	Air	Helium
46.3	^{210}Pb [^{238}U series]	0.011			
53.3	^{234}U [^{238}U series]	0.082386	0.03		0.02
63.3	^{234}Th [^{238}U series]		0.045	0.12	
66.14		0.32	0.31		0.24
69.6				0.18	
72.82	Pb-X Kα2	0.059	0.016	0.76	0.54
74.77	Pb-X Kα1	0.106	0.3	1.4	0.97
84.85	Pb-X Kβ3	0.053	0.14	0.61	0.42
87	Pb-X Kβ2	0.019	0.09	0.21	0.13
92.123	^{234}Th [^{238}U series]	0.0175			
109.872				0.051	0.04
139.64	^{75m}Ge IT		0.16	0.17	0.17
166.9				0.061	
185.71	^{235}U [^{235}U series]	0.008	0.026		0.17
198.3		0.2	0.2	0.20	0.20
238.54	^{211}Pb [^{232}Th series]	0.013		0.018	0.02
252			0.032	0.032	0.03
416.7			0.02	0.015	
511	Annihilation	0.04	0.26	1.2	0.73
569.6	^{207}Bi		0.018		
583.348	^{208}Tl [^{232}Th series]	0.0049		0.0073	0.04
602.298	^{124}Sb [n-act.]	0.0065			
609.364	^{214}Bi [^{238}U-series]	0.011		0.02	0.02
867.7			0.02	0.03	0.03
911.09	^{228}Ac [^{232}Th series]	0.003			
1221.02	^{210}Tl [^{238}U series]	0.0034			
1238.02	^{214}Bi [^{238}U series]	0.0017			
1288.6		0.0011			
1460.64	^{40}K	0.0073			0.01
1463.181				0.02	0.02
1489.315			0.133		
1633.44	^{207}Bi		0.117		0.07
1691.172	^{124}Sb [n-act.]	0.0046			0.01
1764.29	^{214}Bi [^{238}U series]	0.004		0.01	0.01
2614.34	^{208}Tl [^{232}Th series]	0.0049		0.01	0.01

Table 5.3: UT-PGAA background elements.

Element	Equivalent mass in air (mg)	Equivalent mass in helium (mg)
H	0.19 ± 5 %	0.077 ± 10 %
Li	22 ± 17 %	n.d.
N	44 ± 2 %	16.5 ± 6 %
Al	1.7 ± 7 %	2.0 ± 11 %
Ca	0.68 ± 11 %	0.05 ± 20 %
Ge	0.63 ± 7 %	0.32 ± 9 %
Pb	47 ± 11 %	43 ± 13 %

n.d. not detectable

The variation of ^{41}Ar activity found in the room background, typical for this type of reactor, was also examined. ^{41}Ar decay gamma-rays arising from research reactor operations have been detected in other reactor laboratory environments. The site-specific spread of ^{41}Ar after irradiations has been measured *in situ* with a HPGe detector [113]. HPGe gamma spectroscopy has also been used to identify the ^{41}Ar peak arising from another TRIGA reactor [114].

After the identification of the decay line of ^{41}Ar at 1293 keV, its count rate as a function of time was determined. As it turned out, the highest activity of this background component typically appears several hours after the reactor shutdown, and only after several hours-long operations at full power, thus it does not significantly disturb the PGAA measurements. Figure 5.23 shows the count rate of the 1293-keV peak generated by ^{41}Ar and measured by the PGAA facility's HPGe detector [92].

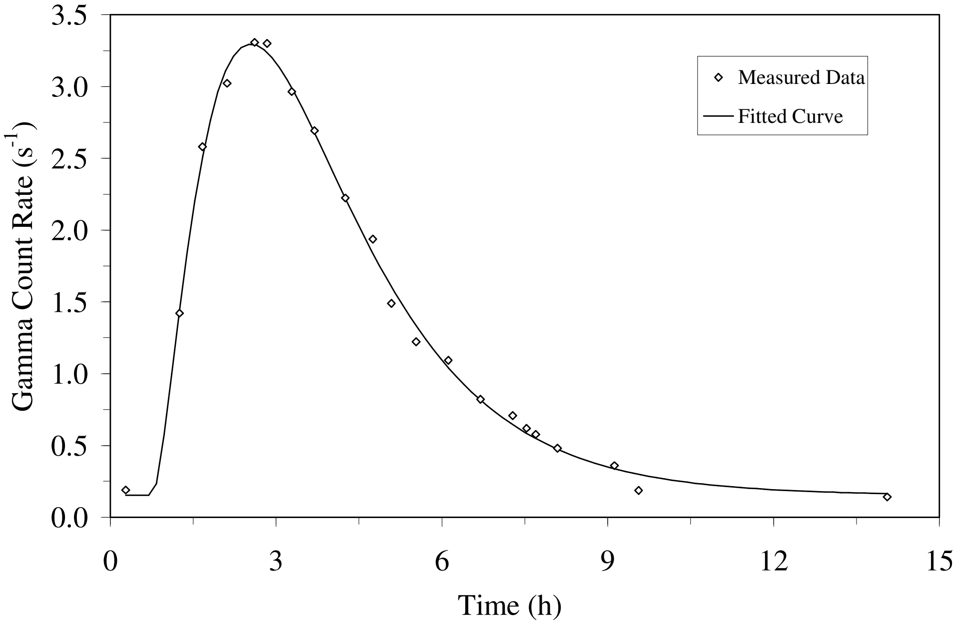

Figure 5.23: ^{41}Ar count rate as a function of time after reactor shutdown.

5.4 PGAA System Calibration for Hydrogen Analysis

To properly utilize the relative standardization method, as outlined in Section 4.2, the PGAA system had to first be calibrated with known standards in order to verify its effectiveness and readily identify prominent sources of error. The measurement system was calibrated in a manner similar to that presented in Aghara *et al.* (2005) and lab grade sucrose ($C_{12}H_{11}O_{22}$), with a hydrogen concentration of 64479 ± 1300 μg g^{-1}, was employed for this study as it was previously shown to be a suitable material for use as a hydrogen standard [102]. NIST SRM 1632C with a certified hydrogen content (51100 ± 1200 μg g^{-1}), laboratory grade $Ni(OH)_2$, $Ni(CH_3CO_2)_2$, and $LiOH{\cdot}H_2O$ were analyzed as "unknowns" in order to validate the detection capabilities of the PGAA facility for quality assurance/quality control purposes. The nickel contents in nickel hydroxide and nickel acetate presented an opportunity to emulate the matrices of the oxide cathodes as they contain similar transition metals such as Co and Mn. Similarly, lithium hydroxide presented a unique opportunity to qualify lithium's attenuation affects for the particular geometry used during these experiments since $LiOH \cdot H_2O$ has a lithium concentration of more than double what is expected even in the parent $LiMO_2$ compounds. Also, the relatively large hydrogen concentrations in each sample served to qualify the effects of neutron scattering.

Each calibration sample was dried in an air oven for 2 h at 100 °C and then stored in an evacuated desiccator until needed for further analysis in order to remove any water that may have been adsorbed onto the sample's surface. All samples were irradiated for long enough times to obtain sufficient counting statistics ($\geq$ 10,000 counts), typically from 0.5 to 1.0 h. System calibration was repeated as needed (*i.e.* after lengthy system downtime or system reconfiguration).

Table 5.4 presents the calibration results for hydrogen as measured for each of the "unknowns." Both the expected hydrogen content (certified value) and the experimentally measured hydrogen content for each sample are given. The percent differences between the expected and measured hydrogen values are also presented. As a comparison, the measured hydrogen values for SRM 1632C and $Ni(OH)_2$, respectively, are each presented twice to show the hydrogen detection improvement as a result of the PGAA facility reconstruction.

Before the PGAA facility reconstruction was undertaken, a good agreement between the theoretically expected and experimentally measured hydrogen contents with no more than 3.33 % difference validated the applicability of the PGAA facility to precisely and accurately measure hydrogen contents in a variety of samples. The attenuation effects of Li were also shown to be acceptable as the expected and measured hydrogen concentrations in the case of $LiOH \cdot H_2O$ were close in agreement.

After the PGAA facility reconstruction, the ability to precisely determine hydrogen was dramatically improved as the percent difference was decreased from 1.41 % to 0.62 % for SRM 1632C and from 2.11 % to 0.28 % for $Ni(OH)_2$, respectively. The small percent differences can most likely be attributed to PGAA background noise, counting statistics, slight variations in sample geometry, and trace amount of impurities in raw materials. Furthermore, hydrogen background levels can vary depending on the type of sample being analyzed as high hydrogen content in a given sample will lead to increased neutron scattering, which in turn can increase the probability of neutron interaction with hydrogenous materials located in the vicinity of the gamma-ray detector and thereby increase the hydrogen background count. Gamma-ray self-attenuation within the given samples may also have contributed to low levels of error [93]. The percent differences given in Table 5.4 were acceptable for the purposes of this study.

Table 5.4: PGAA hydrogen calibration results.

Sample	Expected H (μg g^{-1})	Measured H (μg g^{-1})	Difference (%)
Before PGAA facility reconstruction			
SRM 1632C	51100 ± 1200	51830 ± 440	1.41
$Ni(OH)_2$	21744 ± 2821	21285 ± 2888	2.11
$Ni(CH_3CO_2)_2$	34210 ± 3421	34851 ± 4215	1.87
$LiOH·H_2O$	72058 ± 1441	69656 ± 480	3.33
After PGAA facility reconstruction			
SRM 1632C	51100 ± 1200	50782 ± 667	0.62
Ni(OH)2	21744 ± 2821	21805 ± 314	0.28

*H Standard utilized to calculate measured H: $C_{12}H_{22}O_{11}$ 64479 ± 1300 μg g^{-1}

5.5 Hydrogen Limit of Detection

Given cobalt's spectral interference with hydrogen, it was important to quantify the detection limits for hydrogen as a function of cobalt content present in the respective sample matrices. In this regard, cobalt contents were varied in a number of lithium ion battery cathode samples in order to experimentally measure their respective limit of detection for hydrogen. The critical values and detection limits for the samples were calculated using Currie's method [115, 116] where the critical limit may be calculated as shown in Equation 5.1. For purposes of this investigation, the value for the abscissa of the standardized normal distribution was chosen to correspond to a 95 % confidence level and the measured gamma peak counts were assumed to have Poisson counting statistics (*i.e.* the mean equals the variance):

$$L_C = k\sqrt{2(\mu_{Bkg} + \mu_{Co} + \mu_C)} \tag{5.1}$$

where k is the abscissa of the standardized normal distribution, μ_{Bkg} is the measured hydrogen background peak area, μ_{Co} is the cobalt peak interference, and μ_C is the Compton continuum at the peak location composed of the background and cobalt continuum, respectively.

The detection limit can then be calculated as follows:

$$L_D = k^2 + 2L_C \tag{5.2}$$

L_D can be converted from units of counts to units of mass by way of Equation 5.3:

$$L_D(g) = \frac{L_D(counts) \cdot MW}{\varepsilon \cdot \gamma \cdot \phi \cdot \sigma \cdot N_A} \tag{5.3}$$

where L_D(g) is the detection limit in units of g, L_D(*counts*) is the detection limit in units of counts, *MW* is the molecular weight of the element of interest (g mol^{-1}), ε is gamma-ray energy dependent detector efficiency (counts/photons), γ is the gamma-ray yield (photons/capture), ϕ is the neutron fluence over the counting period (cm^{-2}), σ is the microscopic cross-section (cm^2), and N_A is Avogadro's number (mol^{-1}).

Similarly, the theoretical hydrogen detection limits were calculated based on measured cobalt sensitivities for both the 2221.61 keV gamma line and the Compton continuum, assuming the 2223.25 keV background peak and continuum reaction rates remained constant. Figure 5.24 provides a comparison of the measured and theoretical hydrogen detection limits, respectively.

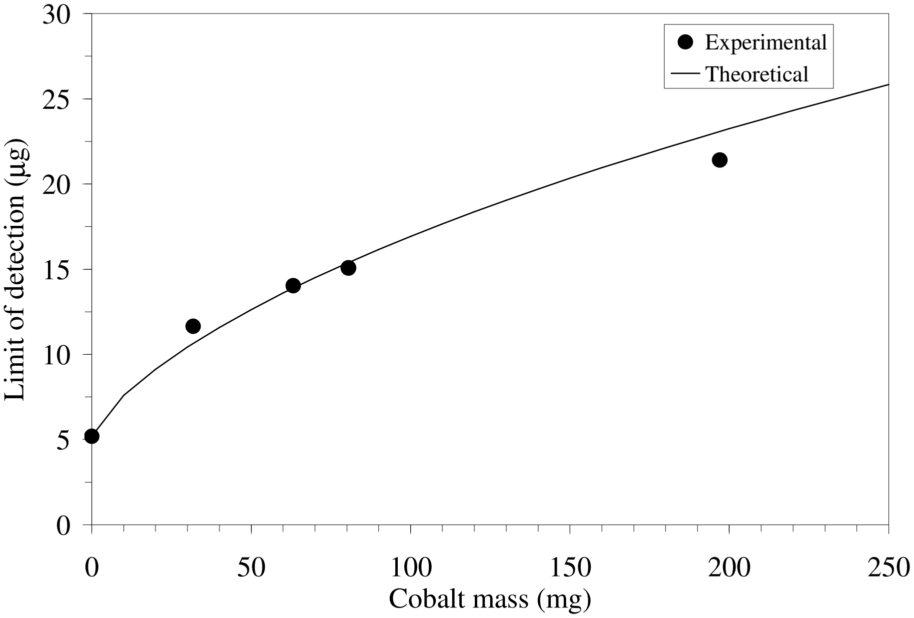

Figure 5.24: Comparison of the experimentally measured and theoretically calculated limits of detection for hydrogen as a function of cobalt mass.

The experimentally determined detection limits match well with the theoretically calculated detection limits. Assuming an extreme case where cobalt occupies one mole in the delithiated oxide lattice as in the case of CoO_2 (complete lithium extraction) and the sample mass is 350 mg, one would calculate a cobalt mass of 227 mg and a corresponding hydrogen detection limit of 22.7 μg for an analysis time of 2 h. This hydrogen limit of detection is quite acceptable for the purposes of this study as a hydrogen mass of around 2.16 mg is expected to be present in a 350 mg sample of fully delithiated $LiCoO_2$. This estimate is based on the charge neutrality principle assuming no oxygen is lost from the lattice and previous reports that have measured the oxidation state of cobalt to be around 3.44+ for the CoO_2 material [27, 29].

5.6 Summary of Work

The new physical arrangement of the UT-PGAA facility was designed and constructed with a special emphasis on the reduction of the background. As a result of the reconstructed shielding and the new sample chamber, all the background components present in the prompt gamma spectra were reduced by about an order of magnitude and sometimes even more. The thermal flux, the cadmium ratio and the effective temperature of the beam were also determined. The flux profile at the sample position was scanned by a neutron radiography camera system. The background components were identified and their count rates are given under different measuring conditions. Similarly the background elements appearing in the prompt gamma spectra were also identified and their equivalent masses were determined. All these efforts significantly improved the accuracy and the reliability of the analyses performed at the UT-PGAA facility especially for the precise determination of H as was demonstrated during the calibration of the PGAA system for hydrogen analysis.

Chapter 6: Experimental Results

6.1 Hydrogen Insertion into Lithium Ion Battery Cathodes during Chemical Delithiation

Oxide cathodes containing nickel and manganese, typically of the form $LiMO_2$ ($M = Ni_{1-y-z}Mn_yCo_z$), have been shown to produce higher capacities when compared to the commercially used $LiCoO_2$ [9, 10, 12, 17, 117-120]. The differences in capacity could be linked to chemical instabilities that are related to the position of the transition metal $M^{n+/(n+1)+}$:3d band relative to the top of the O^{2-}:2p band [8, 26-28, 30, 121, 122]. The chemical instabilities may be accommodated by either an ion exchange of Li^+ with H^+ or a forced loss of oxygen from the lattice. Prior investigations have focused on the indirect determination of proton insertion and/or oxygen loss from the $LiMO_2$ lattice after chemically extracting lithium. The previous studies have linked the deviation of the measured oxidation state from the theoretically expected value to the onset of chemical instability for a number of cathode systems [8, 26-28, 30, 121, 122].

A number of these same oxide cathode compounds have been analyzed by way of PGAA for the determination of hydrogen. The purpose of the investigation was to directly determine the hydrogen content (if any) present in the oxide cathode lattice after undergoing deep chemical delithiation and reveal the type of mechanism(s) occurring to relieve the associated chemical instabilities. The chemical delithiation was accomplished by stirring $LiMO_2$ parent compounds in a non-aqueous acetonitrile solution of NO_2BF_4 oxidizer under an argon environment [8, 26-28, 30, 121, 122]. Precautions were taken to keep the delithiated samples free from contamination such as ambient moisture that would skew data obtained from PGAA.

The samples analyzed during this study were: layered $Li_{1-x}CoO_2$, layered $Li_{1-x}Ni_{1/3}Mn_{1/3}Co_{1/3}O_2$, layered $Li_{1-x}Ni_{0.5}Mn_{0.5}O_2$, orthorhombic $LiMnO_2$ (o-$LiMnO_2$), spinel $Li_{1-x}Mn_2O_4$ (4 V cathode), spinel $Li_{1-x}Mn_{1.58}Ni_{0.42}O_4$ (5 V cathode), spinel $Li_{2-x}Co_2O_4$, and olivine $Li_{1-x}FePO_4$. The quantitative determination of hydrogen content in the delithiated oxide cathodes would establish the type of mechanism(s) (*i.e.* proton insertion and/or oxygen loss) occurring in given oxide cathode compounds and provide some insight into the factors that limit their practical capacities.

6.1.1 Experimental

$LiCoO_2$ was synthesized by a solid-state reaction where required amounts of Li_2CO_3 (Alfa Aeasar) and Co_3O_4 (GFS Chemicals) were ground together and then fired at 900 °C for 24 h in air. $LiNi_{1/3}Mn_{1/3}Co_{1/3}O_2$ and $LiNi_{0.5}Mn_{0.5}O_2$ were prepared by a co-precipitation method where required amounts of metal acetates ($Ni(CH_3CO_2)_2{\cdot}xH_2O$ (Alfa Aesar) and $Mn(CH_3CO_2)_2{\cdot}xH_2O$ (Acros Organics)) were dissolved in de-ionized water and then slowly dripped into a stirred solution of 0.1 M LiOH (Fischer Scientific) solution using a burette. The precipitate was then filtered and repeatedly washed with deionized water to remove residual lithium salts, if any, and oven dried in air at 100 °C for at least 24 h. Required amounts of $LiOH{\cdot}H_2O$ (Fischer Scientific) were then ground with the dried mixed metal hydroxide precipitate and subsequently fired at 900 °C for 24 h. $LiNiO_2$ was synthesized by co-precipitation method, mixed with a required amount of $LiOH{\cdot}H_2O$, and subsequently heated under O_2 atmosphere at 750 ^{o}C for 24 h. o-$LiMnO_2$ and $LiMn_2O_4$ were prepared by solid state reaction between Li_2CO_3 and Mn_2O_3 with subsequent firing at 1000 ^{o}C for 24 h under N_2 atmosphere for the former and at 800 ^{o}C for 48 h in air for the latter, respectively. $LiFePO_4$ was synthesized by firing required amounts of Li_2CO_3, $Fe(CH_3COO)_2$, and $NH_4H_2PO_4$ first at 320 ^{o}C for 3 h followed by grinding and refiring at 700 ^{o}C for 10 h all under N_2 atmosphere. Low temperature $LiCoO_2$, that has a lithiated spinel structure $Li_2Co_2O_4$, was synthesized by firing a stoichiometric amount of Li_2CO_3 and Co_3O_4 at 400 ^{o}C in air for 1 week [123-126]. It should be noted that the $LiNiO_2$, o-$LiMnO_2$, $LiMn_2O_4$, $LiFePO_4$, and $Li_2Co_2O_4$ samples were synthesized and provided to the author by two graduate students (Dr. Jeh Won Choi and Mr. Tiruvannamalai Arunkumar) in Dr. Manthiram's laboratory.

Controlled delithiation of the samples was accomplished by stirring the as-synthesized parent oxides for 2 days in a non-aqueous solution of NO_2BF_4 and acetonitrile under an argon atmosphere. The samples were then washed with fresh acetonitrile to remove any residual $LiBF_4$ and then vacuum dried at room temperature. In order to avoid moisture adsorption onto the surface of the samples they were carefully handled under argon atmosphere throughout the delithiation process. The delithiation of the $LiNiO_2$, o-$LiMnO_2$, $LiMn_2O_4$, $LiFePO_4$, and $Li_2Co_2O_4$ samples was carried out by Dr. Choi and Mr. Arunkumar.

Prior to this investigation, the PGAA facility at UT had shown to be well suited for the detection of hydrogen in delithiated oxide cathode materials treated with 2.5 N H_2SO_4 [102]. Since then, as detailed in Chapter 5, the UT-PGAA facility has been completely redesigned and reconstructed as part of an effort to substantially reduce background noise and improve detection limits. Hydrogen background noise levels have been substantially reduced by optimizing the PGAA facility's shielding [92]. The set of experiments discussed here were conducted prior to the facility's recent reconstruction.

In order to further establish the reliability and accuracy of PGAA in determining the hydrogen content in metal oxide materials, attention was first given to a few layered oxides that are known to contain protons and are free from Co since its 2221.61 keV photon may interfere with hydrogen's 2223.25 keV photon. Accordingly, presented here are the PGAA results of the layered oxide composition $LiNi_{0.5}Mn_{0.5}O_2$ before (parent) and after (daughter) treating with dilute H_2SO_4. The chemical extraction of lithium was performed by stirring $LiNi_{0.5}Mn_{0.5}O_2$ with 1.0 and 2.5 N aqueous H_2SO_4, respectively, for 2 days. The resulting solution was then filtered and dried in an air oven for $\geq$ 12 h. Treatment with aqueous acid is known not only to extract lithium chemically but also to incorporate protons into the lattice [29].

To complement the PGAA data, each sample was structurally and chemically analyzed by AAS to determine lithium content, iodometric titration for the measurement of the average oxidation state (M^{n+}), and XRD. Some samples were analyzed by TGA and mass spectrometry. These characterizations were carried out by Dr. Choi and Mr. Arunkumar for the $LiNiO_2$, o-$LiMnO_2$, $LiMn_2O_4$, $LiFePO_4$, and $Li_2Co_2O_4$ samples. The acid treated samples were also analyzed by Fourier Transform Infrared Spectroscopy (FTIR), a technique used for detecting O–H groups.

6.1.2 Aqueous Chemical Delithiation of $LiNi_{0.5}Mn_{0.5}O_2$

Table 6.1 gives the PGAA results of the parent and aqueous delithiated daughter $Li_{1-x}Ni_{0.5}Mn_{0.5}O_2$ samples that were analyzed as a proof of principle to demonstrate that PGAA can be used to precisely quantify the hydrogen contents in lithium ion battery cathode materials. The final compositions of the parent and delithiated daughter samples were obtained based on the charge neutrality principle where the AAS data for lithium content, PGAA data for hydrogen content, and average oxidation state of the transition metals were employed. As seen in Table 6.1, there was no significant amount of hydrogen above background detected in the parent compound. These results are comparable to those presented by Aghara *et al.* (2005) for analogous materials [102].

Table 6.1: Chemical analysis and PGAA data of $LiNi_{0.5}Mn_{0.5}O_2$ before (parent) and after (daughter) treating with 1.0 and 2.5 N H_2SO_4.

Sample	H content (± 0.01)	Li content (± 0.02)	M^{n+} (± 0.02)	Final Composition[a]
Parent	0.00	1.00	3.00	$LiNi_{0.5}Mn_{0.5}O_2$
1.0 N Daughter	0.17	0.42	3.41	$H_{0.17}Li_{0.42}Ni_{0.5}Mn_{0.5}O_2$
2.5 N Daughter	0.19	0.43	3.38	$H_{0.19}Li_{0.43}Ni_{0.5}Mn_{0.5}O_2$

[a] Obtained based on the Li content and oxidation state analysis assuming no oxygen loss.

Figure 6.1 presents the results obtained from the FTIR analysis of the parent and two of the daughter compounds, $H_{0.17}Li_{0.42}Ni_{0.5}Mn_{0.5}O_2$ and $H_{0.19}Li_{0.43}Ni_{0.5}Mn_{0.5}O_2$, respectively. The data shows that the chemically delithiated daughter samples have an absorption band around 3,500 cm^{-1} that corresponds to the O-H stretch [29]; no such band is observed for the parent sample. The FTIR results are consistent with the PGAA analysis, confirming the incorporation of protons into $LiNi_{0.5}Mn_{0.5}O_2$ during the acid treatment process with H_2SO_4.

Several daughter $Li_{1-x}Ni_{0.5}Mn_{0.5}O_2$ compounds also underwent aqueous delithiation as a function of stirring time with 2.5 N H_2SO_4 in order to measure the relative levels of hydrogen insertion. Table 6.2 presents the data for the $Li_{1-x}Ni_{0.5}Mn_{0.5}O_2$ samples where, again, H content was measured by PGAA, Li content was determined by AAS, the average oxidation state was found by iodometric titration, and the final composition was determined by the charge neutrality principle.

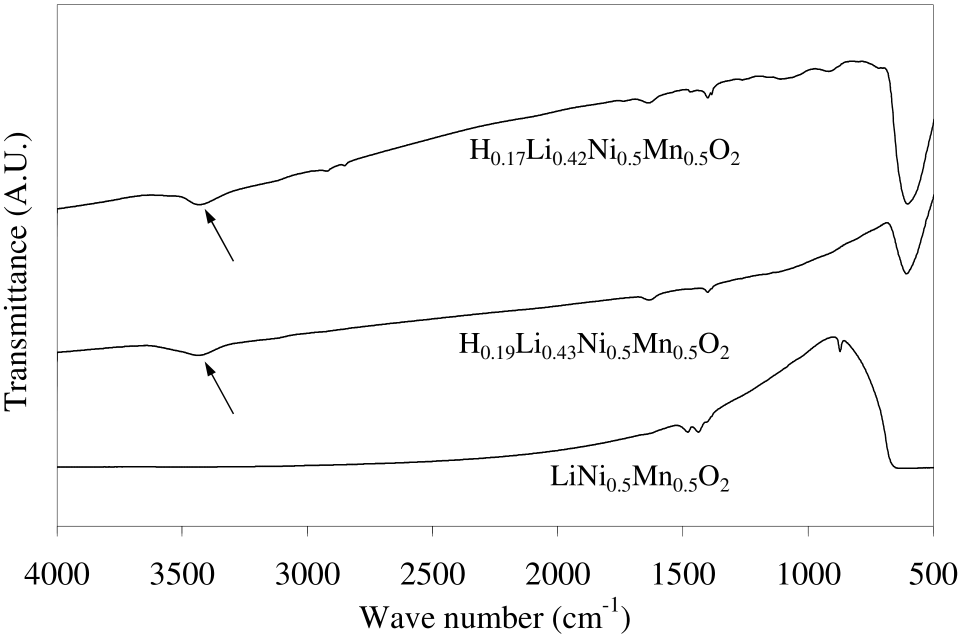

Figure 6.1: Comparison of the FTIR spectra for the parent $LiNi_{0.5}Mn_{0.5}O_2$, aqueous delithiated daughter $H_{0.19}Li_{0.42}Ni_{0.5}Mn_{0.5}O_2$, and aqueous delithiated daughter $H_{0.19}Li_{0.43}Ni_{0.5}Mn_{0.5}O_2$. The arrow indicates the position of the characteristic O-H group absorption band (~ 3500 cm^{-1}).

Table 6.2: Chemical analysis and PGAA data of aqueous delithiated $Li_{1-x}Ni_{0.5}Mn_{0.5}O_2$ compounds as a function of extraction time with 2.5 N H_2SO_4.

Extraction time (h)	H content (± 0.01)	Li content (± 0.02)	M^{n+} (± 0.02)	Final Composition[a]
6	0.14	0.46	3.40	$H_{0.14}Li_{0.46}Ni_{0.5}Mn_{0.5}O_2$
12	0.17	0.43	3.40	$H_{0.17}Li_{0.43}Ni_{0.5}Mn_{0.5}O_2$
48	0.23	0.35	3.41	$H_{0.24}Li_{0.42}Ni_{0.5}Mn_{0.5}O_2$
96	0.29	0.28	3.42	$H_{0.30}Li_{0.28}Ni_{0.5}Mn_{0.5}O_2$

[a] Obtained based on the Li content and oxidation state analysis assuming no oxygen loss.

From the data given in Table 6.2, it is apparent that the amount of lithium that is extracted from the $LiNi_{0.5}Mn_{0.5}O_2$ lattice is not significantly affected for chemical extraction times of $\leq$ 48 h in aqueous 2.5 N H_2SO_4. Similarly, the amount of H^+ ions exchanged with Li^+ ions does not significantly increase for delithiation times of $\leq$ 48 h. However, larger amounts of hydrogen are inserted into the $LiNi_{0.5}Mn_{0.5}O_2$ lattice for extraction times > 48 h. The difference in the measured average oxidation state remains relatively constant regardless of lithium extraction time which provides evidence that the ion exchange of H^+ with Li^+ is the predominate factor for controlling the extraction of lithium during aqueous chemical delithiation.

The sample that was stirred for 24 h is not presented in Table 6.2 as its measured hydrogen content did not match well with the expected value as calculated from the charge neutrality principle based on the lithium content and oxidation state analysis results. It is reasoned that there is significant error associated with this sample due to boron contamination that could have been introduced as an impurity during the filtering process. Since the filter material is composed of borosilicate glass, it is rationalized that significant amounts of borosilicate glass particles were inadvertently scraped off of the filter's surface while the dried sample powder was being removed. The addition of the borosilicate glass material adversely affects all of the characterization results and both the lithium content and oxidation state values are expected to be higher than what was measured. The presence of substantial amounts of boron beyond the accepted range, as discussed in Section 4.4, was confirmed by PGAA (Figure 6.2). The spectrum also reveals a suppressed nickel peak where the suppression is most likely due to low levels of neutron attenuation caused by the presence of boron.

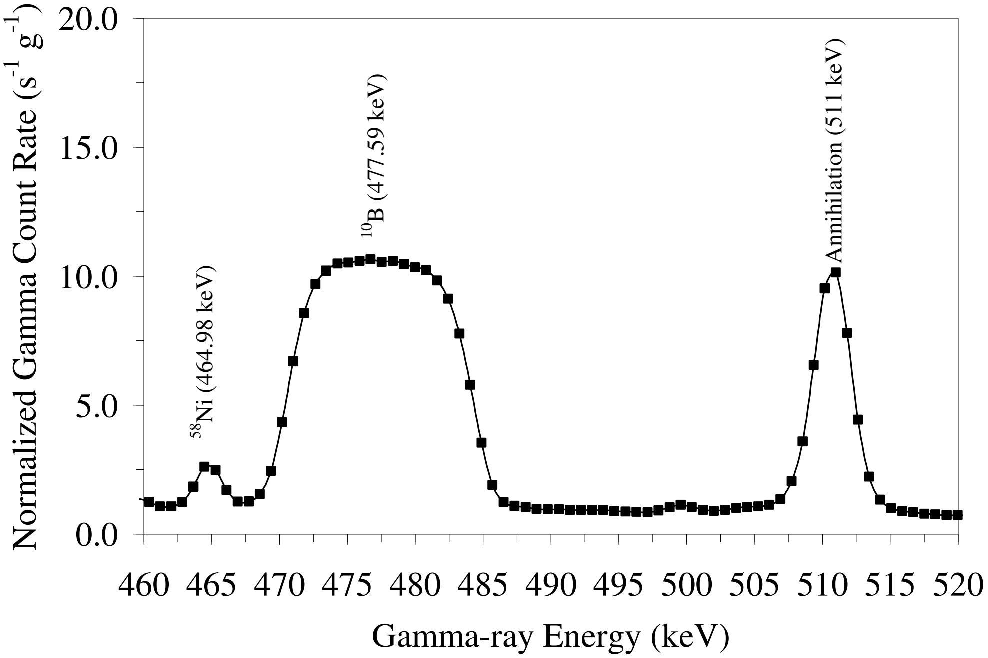

Figure 6.2: Normalized PGAA spectra for $H_{0.29}Li_{0.35}Ni_{0.5}Mn_{0.5}O_2$ revealing the ^{58}Ni 464.98 keV, ^{10}B 477.59 keV, and annihilation 511 keV gamma peaks.

In general, the results provided above prove that PGAA at UT is a viable technique for measuring trace concentrations of hydrogen in metal oxides of interest for lithium ion battery cathodes. Chemical delithiation with aqueous acid results in an incorporation of a significant amount of protons into the lattice of layered $LiNi_{0.5}Mn_{0.5}O_2$.

Presented below are the chemical and structural results obtained for the oxide cathode materials after extracting lithium in acetonitrile with NO_2BF_4 as an oxidizing agent. In contrast to the experiments with aqueous medium, those with non-aqueous medium are not anticipated to incorporate protons into the lattice. Such a study with PGAA can help to understand the factors limiting the practical capacities of lithium ion battery cathodes and to design new better performing cathodes.

6.1.3 Non-Aqueous Chemical Delithiation of Lithium Ion Battery Cathodes

In the case of electrochemical cells, as presented in Section 1.3, four possibilities exist for the electrochemical redox process occurring at deep charging of the $LiMO_2$ cathodes: (i) oxidation of M^{3+} to M^{4+} as one would normally anticipate, (ii) oxidation of O^{2-} ions leading to a loss of oxygen from the lattice, (iii) ion exchange of Li^+ by H^+ generated by an electrochemical oxidation of the electrolyte solvent, or (iv) the combination of two or all three of the above processes. These mechanisms also exist for the case of chemically delithiated oxide cathodes except that the H^+ ions could be generated from the acetonitrile rather than the electrolyte solvent as in the case of a practical lithium ion cell. The application of PGAA to this issue has resolved exactly which mechanism(s) is occurring for specific systems that have undergone chemical delithiation as presented in Table 6.3 where the compound of interest, its structure type, its hydrogen content as measured by PGAA, its lithium content determined by AAS, its average oxidation state measured by redox titration, its final composition as calculated by charge neutrality, and its chemical instability mechanism(s) are presented.

The commercially used cathode, layered $LiCoO_2$, was shown to undergo only hydrogen insertion during deep chemical delithiation while it was found that the spinel $LiMn_2O_4$ compound only undergoes oxidation of Mn. So in the case of $LiCoO_2$, possibility (iii) was shown to be true and in the case of $LiMn_2O_4$, possibility (i) was found to be true. Although, as evident from the data presented in Table 6.3, possibility (iv), a combination of hydrogen insertion and oxygen loss from the lattice, has also been proven to exist as in the case of spinel $Li_2Co_2O_4$ and the layered series $Li[Li_{0.17}Mn_{0.33}Co_{0.5-y}Ni_y]O_2$ ($0 \leq y \leq 0.5$) whose results are reserved for a more detailed discussion in Section 6.3. By way of this investigation, only possibility (ii), oxidation of O^{2-}, has not yet been proven to occur exclusively in chemically delithiated oxide cathodes. However, that may or may not be the case in electrochemically charged lithium ion cells.

Table 6.3: Chemical analysis and PGAA data of the chemically delithiated cathodes [33].

Compound	Structure	H content (± 0.02)	Li content (± 0.02)	M^{n+} (± 0.02)	Final Composition[b]	Mechanism(s)
$LiCoO_2$	Layered	0.37	0.05	3.56	$H_{0.39}Li_{0.05}CoO_2$	H^+ insertion
$LiNiO_2$[a]	Layered	0.03	0.09	3.92	$Li_{0.09}NiO_2$	N/A
$LiNi_{1/3}Mn_{1/3}Co_{1/3}O_2$	Layered	0.39	0.02	3.58	$H_{0.40}Li_{0.02}Ni_{1/3}Mn_{1/3}Co_{1/3}O_2$	H^+ insertion
$LiNi_{0.5}Mn_{0.5}O_2$	Layered	0.34	0.08	3.58	$H_{0.34}Li_{0.08}Ni_{0.5}Mn_{0.5}O_2$	H^+ insertion
o-$LiMnO_2$[a]	Orthorhombic	0.03	0.25	3.70	$H_{0.05}Li_{0.25}MnO_2$	N/A
$LiMn_2O_4$[a]	Spinel	0.03	0.06	3.97	$Li_{0.06}Mn_2O_4$	N/A
$LiMn_{1.58}Ni_{0.42}O_4$[a]	Spinel	0.00	0.08	3.96	$Li_{0.08}Mn_{1.58}Ni_{0.42}O_4$	N/A
$Li_2Co_2O_4$[a, c]	Spinel	0.18	0.60	3.38	$H_{0.24}Li_{0.60}Co_2O_{3.80}$[d]	H^+ insertion & O^{2-} loss
$LiFePO_4$[a]	Olivine	0.00	0.00	3.00	$FePO_4$	N/A

[a] Synthesis and non-PGAA analysis of these compounds was performed by Dr. Choi and Mr. Arunkumar.
[b] Obtained based on the Li content and oxidation state analysis assuming no oxygen loss occurs except for $Li_{2-x}Co_2O_4$.
[c] Low temperature $LiCoO_2$ that has a lithiated spinel ($Li_2Co_2O_4$) structure[123-126].
[d] Obtained based on the TGA data analysis.

The data reveal the insertion of a significant amount of hydrogen due to an ion exchange of Li^+ by H^+ at deep lithium extraction in the case of layered $Li_{1-x}CoO_2$, $Li_{1-x}Ni_{1/3}Mn_{1/3}Co_{1/3}O_2$, and $Li_{1-x}Ni_{0.5}Mn_{0.5}O_2$. However, little or no proton is inserted in cases like layered $Li_{1-x}NiO_2$, o-$Li_{1-x}MnO_2$, spinel $Li_{1-x}Mn_2O_4$ (4 V cathode), spinel $Li_{1-x}Mn_{1.58}Ni_{0.42}O_4$ (5 V cathode), and olivine $Li_{1-x}FePO_4$. The difference may be related to the good chemical stability of the $Mn^{3+/4+}$ and $Fe^{2+/3+}$ couples and the chemical instability of the $Co^{3+/4+}$ couple at deep lithium extraction. When comparing layered $LiNi_{0.5}Mn_{0.5}O_2$ to layered $LiNiO_2$ and spinel $LiMn_{1.58}Ni_{0.42}O_2$, only the layered $LiNi_{0.5}Mn_{0.5}O_2$ undergoes significant proton insertion even though they each have the $Ni^{3+/4+}$ couple in common. This occurrence can most likely be attributed to the position of the $Ni^{3+/4+}$:3d band relative to the top of the O^{2-}:2p band depending upon the composition, structure, and atomic arrangement in the layered lattice [8, 33, 122, 127]. Figure 6.3 compares the qualitative energy band diagrams of $Li_{1-x}CoO_2$ and $Li_{1-x}NiO_2$, respectively, as proposed by Chebiam *et al.* (2001) [8]. The grey shading represents a qualitative population of the bands by the electrons.

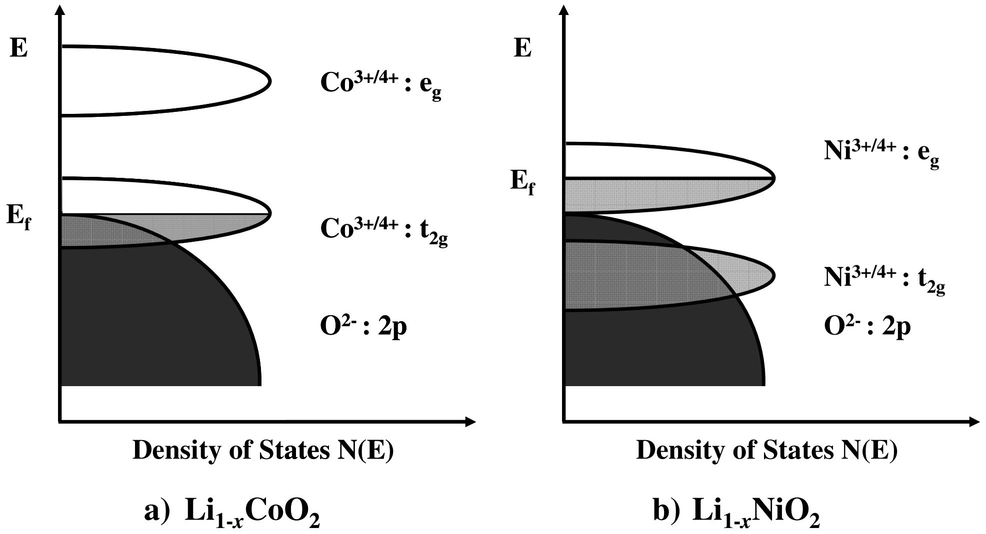

a) $Li_{1-x}CoO_2$ **b) $Li_{1-x}NiO_2$**

Figure 6.3: Qualitative energy band diagrams of: a) $Li_{1-x}CoO_2$ and b) $Li_{1-x}NiO_2$.

In the case of $LiCoO_2$, the t_{2g} band is initially completely filled and the e_g band is empty. When lithium is extracted from the lattice, Co^{3+} oxidizes to Co^{4+} thus leading to a removal of electrons from the t_{2g} band. However, due to the overlap of the t_{2g} band with the O^{2-}:2p band, the possibility exists for the oxidation of oxygen when lithium is extracted beyond $1-x < 0.5$ as electrons are more deeply removed from the t_{2g} band [8]. A chemical instability arises when O^{2-} undergoes oxidation as oxygen can then be lost from the system. This type of oxygen loss could limit the practical capacity of lithium ion cells but in the case of the chemically delithiated $Li_{1-x}CoO_2$, hydrogen may be more readily available and can more easily accommodate the instability as compared to a forced removal of oxygen from the lattice.

In contrast, $LiNiO_2$, while undergoing lithium extraction and subsequent oxidation of Ni^{3+} to Ni^{4+}, only involves the removal of electrons from the e_g band that is above the top of the O^{2-}:2p band [8]. Since the e_g band is above the top of the O^{2-}:2p band, there is not much chemical instability and therefore no oxygen loss or, in the case of chemical delithiation, no hydrogen insertion occurs. Past studies have shown increasing levels of chemical instability in the layered $Li_{1-x}Ni_{1-y}Co_yO_2$ series when substituting nickel with cobalt due to the increasing possibility of electron density removal the O^{2-}:2p band. One compound in particular, $LiNi_{0.85}Co_{0.15}O_2$, was found to have better capacity (180 mAh g^{-1}) as compared to $LiCoO_2$ (140 mah g^{-1}) and the difference was related to the band positions [8].

The identification of hydrogen uptake presented here reinforces the previous findings as they relate to the relative chemical instabilities of the chemically delithiated $Li_{1-x}CoO_2$ and $Li_{1-x}NiO_2$ systems where increasing amounts of cobalt increase the amount of instability found during chemical charging. In the case of lithiated spinel $Li_2Co_2O_4$, when compared to layered $LiCoO_2$, even though both compounds contain cobalt, it appears that it is more difficult to incorporate protons into the more complex $Li_2Co_2O_4$ spinel lattice as compared to the layered $LiCoO_2$ lattice and thus the chemical instability in $Li_2Co_2O_4$ is primarily relieved by oxygen loss rather than proton insertion. In general the positions of the $M^{3+/4+}$:3d band relative to the top of the O^{2-}:2p band and the resulting differences in the chemical instability seem to correlate with the reversible capacity values of various oxide cathodes.

The close agreement between the hydrogen content values obtained with PGAA and the hydrogen values that can be calculated from the redox titration data and application of the charge neutrality principle, assuming no oxygen loss, validates the applicability of PGAA to obtain quantitative hydrogen contents. The slightly higher hydrogen content values obtained with the PGAA in a couple of cases could be due to adsorbed water on the surface of the sample. It should be noted that these findings may not necessarily represent the exact failure mechanisms in actual lithium ion cells since the operating conditions are different for the electrochemical extraction of lithium as compared to the chemical lithium extraction and thus it is not clear whether proton insertion occurs at deep charging of actual lithium ion cells. Nevertheless, this study reveals the mechanisms that are occurring to relieve the chemical instabilities undergone by the various cathode oxide systems investigated.

The presence of hydrogen was complemented by TGA and mass spectrometry studies in a few cases. The absence of any weight loss below 100 °C in the TGA plots indicates that the samples are free from adsorbed acetonitrile or moisture. It should be noted that it is difficult to calculate the expected weight loss for manganese containing compounds because the final products, after undergoing TGA, are a complex mix of two or more phases.

For $Li_{1-x}CoO_2$, assuming the final product after TGA to be $(0.05)LiCoO_2$ and $(0.95/3)Co_3O_4$ as indicated by the XRD data, the observed weight loss of 11.6 % agrees well with the expected weight loss of 11.5 % (Figure 6.4) for the formula $H_{0.39}Li_{0.05}CoO_2$ with hydrogen in the lattice. The expected weight loss of 7.8 % for the formula $Li_{0.05}CoO_{1.80}$ with a loss of oxygen from the lattice with the same oxidation state of 3.56+ for Co in both the formulas does not match the measured weight loss (11.6 %) value and thus reinforces the conclusion that hydrogen insertion is occurring in this layered system in order to accommodate the chemical instability.

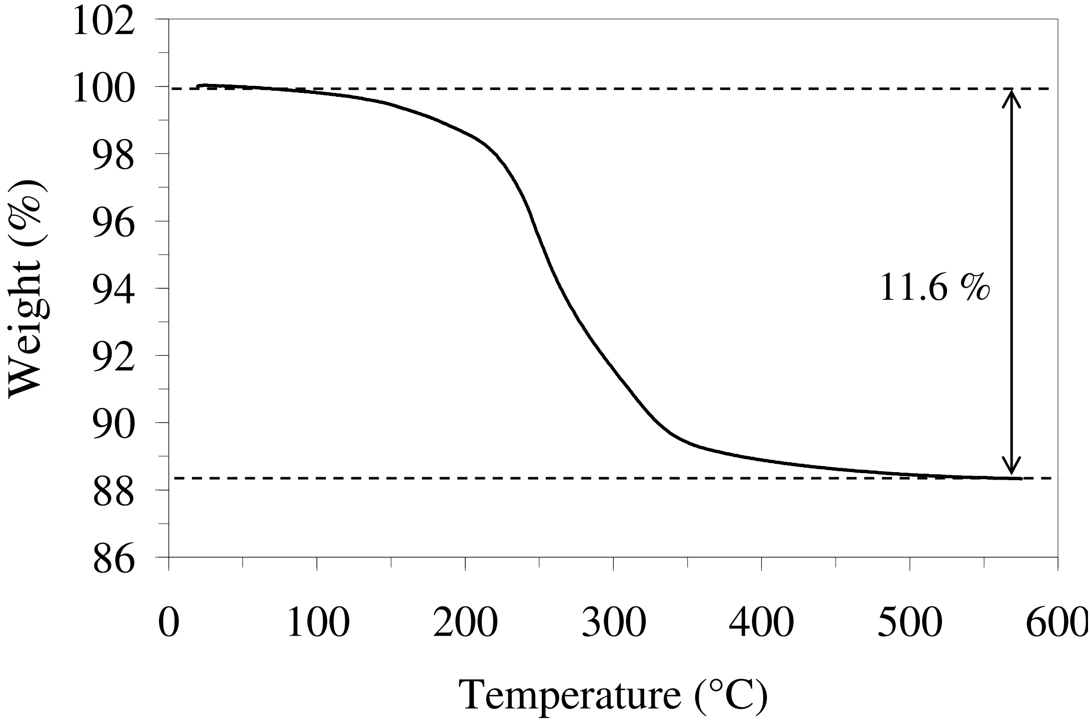

Figure 6.4: TGA plot of chemically delithiated $H_{0.39}Li_{0.05}CoO_2$.

Similarly, for $Li_{1-x}NiO_2$, assuming the final product after TGA to be $(0.08)LiNiO_2$ and $(0.92)NiO_2$ as observed by the XRD data, the measured weight loss was found to be 15.6 % as reported in Choi (2006) (Figure 6.5) [128]. This agrees well with the expected weight loss of 16.1 % associated with the final formula $Li_{0.08}NiO_2$ where no hydrogen insertion or loss of oxygen is expected as presented in Table 6.3.

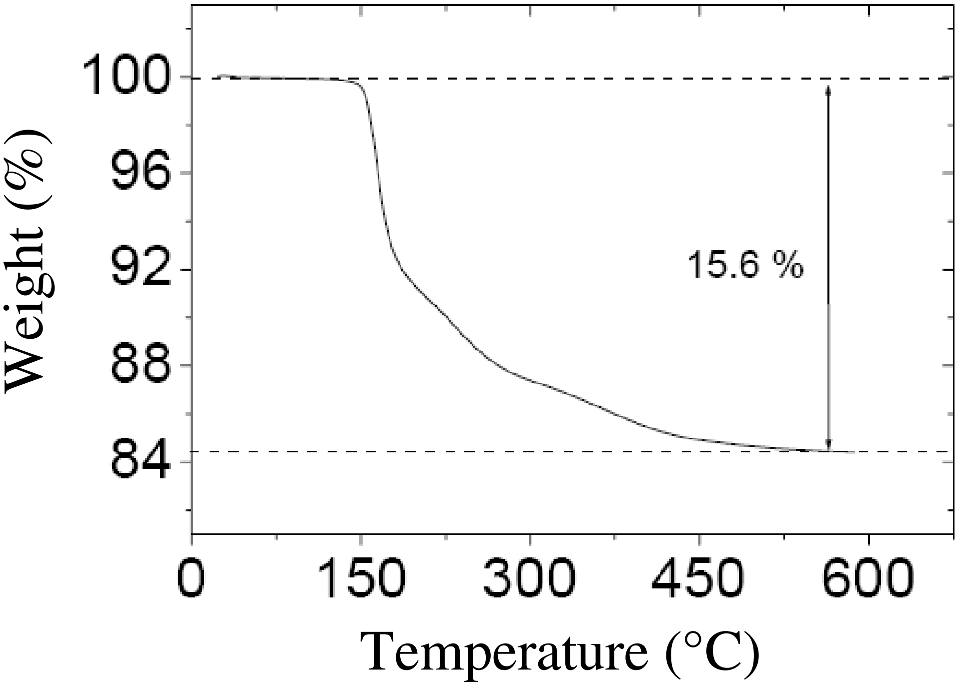

Figure 6.5: TGA plot of chemically delithiated $Li_{0.09}NiO_2$ [128].

Table 6.3 also gives the chemical analysis and PGAA data for the spinel $Li_{1-x}Co_2O_4$ that was obtained by chemically extracting lithium from the low temperature $LiCoO_2$, which is a lithiated spinel $Li_2Co_2O_4$ [123-126]. While the expected amount of proton based on the lithium content and oxidation state analysis assuming no oxygen loss occurs from the lattice is 0.64, the PGAA data indicate a much lower proton content of 0.18. This suggests the charge compensation in the spinel $Li_{1-x}Co_2O_4$ at deep lithium extraction may occur both by proton insertion and oxygen loss from the lattice. This conclusion is supported by the TGA data as presented in Figure 6.6. The observed weight loss of 6.5 % is smaller than the expected value of 8.3 % for the formula $H_{0.64}Li_{0.6}Co_2O_4$ (assuming only proton insertion) but higher than the expected value of 5.4 % for the formula $Li_{0.6}CoO_{3.68}$ (assuming only oxygen loss) where the final product after TGA is $(0.6)LiCoO_2$ and $(1.4/3)Co_3O_4$ as indicated by the XRD data. Based on the observed weight loss and charge neutrality principle, the calculated composition is $H_{0.24}Li_{0.6}Co_2O_{3.80}$ as indicated in Table 6.3, which is in close agreement with the proton content obtained from PGAA. Thus, the chemical instability associated with the $Co^{3+/4+}$ couple is largely relieved by a loss of oxygen from the lattice in the case of spinel $Li_{1-x}Co_2O_4$ possibly due to the difficulty of incorporating protons into the spinel lattice in contrast to the layered $Li_{1-x}CoO_2$ lattice [33].

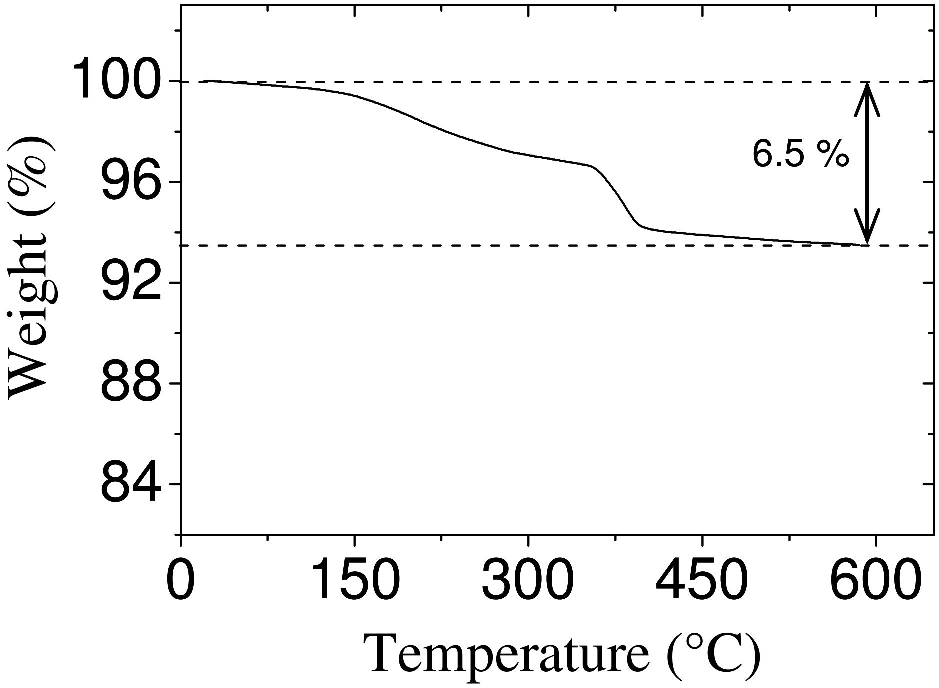

Figure 6.6: TGA plot of chemically delithiated $H_{0.24}Li_{0.60}Co_2O_{3.80}$ [33].

Further, as was reported earlier, the mass spectra reveal the simultaneous release of both H_2O and oxygen at $T > 250\ ^oC$ for a few systems reconfirming the presence of hydrogen in the lattice rather than from the samples' surface [33, 128].

In previous studies [8, 26-28, 30, 121, 122] the constancy of the oxidation state of the transition metal ions at lower lithium contents was believed to be due to a loss of oxygen from the lattice, assuming no hydrogen insertion occurs during the chemical delithiation process considering the non-aqueous reaction medium. However, there is a possibility of an ion exchange of Li^+ by H^+ ions that could be produced from acetonitrile in the presence of a powerful oxidizer like NO_2BF_4 [129]. In this regard, ion exchange of Li^+ by H^+ as well as loss of oxygen from the lattice have been reported by Robertson and Bruce [34, 130] during the electrochemical charging of Li_2MnO_3 and $Li_xMn_{1-y}Li_yO_2$ beyond Mn^{4+} [33].

While it is not anticipated that hydrogen would be available for uptake into the oxide cathode lattice given the non-aqueous reaction medium, it is clear from the data presented above that there is a definite source of protons present. The most likely source of hydrogen in this case is the acetonitrile solution. It is possible for acetonitrile to be decomposed by a strong oxidizer such as NO_2BF_4 [129]. The decomposition may be accelerated in the presence of highly oxidized Co^{4+} or Ni^{4+} ions that show catalytic activity [131]. Water, present as a trace impurity in the acetonitrile, is another possible source of hydrogen. Although the hydrogen content in the reaction medium may be small, the significant amount of holes present in the O^{2-}:2p band due to the chemical instability of the highly oxidized Co^{4+} or Ni^{4+} ions during deep lithium extraction may lead to a strong adsorption of protons on the delithiated oxide cathode surface [33, 132, 133].

6.1.4 Summary of Work

The major goal of this study was the direct, quantitative measurement of hydrogen content, if any, present in various chemically delithiated oxide cathodes by PGAA. The detection of proton levels would put to rest speculation regarding whether or not oxygen is indeed being lost from a given cathode system during chemical delithiation. The PGAA results are complemented and reinforced by TGA and mass spectroscopic data.

While some cathodes such as layered $LiCoO_2$, $LiNi_{0.5}Mn_{0.5}O_2$, and $LiNi_{1/3}Mn_{1/3}Co_{1/3}O_2$ show relatively high levels of proton uptake, other compounds like layered $LiNiO_2$, o-$LiMnO_2$, spinel $LiMn_2O_4$, spinel $LiMn_{1.58}Ni_{0.42}O_2$, and olivine $LiFePO_4$ do not. The proton uptake is thought to occur to relieve the chemical instability that may occur at deep lithium extraction due to a significant overlap of the $M^{3+/4+}$:3d band with the top of the O^{2-}:2p band.

While the layered $Li_{1-x}CoO_2$, which is currently used as a cathode in commercial lithium ion batteries, incorporates a significant amount of hydrogen into the lattice at deep chemical lithium extraction as indicated by the PGAA data and complemented by other techniques, layered o-$LiMnO_2$, layered $LiNiO_2$, spinel $LiMn_2O_4$, spinel $LiMn_{1.58}Ni_{0.42}O_2$, and olivine $LiFePO_4$ cathodes incorporate little or no protons into the lattice. The incorporation of protons into chemically delithiated $Li_{1-x}CoO_2$ is to relieve the chemical instability arising from a removal of significant amount of electron density from the O^{2-}:2p band. Thus the capacity limitation (50 % of the theoretical capacity) of the layered $Li_{1-x}CoO_2$ cathode compared to other layered cathodes that are richer in manganese or nickel may possibly be related to the chemical instability arising during chemical delithiation. The differences could be related to the relative positions of the $M^{n+/(n+1)+}$:3d band with respect to the top of the O^{2-}:2p band and the consequent chemical instability arising from an introduction of significant amount of holes into the O^{2-}:2p band at deep lithium extraction.

6.2 Systematic Hydrogen Determination in Layered $Li_{1-x}Ni_{1-y-z}Mn_yCo_zO_2$ Cathodes

As previously discussed, nickel and manganese-containing lithium ion cathode compositions, with the same initial O3-type structure as $LiCoO_2$, such as layered $LiNi_{0.5}Mn_{0.5}O_2$ and $LiNi_{1/3}Mn_{1/3}Co_{1/3}O_2$ have been shown to exhibit higher reversible capacities [9, 10, 12, 17, 117-120]. However, it is unclear in literature why such capacity differences occur given the fact that all of these compounds have the same O3-layered structure. It has been hypothesized that the reversible capacity differences can be attributed to chemical instabilities arising at deep extraction of lithium from the lattice. The instability has been linked to the positions of the $Co^{3+/4+}$:3d and $Ni^{3+/4+}$:3d bands relative to the location of the O^{2-}:2p band [8, 27-29]. Oxygen loss from the lattice was suggested to be the primary mechanism for relieving the chemical instability.

These conclusions are a result of systematic redox titration studies that indirectly provide oxygen content values by way of the charge neutrality principle. However, the data could be skewed if protons are being inserted into the lattice during said chemical delithiation. Thus, a direct determination of hydrogen content, if any, in the chemically delithiated oxide cathodes would fully establish the issue of which mechanism(s) is occurring during deep chemical charging of O3-type layered $Li_{1-x}Ni_{1-y-z}Mn_yCo_zO_2$ cathodes.

In an effort to fingerprint the actual mechanism(s) occurring (*i.e.* proton insertion and/or oxygen loss) in these $Li_{1-x}Ni_{1-y-z}Mn_yCo_zO_2$ systems to alleviate their chemical instability, PGAA has been applied to a number of samples to determine the amount of proton insertion, if any, occurring during chemical delithiation. In this regard, focus has been placed on systematically analyzing the layered $LiCoO_2$, $LiNi_{0.5}Mn_{0.5}O_2$, and $LiNi_{1/3}Mn_{1/3}Co_{1/3}O_2$ compounds in order to determine whether proton insertion is occurring and pinpoint the onset of the chemical instability as a function of lithium content for these particular cathodes. These studies have been accomplished by way of chemically extracting lithium from layered oxides using NO_2BF_4 oxidizer under an inert argon environment [8, 27-29].

6.2.1 Experimental

$LiCoO_2$ was synthesized by a solid-state reaction of Co_3O_4 (GFS Chemicals) and Li_2CO_3 (Alfa Aeasar) for 24 h in air at 900 °C. $LiNi_{0.5}Mn_{0.5}O_2$ was synthesized by firing required amounts of co-precipitated hydroxides of Ni and Mn with $LiOH{\cdot}H_2O$ for 24 h in air at 900 °C. $LiNi_{1/3}Mn_{1/3}Co_{1/3}O_2$ was prepared by firing required amounts of co-precipitated hydroxides of Ni, Mn, and Co with $LiOH{\cdot}H_2O$ for 24 h in air at 900 °C. The Ni, Mn, and Co hydroxides were obtained by slowly adding an aqueous solution containing required amounts of Ni^{2+}, Mn^{2+}, and Co^{2+} into a LiOH solution followed by filtering and washing the precipitate with de-ionized water. Each of the above compounds underwent heating and cooling rates, respectively, of 1 °C/min.

The chemically delithiated $Li_{1-x}CoO_2$, $Li_{1-x}Ni_{0.5}Mn_{0.5}O_2$, and $Li_{1-x}Ni_{1/3}Mn_{1/3}Co_{1/3}O_2$ samples were then obtained by stirring the respective parent compounds with a non-aqueous acetonitrile solution of NO_2BF_4 for 2 days under an inert argon environment. The resulting chemically delithiated lithium samples were then washed several times with fresh acetonitrile to remove the remaining $LiBF_4$ and then dried under vacuum. After undergoing lithium extraction, the compounds were carefully handled and stored in an evacuated desiccator to limit exposure to ambient air and reduce the possibility of moisture contamination as well as the possible spontaneous reduction of the transition metal ions. Lithium was chemically extracted from $LiCoO_2$, $LiNi_{0.5}Mn_{0.5}O_2$, and $LiNi_{1/3}Mn_{1/3}Co_{1/3}O_2$ in a systematic fashion in order to obtain three sets of compounds containing approximately 80 %, 60 %, 40 %, 20 %, and 0 % lithium content relative to the parent compound (100 %). After extraction, each compound (including the parent compounds) underwent characterization where the lithium content of the delithiated samples was determined by AAS, average oxidation state of the transition metals was determined by wet-chemical redox titration, the hydrogen content was measured by PGAA, and the charge neutrality principle was applied for the calculation of the oxygen content. Structural characterization was accomplished by XRD. $Li_{1-x}CoO_2$ was also analyzed by TGA and its weight loss was observed to complement the PGAA data. The $Li_{1-x}CoO_2$, $Li_{1-x}Ni_{0.5}Mn_{0.5}O_2$ and $Li_{1-x}Ni_{1/3}Mn_{1/3}Co_{1/3}O_2$ samples were analyzed before the PGAA facility underwent extensive reconstruction.

To avoid moisture adsorption onto the surface of the delithiated samples during PGAA, the samples were packaged in custom made Teflon® vials and were then purged under helium atmosphere while being irradiated for 2 h at a reactor power of 950 kW. Also, as discussed in Section 4.3, a correction had to be made for the $Li_{1-x}CoO_2$ and $Li_{1-x}Ni_{1/3}Mn_{1/3}Co_{1/3}O_2$ samples due to the spectral interference between hydrogen (2223.25 keV) and cobalt (2221.61 keV) that cannot be deconvoluted by the HPGe gamma-ray detector. The ^{59}Co interference is addressed by utilizing the PGAA reference peak method as previously outlined in Section 4.3.

6.2.2 Results and Discussion

The evolving XRD patterns for $Li_{1-x}CoO_2$, $Li_{1-x}Ni_{0.5}Mn_{0.5}O_2$, and $Li_{1-x}Ni_{1/3}Mn_{1/3}Co_{1/3}O_2$ are presented in Figures 6.7, 6.8, and 6.9, respectively. From the

XRD results for each sample it is clear that $Li_{1-x}CoO_2$ maintains an O3 phase for $0.5 \leq 1-x \leq 1$ that then begins to evolve into a mixed O3 and P3 phase structure from $0 \leq 1-x \leq 0.5$ where eventually a pure P3 phase is obtained. For long enough delithiation reaction times (> 2 days), an O1-type structure would be born [27, 28]. $Li_{1-x}Ni_{0.5}Mn_{0.5}O_2$ maintains its O3-type structure without the formation of any new phases throughout the delithiation process ($0 \leq 1-x \leq 1$) [28]. $Li_{1-x}Ni_{1/3}Mn_{1/3}Co_{1/3}O_2$ maintains its initial O3-type structure down to relatively low lithium contents (< 0.23) before developing into an O1-type structure [30]. These results are consistent with what was previously reported for these systems [27, 28, 30].

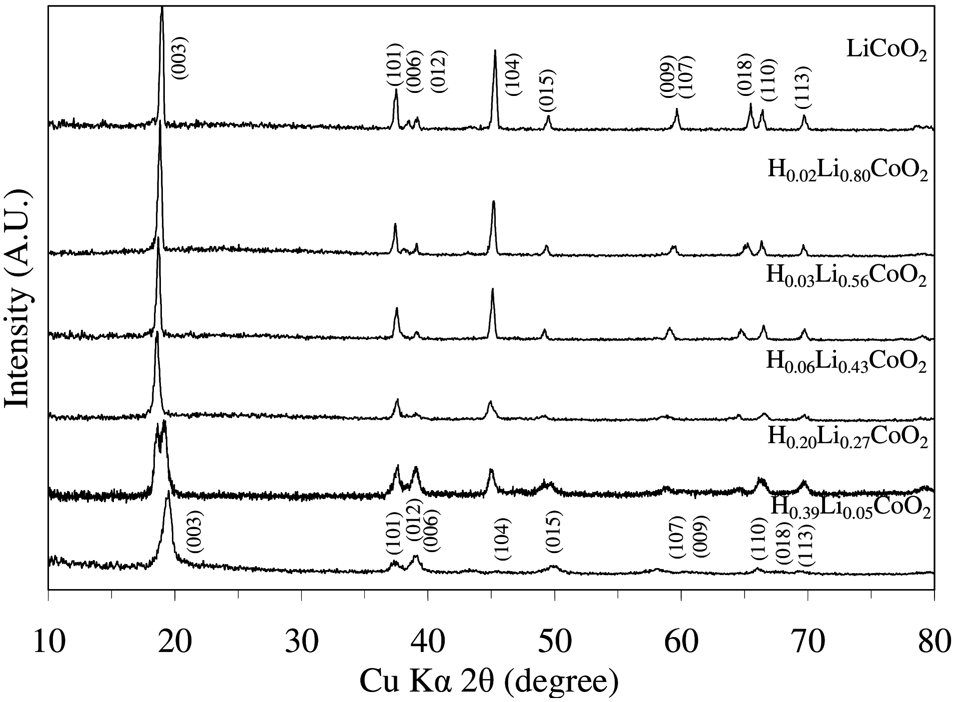

Figure 6.7: XRD pattern transformation of $Li_{1-x}CoO_2$ for $0 \leq 1-x \leq 1$.

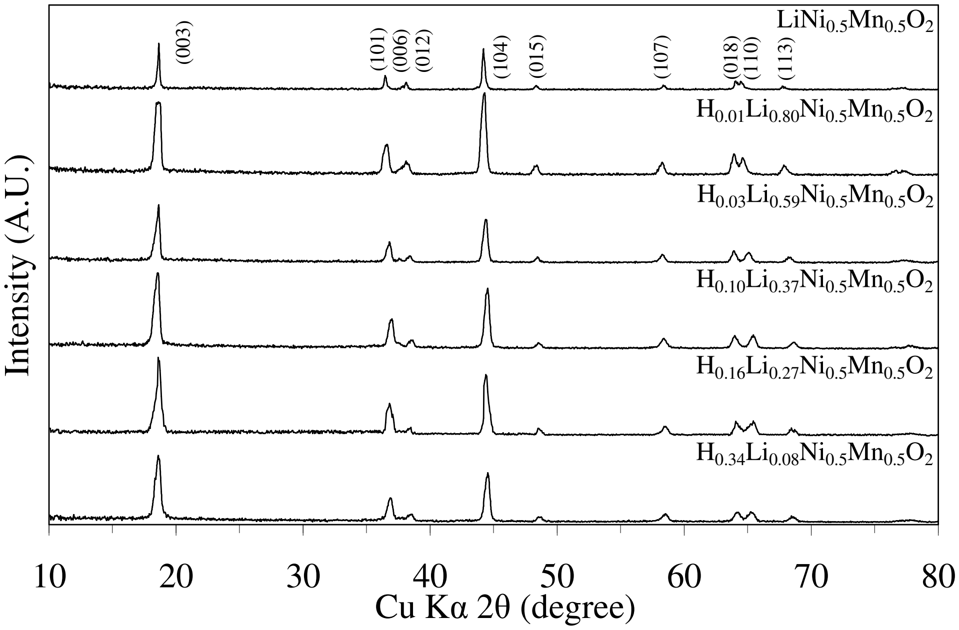

Figure 6.8: XRD patterns of $Li_{1-x}Ni_{0.5}Mn_{0.5}O_2$ for $0 \leq 1-x \leq 1$.

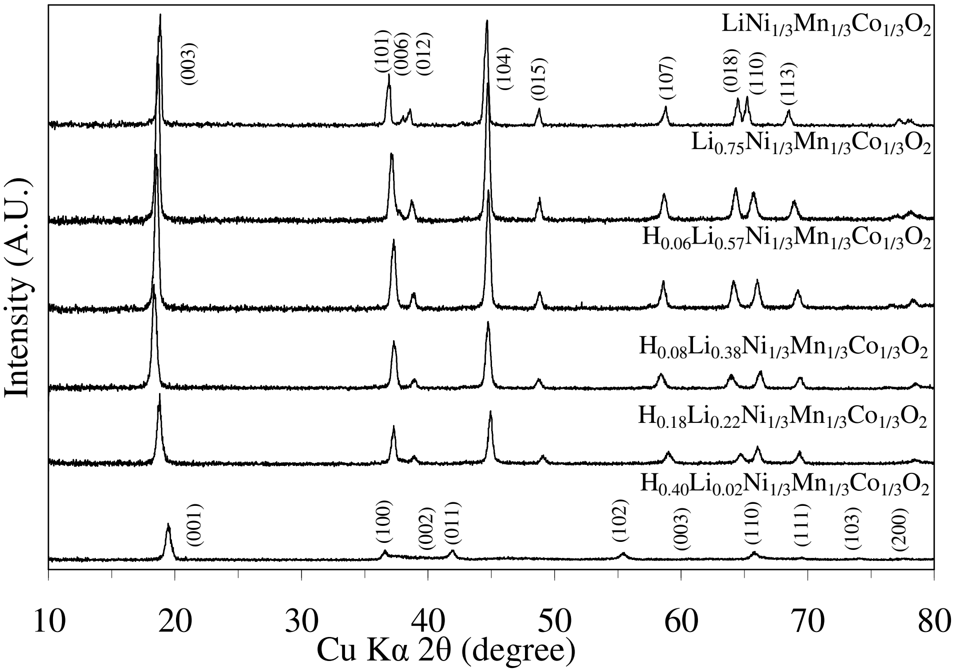

Figure 6.9: XRD patterns of $Li_{1-x}Ni_{1/3}Mn_{1/3}Co_{1/3}O_2$ for $0 \leq 1-x \leq 1$.

The hydrogen signals measured for each sample with PGAA are shown below. The plots show the sample mass-normalized gamma count rate detected for hydrogen, after background subtraction, as a function of gamma-ray energy. For each plot, the 2223.25 keV hydrogen gamma-ray peak associated with its respective cathode sample can be seen along with other distinct peaks in the spectra that originate from the sample or the background materials.

For $Li_{1-x}CoO_2$, only one significant peak can be found in the 2220 – 2226 keV gamma-ray energy range. This single peak is attributed to the combined signal arising from the hydrogen (2223.25 keV) and cobalt (2221.61 keV) gamma-ray lines as shown in Figure 6.10. From the gamma-ray spectrum, it can be qualified that there is a noticeable increase in the peak area at lower lithium contents due to the relatively large insertion of hydrogen into the $Li_{1-x}CoO_2$ lattice. Similarly, the Compton continuum is also increased as is expected for the increased gamma-ray signal.

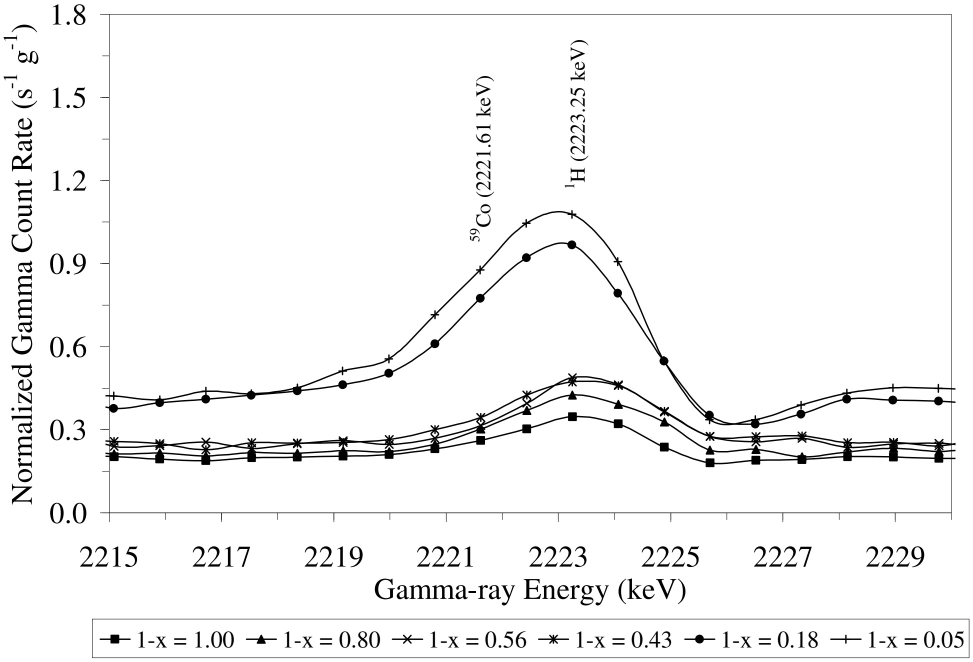

Figure 6.10: Normalized hydrogen signal (2223.25 keV) for the $Li_{1-x}CoO_2$ system.

The cobalt peak (447.71 keV) used for purposes of the hydrogen peak correction is shown in Figure 6.11 along with other surrounding cobalt peaks (*i.e.* 435.68 keV and 461.08 keV, respectively). From Figure 6.11, it can also be seen, from a qualitative assessment, that boron is not present in the sample as evidence by the absence of the 477.59 keV gamma peak.

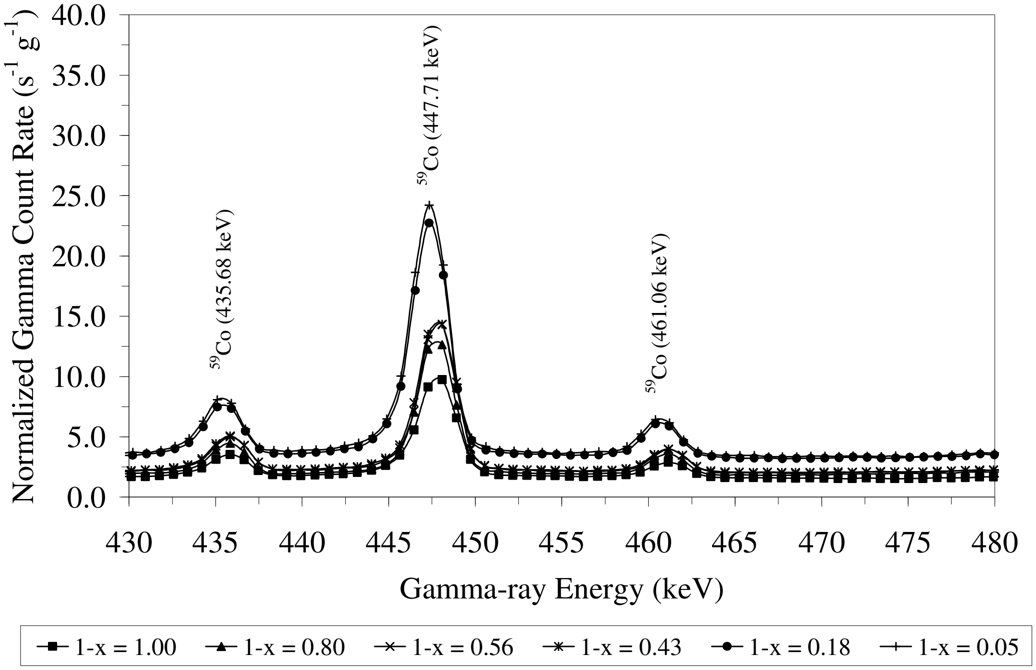

Figure 6.11: Normalized cobalt signal (447.711 keV) and other surrounding cobalt peaks for the $Li_{1-x}CoO_2$ system.

In the case of $Li_{1-x}Ni_{0.5}Mn_{0.5}O_2$ (Figure 6.12), the 2210.29 keV peak is originating from the manganese present in the sample, the 2215.36 keV peak is coming from the HPGe detector's germanium crystal after becoming activated by scattered neutrons, and the 2229.75 keV gamma-ray peak is born in the fluorine present in the Teflon® vial. It can also be qualitatively assessed from the plot that the proton signal, and thus proton content in each sample, increases with decreasing lithium content while the other peak heights remain relatively constant as expected.

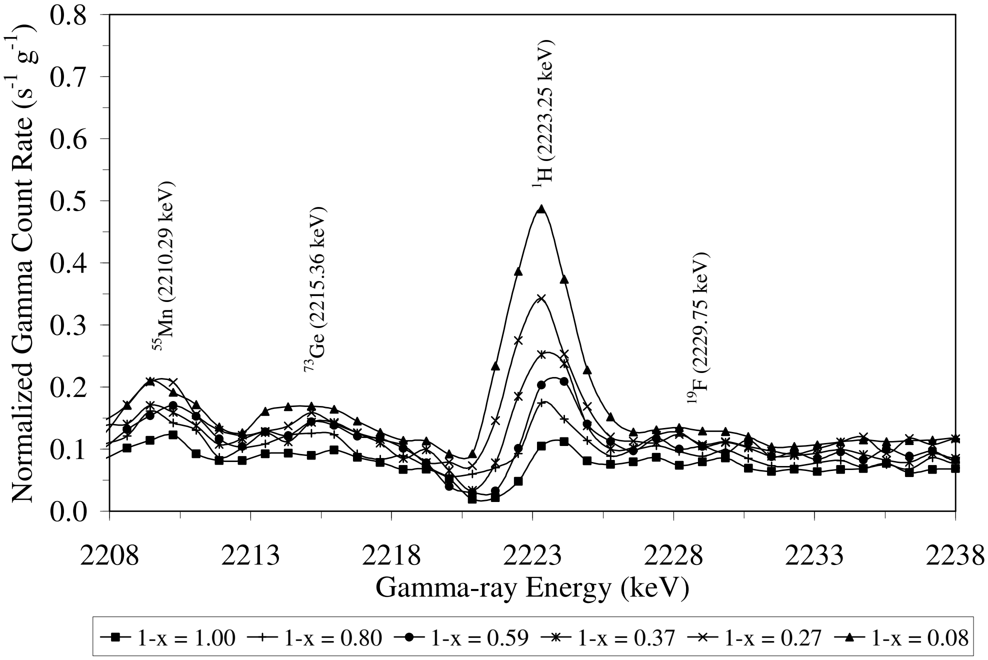

Figure 6.12: Normalized hydrogen signal (2223.25 keV) for the $Li_{1-x}Ni_{0.5}Mn_{0.5}O_2$ system.

The sample mass-normalized hydrogen signals for the $Li_{1-x}Ni_{1/3}Mn_{1/3}Co_{1/3}O_2$ system are shown in Figure 6.13. Like $Li_{1-x}CoO_2$, the hydrogen peaks for $Li_{1-x}Ni_{1/3}Mn_{1/3}Co_{1/3}O_2$ is actually a summation of the ^{59}Co-2221.61 keV and ^{1}H-2223.25 keV gamma-ray signal. Qualitatively, it is seen that the maximum mass-normalized peak height for $Li_{0.02}Ni_{1/3}Mn_{1/3}Co_{1/3}O_2$ is comparable to the maximum mass-normalized peak height of $Li_{0.05}CoO_2$. Like in the $Li_{1-x}CoO_2$ spectra, the ^{73}Ge (2215.36 keV) and ^{19}F (2229.75 keV) peaks that were visible in the $Li_{1-x}Ni_{0.5}Mn_{0.5}O_2$ spectra are not detectable in these spectra due to the higher Compton continuum that results from increased gamma-ray reaction rates that originate from cobalt.

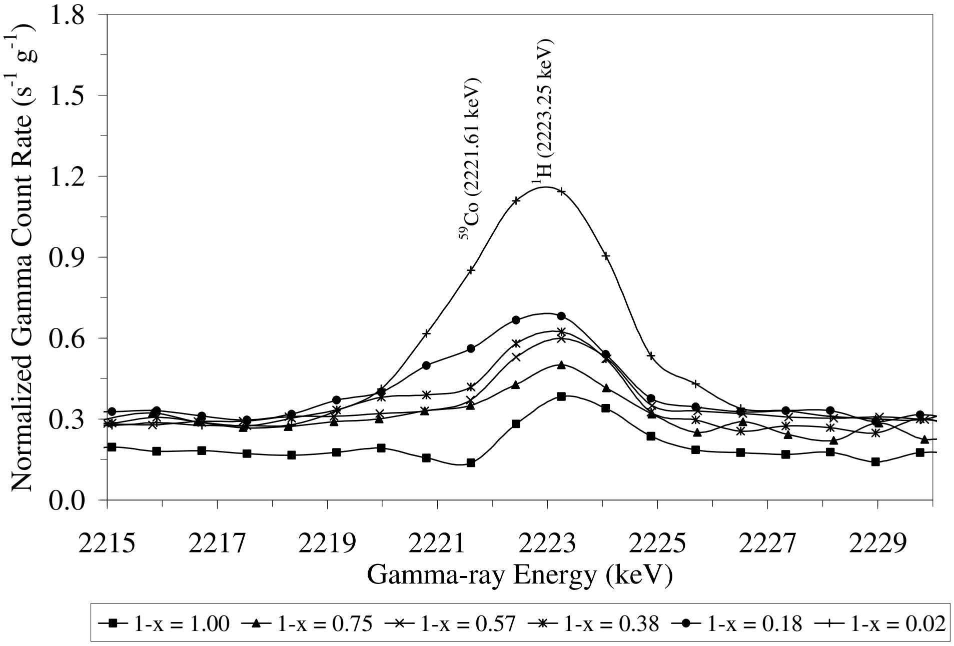

Figure 6.13: Normalized hydrogen signal (2223.25 keV) for the $Li_{1-x}Ni_{1/3}Mn_{1/3}Co_{1/3}O_2$ system.

A qualitative assessment of Figure 6.14 provides an indication of the elements present in the $Li_{1-x}Ni_{1/3}Mn_{1/3}Co_{1/3}O_2$ system samples. The 447.71 keV cobalt peak is prominently featured, as is found in the case of $Li_{1-x}CoO_2$, along with its neighboring 435.68 and 461.08 keV ^{59}Co gamma-ray peaks, respectively. Of further interest is the visible gamma peaks that are originating from ^{55}Mn (454.38 keV) and ^{58}Ni (464.98 keV), both of which are present as elements in the $Li_{1-x}Ni_{1/3}Mn_{1/3}Co_{1/3}O_2$ samples. These gamma lines were not present in the $Li_{1-x}CoO_2$ spectra, thus providing further evidence that the detection capabilities of the PGAA system, for purposes of analyzing a variety of lithium ion oxide cathode materials, are adequate as it is straightforward to distinguish and properly identify the range of elements present in the various samples. The Doppler broadened ^{10}B (477.59 keV) gamma line originating from shielding materials can also be seen in the spectra presented in Figure 6.14. The levels of boron present are within the acceptable range and therefore are not thought to cause an elevated source of error in the form of neutron attenuation.

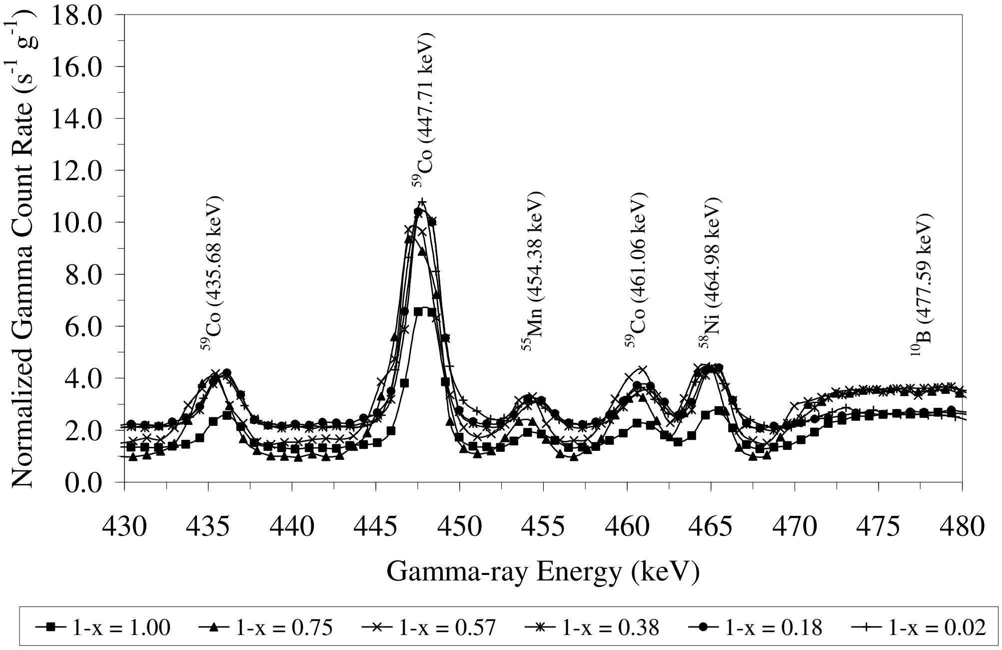

Figure 6.14: Normalized cobalt signal (447.71 keV) and other surrounding cobalt, nickel, and manganese peaks for the $Li_{1-x}Ni_{1/3}Mn_{1/3}Co_{1/3}O_2$ system.

Table 6.4 presents the quantified hydrogen content as obtained by PGAA, the lithium content as determined by AAS, the average oxidation state (M^{n+}) as measured by permanganate titration, and the final composition as found through the application of the charge neutrality principle (assuming no oxygen is lost) for each respective layered $Li_{1-x}Ni_{1-y-z}Mn_yCo_zO_2$ cathode system. Figures 6.15, 6.16, and 6.17 are plots of the data contained in Table 6.4 for $Li_{1-x}CoO_2$, $Li_{1-x}Ni_{0.5}Mn_{0.5}O_2$, and $Li_{1-x}Ni_{1/3}Mn_{1/3}Co_{1/3}O_2$, respectively, where the oxidation state, proton content, and oxygen content for each layered system is illustrated as a function of lithium content. The oxidation state trends presented as a function of lithium content in Figure 6.15, 6.16, and 6.17 are consistent with what was previously reported for these systems [27, 28, 30].

Table 6.4: PGAA and Chemical analysis data obtained for $Li_{1-x}CoO_2$, $Li_{1-x}Ni_{0.5}Mn_{0.5}O_2$, and $Li_{1-x}Ni_{1/3}Mn_{1/3}Co_{1/3}O_2$.

$Li_{1-x}CoO_2$ ($0 \leq 1\text{-}x \leq 1$)

H content (± 0.02)	Li content (± 0.02)	M^{n+} (± 0.02)	Final Composition[a]
0.37	0.05	3.56	$H_{0.39}Li_{0.05}CoO_2$
0.20	0.27	3.53	$H_{0.20}Li_{0.27}CoO_2$
0.07	0.43	3.51	$H_{0.06}Li_{0.43}CoO_2$
0.05	0.56	3.41	$H_{0.03}Li_{0.56}CoO_2$
0.03	0.80	3.18	$H_{0.02}Li_{0.80}CoO_2$
0.00	1.00	3.00	$LiCoO_2$

$Li_{1-x}Ni_{0.5}Mn_{0.5}O_2$ ($0 \leq 1\text{-}x \leq 1$)

H content (± 0.01)	Li content (± 0.02)	M^{n+} (± 0.02)	Final Composition[a]
0.34	0.08	3.58	$H_{0.34}Li_{0.08}Ni_{0.5}Mn_{0.5}O_2$
0.16	0.27	3.55	$H_{0.18}Li_{0.27}Ni_{0.5}Mn_{0.5}O_2$
0.10	0.37	3.54	$H_{0.09}Li_{0.37}Ni_{0.5}Mn_{0.5}O_2$
0.03	0.59	3.35	$H_{0.08}Li_{0.59}Ni_{0.5}Mn_{0.5}O_2$
0.01	0.80	3.18	$H_{0.02}Li_{0.80}Ni_{0.5}Mn_{0.5}O_2$
0.00	1.00	3.00	$LiNi_{0.5}Mn_{0.5}O_2$

$Li_{1-x}Ni_{1/3}Mn_{1/3}Co_{1/3}O_2$ ($0 \leq 1\text{-}x \leq 1$)

H content (± 0.02)	Li content (± 0.02)	M^{n+} (± 0.02)	Final Composition[a]
0.39	0.02	3.58	$H_{0.40}Li_{0.02}Ni_{1/3}Mn_{1/3}Co_{1/3}O_2$
0.24	0.18	3.60	$H_{0.22}Li_{0.18}Ni_{1/3}Mn_{1/3}Co_{1/3}O_2$
0.10	0.38	3.54	$H_{0.08}Li_{0.38}Ni_{1/3}Mn_{1/3}Co_{1/3}O_2$
0.06	0.57	3.37	$H_{0.06}Li_{0.57}Ni_{1/3}Mn_{1/3}Co_{1/3}O_2$
0.00	0.75	3.25	$Li_{0.75}Ni_{1/3}Mn_{1/3}Co_{1/3}O_2$
0.00	1.00	3.00	$LiNi_{1/3}Mn_{1/3}Co_{1/3}O_2$

[a] Obtained based on Li content and oxidation state analysis assuming no oxygen loss occurs.

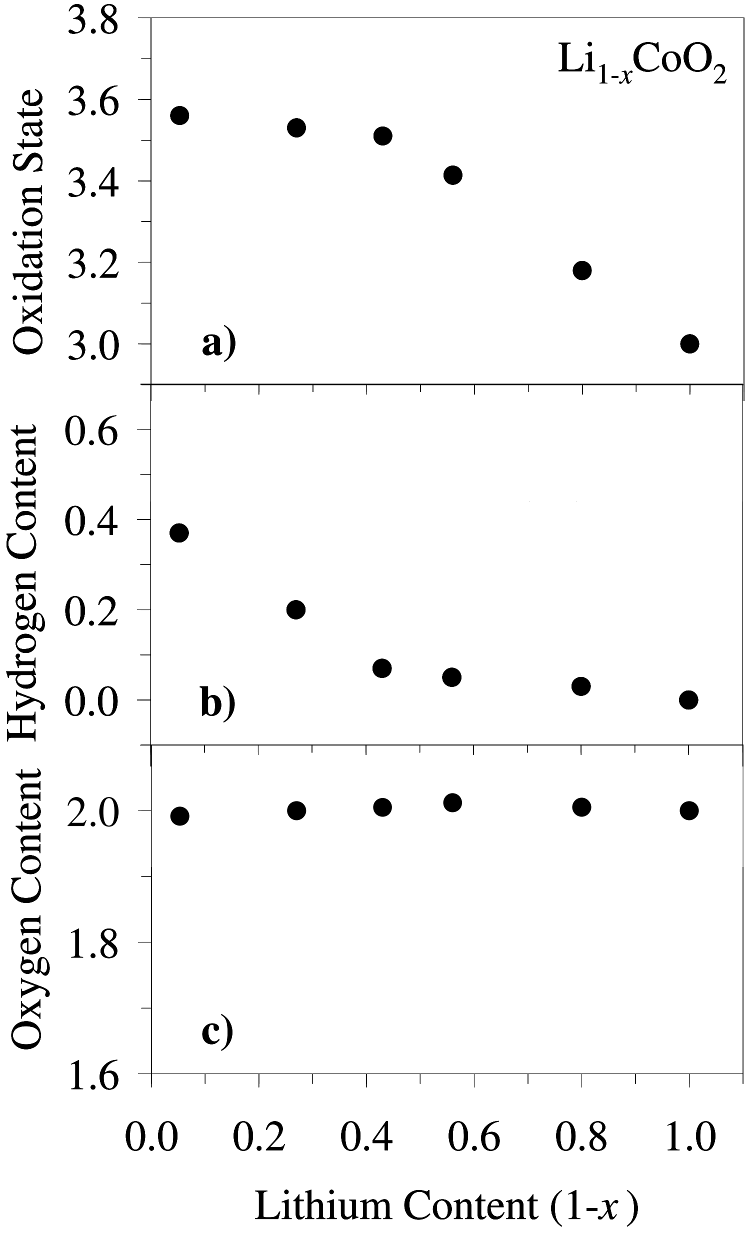

Figure 6.15: Variations of the: (a) oxidation state of the transition metal ions, (b) hydrogen content as measured by PGAA, and (c) oxygen content calculated from the measured oxidation state and proton content as a function of lithium content (1-*x*) in $Li_{1-x}CoO_2$.

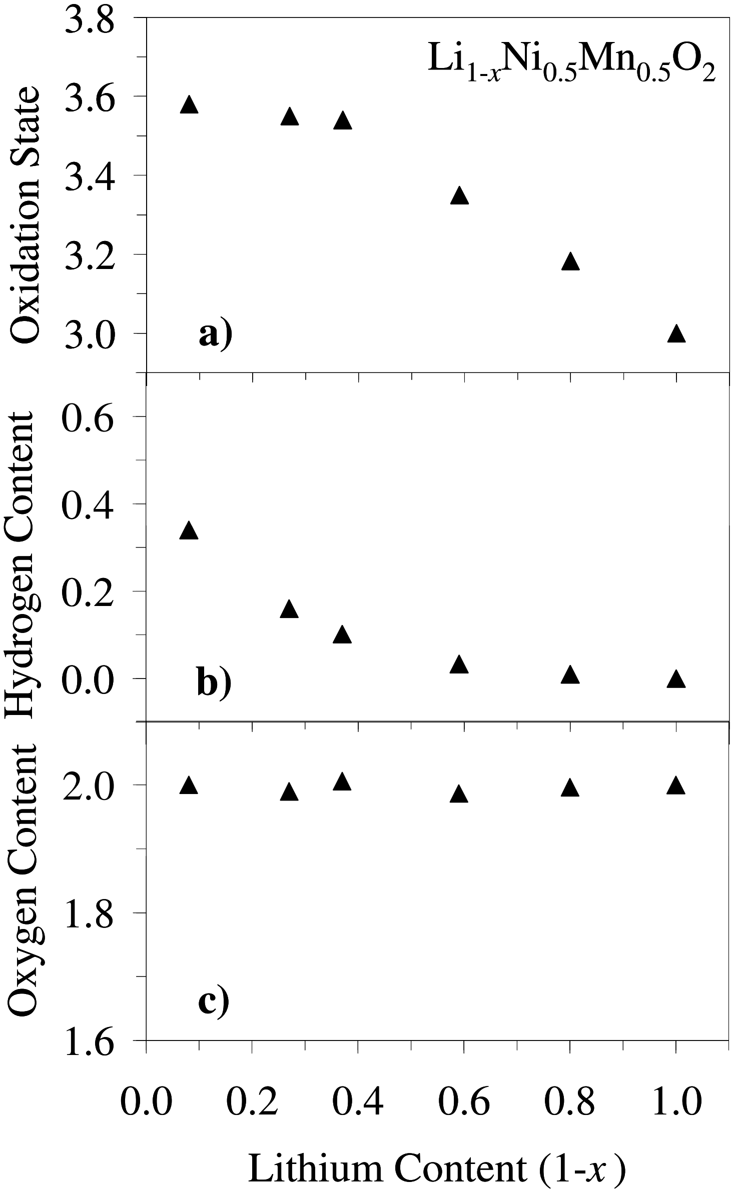

Figure 6.16: Variations of the: (a) oxidation state of the transition metal ions, (b) hydrogen content as measured by PGAA, and (c) oxygen content calculated from the measured oxidation state and proton content as a function of lithium content (1-*x*) in $Li_{1-x}Ni_{0.5}Mn_{0.5}O_2$.

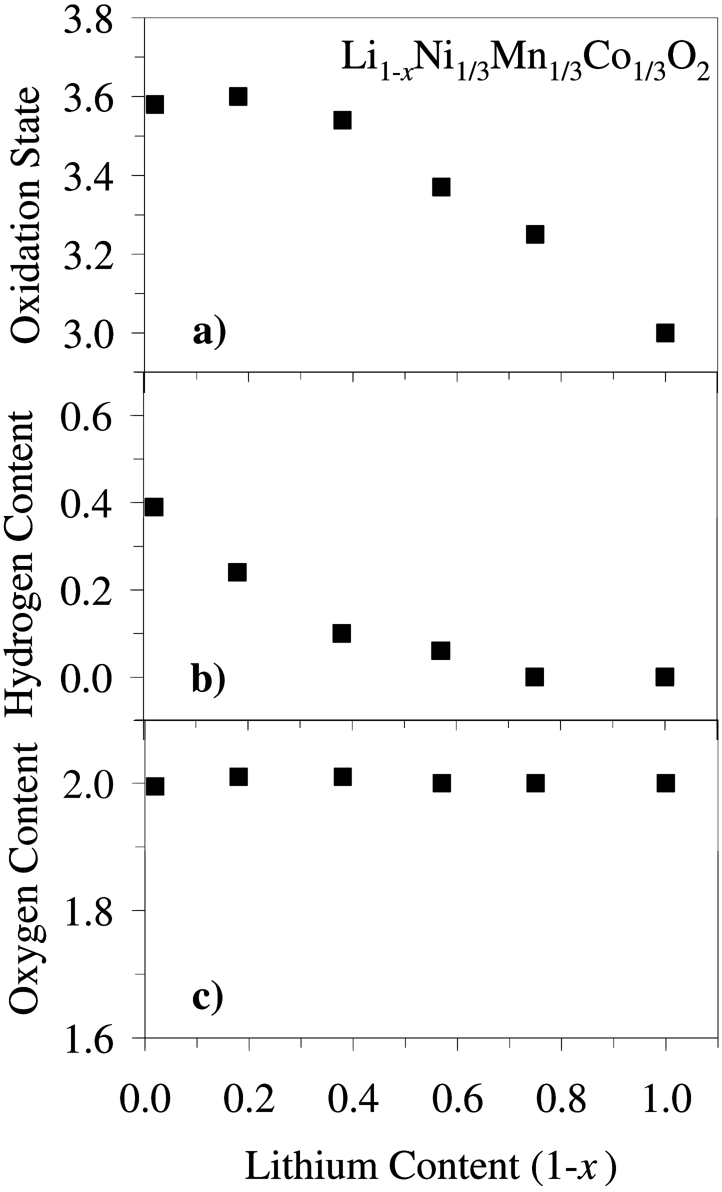

Figure 6.17: Variations of the: (a) oxidation state of the transition metals, (b) hydrogen content as measured by PGAA, and (c) oxygen content calculated from the measured oxidation state and proton content as a function of lithium content (1-x) in Li$_{1-x}$Ni$_{1/3}$Mn$_{1/3}$Co$_{1/3}$O$_2$.

It is apparent from the data that each of these cathode systems takes up a significant amount of hydrogen at low lithium contents of. Further, from the data, it is seen that the average oxidation state becomes nearly constant at a lithium content of $1\text{-}x < 0.5$ rather than continually increasing to the expected value of 3.95+ for $Li_{0.05}CoO_2$, 3.92+ for $Li_{0.08}Ni_{0.5}Mn_{0.5}O_2$, and 3.98+ for $Li_{0.02}Ni_{1/3}Mn_{1/3}Co_{1/3}O_2$, respectively, in order to compensate for the lost positive charge from the extracted lithium ions. However, while the oxidation state of $Li_{1\text{-}x}CoO_2$ begins to approach constancy at lithium contents ($1\text{-}x$) around 0.5, the oxidation state of $Li_{1\text{-}x}Ni_{0.5}Mn_{0.5}O_2$ and $Li_{1\text{-}x}Ni_{1/3}Mn_{1/3}Co_{1/3}O_2$ do not begin to deviate until lower lithium contents of < 0.4 and < 0.35, respectively.

Based on the oxidation state values and assuming no hydrogen insertion occurs, these findings are consistent with what has been previously reported for the levels of chemical instability associated with these layered oxide systems [27, 28, 30]. However, the previous reports identified oxygen loss as the mechanism by which the instability was accommodated. From this investigation it is clear that the chemical instability found in these chemically delithiated samples is in fact accommodated by an insertion of hydrogen into the cathode lattice. Further, it is apparent that H^+ ions are replacing Li^+ ions at the same point where the oxidation state trends become constant as shown in Figures 6.15, 6.16, and 6.17, respectively. Also, from charge neutrality, the oxygen content is calculated to be very nearly 2.0 for each system throughout the delithiation process, thus confirming the insertion of hydrogen into the lattice as lithium is extracted. Therefore, for the layered $Li_{1\text{-}x}CoO_2$, $Li_{1\text{-}x}Ni_{0.5}Mn_{0.5}O_2$, and $Li_{1\text{-}x}Ni_{1/3}Mn_{1/3}Co_{1/3}O_2$ systems, an ion exchange of H^+ with Li^+ readily occurs during chemical delithiation for $0 \leq 1\text{-}x \leq 1$.

Until recently, the PGAA technique had not been utilized to provide a direct determination of proton levels and thus PGAA presents clear cut evidence of which mechanism (*i.e.* proton insertion and/or oxygen loss) was occurring during chemical charging. In either case, the measured level of instability is consistent with previous reports and could be associated to the limited capacity experienced by the respective $LiCoO_2$, $LiNi_{0.5}Mn_{0.5}O_2$, and $LiNi_{1/3}Mn_{1/3}Co_{1/3}O_2$ cathode systems. The chemical instability could be related to the position of the $Co^{3+/4+}$:3d and $Ni^{3+/4+}$:3d bands relative to the top of the O^{2-}:2p band as previously discussed in Section 6.1.3 [8, 27-30]. $LiNi_{0.5}Mn_{0.5}O_2$ has a measurable level of chemical stability unlike the similarly structured $LiNiO_2$ and the reason for the difference in relative stability could be related to the positions of their respective $Ni^{3+/4+}$:e_g bands. As illustrated in Figure 6.18a, the qualitative band diagram for $Li_{1-x}Ni_{0.5}Mn_{0.5}O_2$, as proposed in [28], locates the e_g band directly above the O^{2-}:2p band in an overlapping position as compared to the $Li_{1-x}NiO_2$ band diagram (Figure 6.18b) that locates the e_g band above the O^{2-}:2p band. The overlap of the e_g band in the case of $Li_{1-x}Ni_{0.5}Mn_{0.5}O_2$ results in an onset of chemical instability at low lithium content and a consequent insertion of protons.

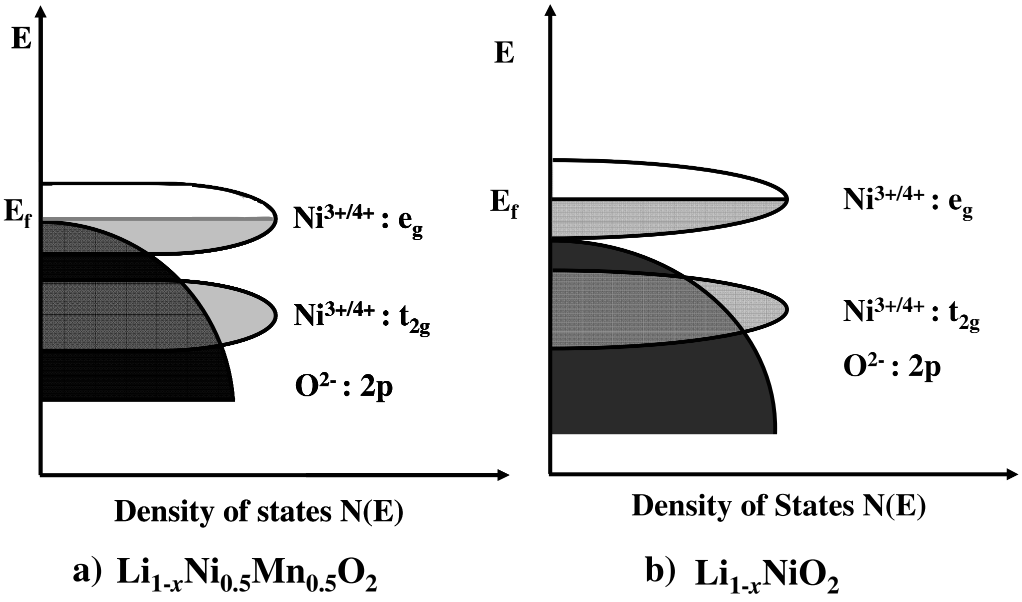

Figure 6.18: Qualitative energy band diagram for: a) $Li_{1-x}Ni_{0.5}Mn_{0.5}O_2$ and b) $Li_{1-x}NiO_2$.

For $Li_{1-x}Ni_{1/3}Mn_{1/3}Co_{1/3}O_2$ there is a significant overlap of the $Co^{3+/4+}$:t_{2g} band with the O^{2-}:2p band (Figure 6.19a), as proposed in [30], similar to the case of $Li_{1-x}CoO_2$ (Figure 6.19b) that could lead to chemical instability and proton insertion.

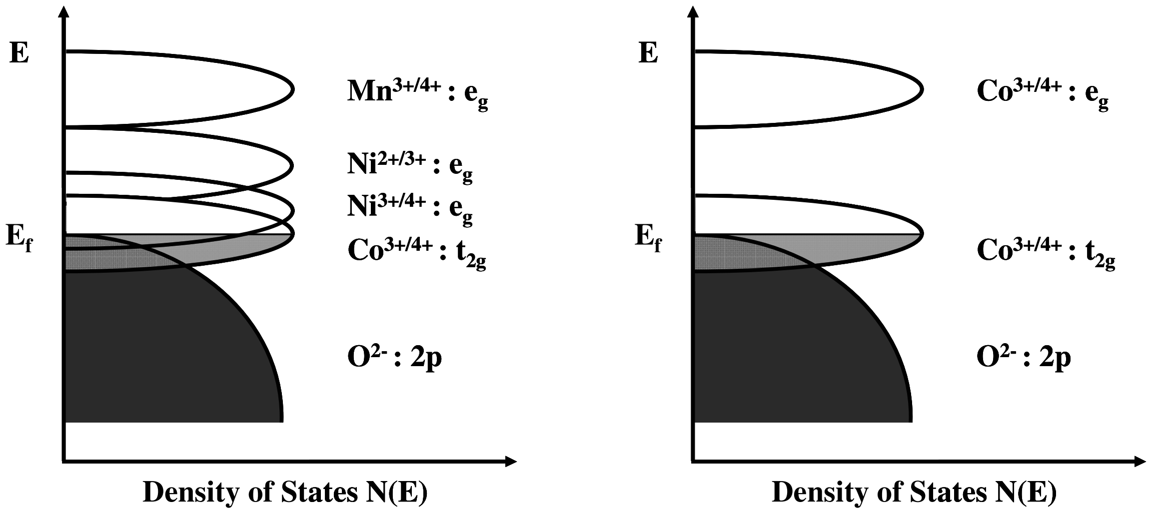

a) $Li_{1-x}Ni_{1/3}Mn_{1/3}Co_{1/3}O_2$ **b) $Li_{1-x}CoO_2$**

Figure 6.19: Qualitative energy band diagram for: a) $Li_{1-x}Ni_{1/3}Mn_{1/3}Co_{1/3}O_2$ and b) $Li_{1-x}CoO_2$.

In regards to the structure of the respective end members (*i.e.* O3, O1, and P3), some authors have hypothesized that the formation of the P3-type phase is a direct consequence of significant amounts of hydrogen insertion during the extraction of lithium [34, 134]. As previously mentioned, $Li_{1-x}CoO_2$ transforms from O3 into P3, $Li_{1-x}N_{1/3}Mn_{1/3}Co_{1/3}O_2$ forms an O1 phase after initially being O3, and $Li_{1-x}N_{0.5}Mn_{0.5}O_2$ maintains its O3 phase throughout the delithiation process. Figure 6.20 presents a comparison of the end member phases formed for the respective oxide cathode systems. From an examination of the hydrogen uptake data (Table 6.4) for each system, even though they maintain different end member structures (*i.e.* P3-CoO_2, O1-

$N_{1/3}Mn_{1/3}Co_{1/3}O_2$, and O3-$N_{0.5}Mn_{0.5}O_2$, respectively), there does not seem to be a clear correlation between the formation of the P3 phase and the amount of hydrogen insertion as each of these end members takes about 0.4 moles of H^+.

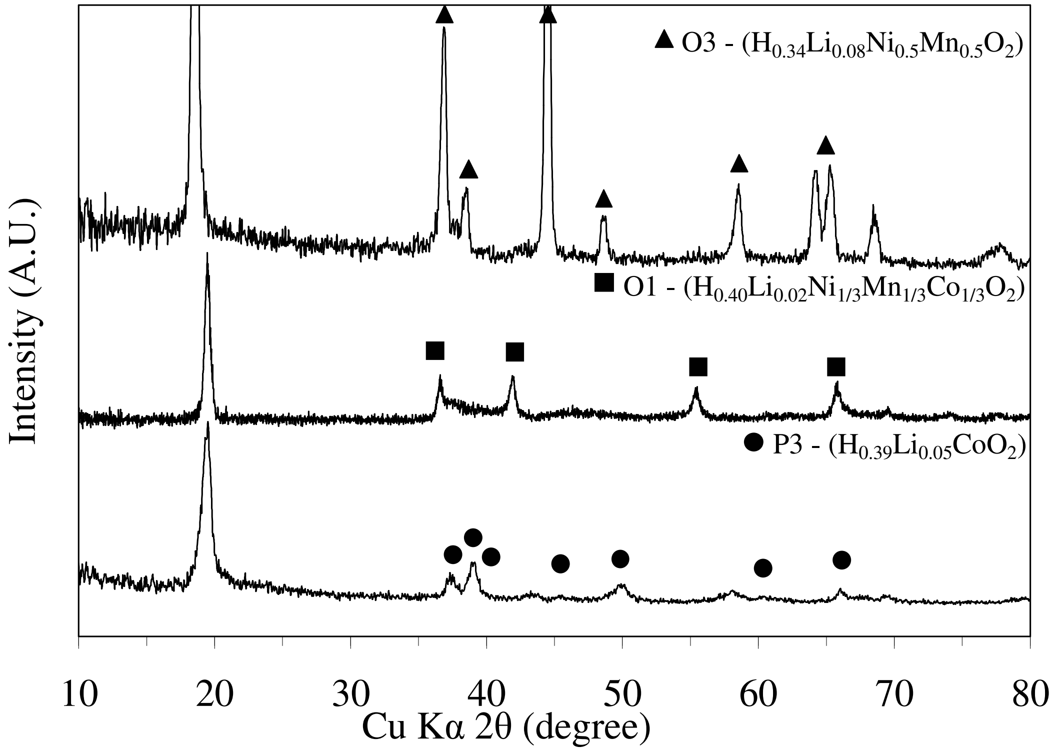

Figure 6.20: Comparison of the XRD patterns of the delithiated $H_{0.34}Li_{0.08}Ni_{0.5}Mn_{0.5}O_2$, $H_{0.40}Li_{0.02}Ni_{1/3}Mn_{1/3}Co_{1/3}O_2$, and $H_{0.39}Li_{0.05}CoO_2$, revealing their respective O3, O1, and P3-type structures.

The uptake of hydrogen in the case of $Li_{1-x}CoO_2$ was supplemented by TGA and the results are given in Figure 6.21 where the observed weight loss of the cathode system is plotted as a function of heating temperature.

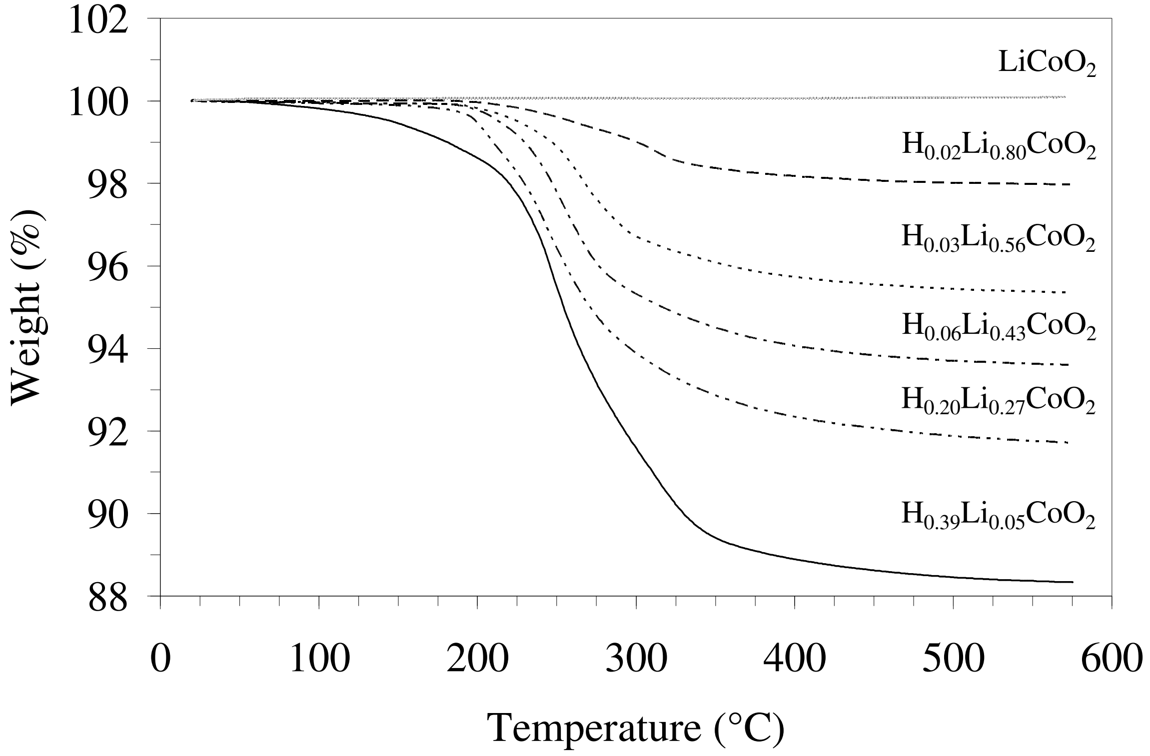

Figure 6.21: TGA plot of chemically delithiated $Li_{1-x}CoO_2$ system.

Again, as detailed in Section 6.1.3, generally assuming the final products after TGA to be (1-*x*)$LiCoO_2$ and (*x*/3)Co_3O_4 where 1-*x* is the lithium content of the respective $Li_{1-x}CoO_2$ samples, the observed weight loss agrees well with the expected weight loss for the formulas with hydrogen in the lattice rather than with the expected weight loss for the formulas with a loss of oxygen from the lattice for the same oxidation state of cobalt as presented in Table 6.5. This data reinforce the fact that hydrogen is being inserted into the $Li_{1-x}CoO_2$ lattice rather than experiencing a loss of oxygen. Again, as was previously noted, it is difficult to calculate the expected weight loss for manganese containing compounds because the final products, after undergoing TGA, are a complex mix of two or more phases and therefore TGA data for $Li_{1-x}Ni_{0.5}Mn_{0.5}O_2$ and $Li_{1-x}Ni_{1/3}Mn_{1/3}Co_{1/3}O_2$ are not presented here.

Table 6.5: TGA data for the $Li_{1-x}CoO_2$ system.

Composition	Final Product(s)	Expected weight loss (%)	Measured weight loss (%)
$LiCoO_2$	$LiCoO_2$	0.0	0.0
$H_{0.02}Li_{0.80}CoO_2$	$(0.80)LiCoO_2 + (0.20/3)Co_3O_4$	2.0	2.2
$H_{0.03}Li_{0.56}CoO_2$	$(0.56)LiCoO_2 + (0.44/3)Co_3O_4$	4.6	5.0
$H_{0.06}Li_{0.43}CoO_2$	$(0.43)LiCoO_2 + (0.57/3)Co_3O_4$	6.4	6.5
$H_{0.20}Li_{0.27}CoO_2$	$(0.27)LiCoO_2 + (0.73/3)Co_3O_4$	8.6	8.2
$H_{0.39}Li_{0.05}CoO_2$	$(0.05)LiCoO_2 + (0.95/3)Co_3O_4$	11.5	11.6

As discussed in Section 6.1.3, significant levels of proton uptake may or may not occur in the case of actual lithium ion cells since it is thought that a substantial amount of protons are generated in the non-aqueous solution used for the delithiation reaction. It is possible that acetonitrile might decompose when exposed to a strong oxidizing agent such as NO_2BF_4 [33]. Therefore, a loss of oxygen from cathodes in actual lithium ion cells is still a possibility and only a direct determination of proton content in electrochemically charged compounds will clarify this issue.

6.2.3 Summary of Work

The O3-layered $Li_{1-x}CoO_2$, $Li_{1-x}Ni_{0.5}Mn_{0.5}O_2$, and $Li_{1-x}Ni_{1/3}Mn_{1/3}Co_{1/3}O_2$ oxide cathode systems have been synthesized and systematically characterized in order to determine whether protons are introduced into the lattice during chemical delithiation.

Chemically delithiated cathodes were obtained by stirring parent $LiCoO_2$, $LiNi_{0.5}Mn_{0.5}O_2$, and $LiNi_{1/3}Mn_{1/3}Co_{1/3}O_2$ compounds with the NO_2BF_4 oxidizer in a non-aqueous acetonitrile medium. PGAA, a novel, non-destructive, nuclear technique was then utilized to directly determine the hydrogen content present in each delithiated sample.

It has been shown that the $Li_{1-x}CoO_2$, $Li_{1-x}Ni_{0.5}Mn_{0.5}O_2$, and $Li_{1-x}Ni_{1/3}Mn_{1/3}Co_{1/3}O_2$ systems show a significant amount of proton insertion during deep chemical charging ($1-x < 0.5$). It is thought that the proton uptake occurs in order to alleviate the chemical instability that occurs during deep charging which in turn could be related to the position of the transition metal bands relative to the top of the O^{2-}:2p band. This may or may not be the case in actual lithium ion cells as it is anticipated that there are fewer protons (if any) available in the electrolyte medium as compared to the acetonitrile environment the cathode samples are exposed to during the chemical extraction process. Similar studies on other cathode materials will help to further understand their capacity limitations as PGAA has been shown to be a useful tool for the direct quantitative measurement of proton content in chemically delithiated lithium ion battery cathodes.

6.3 Systematic Hydrogen Determination in High Capacity Layered $Li[Li_{0.17}Mn_{0.33}Co_{0.5-y}Ni_y]O_2$

During this investigation, special attention was paid to the high capacity oxide cathodes that are formed from solid solutions between layered $LiMO_2$ (M = $Mn_{0.5}Ni_{0.5}$, [17, 135-138] Co, [139, 140] and Ni [141, 142]) and layered Li_2MnO_3. These compounds are being intensively pursued as some of them exhibit high capacities of around 250 mAh g^{-1} and can be manufactured at a lower cost compared to $LiCoO_2$. Layered Li_2MnO_3 has the same O3-type structure as $LiCoO_2$ but with one-third of the transition metal ion sites occupied by lithium ions in the transition metal layer as $Li[Li_{1/3}Mn_{2/3}]O_2$ [143].

The discharge capacities of the above mentioned solid solution cathodes are often much higher than the theoretical capacity values expected based on the initial oxidation states of Mn, Co, and Ni. Also, the first charge profile is accompanied by an irreversible voltage plateau around 4.6 V, which has been confirmed from both *in-situ* X-ray diffraction [19] and differential electrochemical mass spectrometry studies [137] to be due to an irreversible loss of oxygen from the lattice for charging involving oxidation beyond the formal oxidation states of Mn^{4+}, Ni^{4+}, and Co^{4+}. The oxygen loss leads to a lowering of the oxidation states of transition metal ions correspondingly at the end of first discharge, which facilitates a higher reversible capacity in subsequent cycles [143].

During this study, a new series of high capacity O3-type cathodes $Li[Li_{0.17}Mn_{0.33}Co_{0.5-y}Ni_y]O_2$ ($0 \leq y \leq 0.5$) belonging to a solid solution series between $Li[Li_{1/3}Mn_{2/3}]O_2$ and $LiCo_{1-z}Ni_zO_2$ were structurally and chemically characterized in an effort to better understand their performance. Figure 6.22 indicates the y values of the compositions investigated in the solid solution series $Li[Li_{0.17}Mn_{0.33}Co_{0.5-y}Ni_y]O_2$ ($0 \leq y \leq 0.5$). While the $Li[Li_{1/3}Mn_{2/3}]O_2$ and $LiCo_{1-z}Ni_zO_2$ contents in the solid solution are kept at 1:1 (50 mol% $Li[Li_{1/3}Mn_{2/3}]O_2$ and 50 mol% $LiCo_{1-z}Ni_zO_2$), the Ni content z in $LiCo_{1-z}Ni_zO_2$ is varied from 0.0 to 1.0, which translates into a variation of y from 0.0 to 0.5 in $Li[Li_{0.17}Mn_{0.33}Co_{0.5-y}Ni_y]O_2$. With an aim to understand the variations in electrochemical properties as a function of Ni content, focus was placed on the chemical and structural characterization of the samples obtained by chemically extracting lithium with an oxidizer NO_2BF_4 in acetonitrile medium. The structural and chemical data are used to explain the observed differences in electrochemical properties as Ni content is varied. The samples analyzed during this study were provided to the author by Mr. Arunkumar.

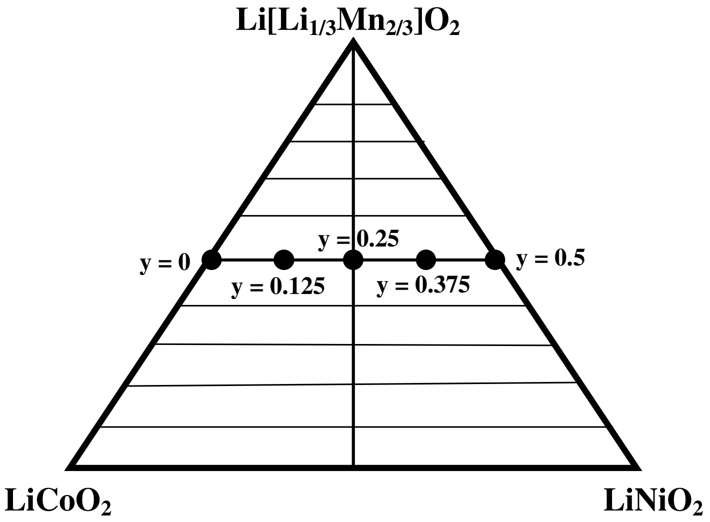

Figure 6.22: Phase diagram of the $Li[Li_{1/3}Mn_{2/3}]O_2$-$LiCoO_2$-$LiNiO_2$ system. The compositions studied in the $Li[Li_{0.17}Mn_{0.33}Co_{0.5-y}Ni_y]O_2$ ($0 \leq y \leq 0.5$) system are indicated by closed circles [143].

6.3.1 Experimental

The $Li[Li_{0.17}Mn_{0.33}Co_{0.5-y}Ni_y]O_2$ ($0 \leq y \leq 0.5$) samples were synthesized by co-precipitation where de-ionized water containing required quantities of manganese, nickel, and cobalt acetates were slowly added to a KOH solution, followed by washing, overnight drying, firing the with a required amount of $LiOH{\cdot}H_2O$ at 900 °C for 12 h in air, and quenching into liquid nitrogen. Chemical extraction of lithium was carried out by stirring parent $Li[Li_{0.17}Mn_{0.33}Co_{0.5-y}Ni_y]O_2$ powders with an acetonitrile solution of the oxidizer NO_2BF_4 for 2 days under argon atmosphere using a Schlenk line, followed by washing the products with acetonitrile [8, 33].

The lithium contents in the parent and chemically delithiated samples were determined by AAS, the average oxidation state of the transition metal ions in the parent and delithiated samples was determined by permanganate titration, and the hydrogen content was directly measured by PGAA. As discussed above, significant levels of hydrogen uptake could be generated from an ion exchange of Li^+ ions by H^+ ions that could be produced by an oxidation of acetonitrile by the powerful oxidizer NO_2BF_4 during chemical delithiation. The PGAA measurements were carried out by irradiating the samples for 2 h at a reactor power of 950 kW. These measurements were performed after the PGAA facility's recent rearrangement and characterization.

6.3.2 Results and Discussion

Table 6.6 gives the observed compositions of the delithiated samples that were calculated based on the experimentally determined hydrogen content, lithium content, and oxidation state values. The first charge and discharge capacities for all the samples are also revealed in Table 6.6; their significance will be discussed later.

During delithiation small amounts of hydrogen were inserted into the Li plane as detected by PGAA. The presence of hydrogen is due to an ion exchange of Li^+ ions by H^+ ions that are generated by an oxidation of acetonitrile by the powerful oxidizer NO_2BF_4 [33] as has been discussed in previous sections. It should be noted that the observed compositions, based on the experimentally determined lithium contents and the average oxidation state of the transition metal ions for each of the parent samples, gave higher nickel contents than expected for the nominal compositions of the form $Li[Li_{0.17}Mn_{0.33}Co_{0.5-y}Ni_y]O_2$. As calculated by Arunkumar *et al.* (2007) [143], the oxidation state values of Ni based on the experimentally observed compositions assuming Mn^{4+}, Co^{3+}, and Li^+ are significantly lower (2.54+ to 2.62+) than the theoretically expected oxidation state of 3+ based on the nominal composition. Due to difficulties associated with the stabilization of Ni^{3+}, the observed lithium content decreases with increasing Ni content resulting from a reduction of Ni^{3+} to Ni^{2+} and subsequent volatilization of lithium during synthesis at 900 ^{o}C.

Table 6.6: Observed chemical compositions and electrochemical data of chemically delithiated $Li[Li_{0.17}Mn_{0.33}Co_{0.5-y}Ni_{y}]O_2$ ($0 \leq y \leq 0.5$) samples [143].

H content (± 0.02)	Li content (± 0.02)	M^{n+} (± 0.02)	Oxygen content[a]	Observed composition	First charge capacity[b] (mAh g^{-1})			First discharge capacity (mAh g^{-1})
					A	B	Total (A+B)	
0.18	0.21	3.53	1.66	$Li_{0.04}H_{0.18}[Li_{0.17}Mn_{0.33}Co_{0.5}]O_{1.66}$	100	233	333	269
0.15	0.23	3.56	1.72	$Li_{0.09}H_{0.15}[Li_{0.14}Mn_{0.34}Co_{0.39}Ni_{0.13}]O_{1.72}$	135	181	316	233
0.18	0.17	3.65	1.78	$Li_{0.05}H_{0.18}[Li_{0.12}Mn_{0.36}Co_{0.26}Ni_{0.26}]O_{1.78}$	150	155	305	205
0.18	0.17	3.70	1.84	$Li_{0.07}H_{0.18}[Li_{0.10}Mn_{0.36}Co_{0.13}Ni_{0.41}]O_{1.84}$	185	92	277	208
0.15	0.20	3.75	1.90	$Li_{0.12}H_{0.15}[Li_{0.08}Mn_{0.37}Ni_{0.55}]O_{1.90}$	234	0[c]	234	194

[a] As measured by application of the charge neutrality principle using Li content, H content, and oxidation state data.

[b] Regions A and B correspond to the initial sloping region A and the plateau region B as marked in Figure 6.23.

[c] The sample does not show a clearly recognizable plateau region.

Further, application of the charge neutrality principle utilizing the Li contents, H contents, and oxidation state indicates that there is a loss of oxygen from the lattice of the various cathodes as presented in Table 6.6. The amount of oxygen lost from the lattice decreases with increasing Ni content. This was found to be an interesting feature since it was seen from electrochemical studies performed on these materials by Arunkumar *et al.* (2007) [143], that there exists a correlation between the amount of oxygen lost from the system and the measured levels of the first cycle charge/discharge capacities.

Figure 6.23 compares the first charge-discharge profiles of the $Li[Li_{0.17}Mn_{0.33}Co_{0.5-y}Ni_y]O_2$ ($0 \leq y \leq 0.5$) samples as measured by Arunkumar *et al.* (2007) [143]. Two distinct regions, A and B, respectively, as indicated and separated by a dashed vertical line, are exhibited during the first charge. In each case this transition begins to occur at a charge voltage of around 4.6 V. A clear transition is not visible in the $y = 0.5$ sample and thus no indicator is given. The initial region (A) corresponds to the oxidation of the transition metal ions to 4+ and the second region (B) is associated to the oxidation of the O^{2-} ions and an irreversible loss of oxygen from the lattice as previously mentioned [17, 19, 135-142].

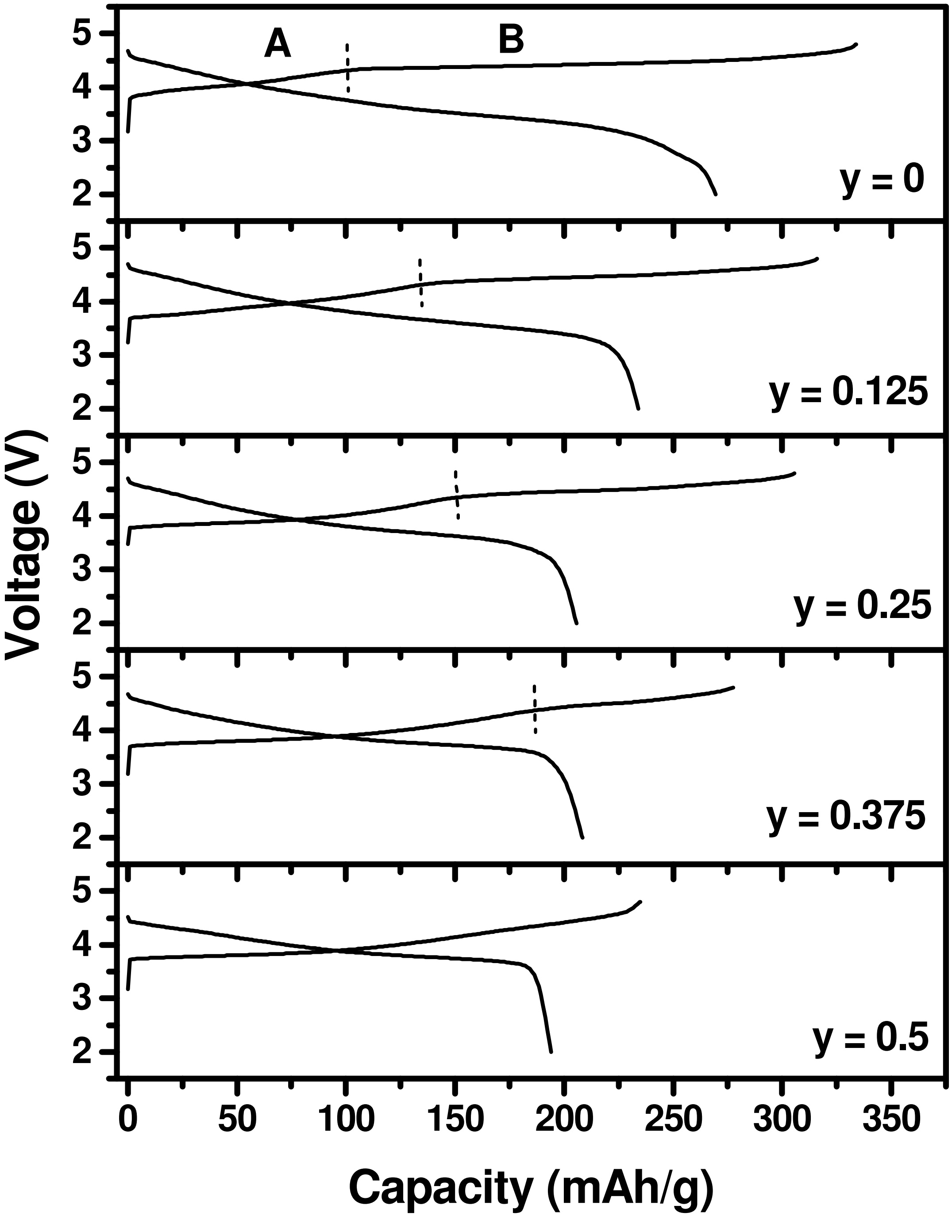

Figure 6.23: Comparison of the first charge-discharge profiles (recorded at 12.5 mA g^{-1} between 2.0 – 4.8 V) of layered $Li[Li_{0.17}Mn_{0.33}Co_{0.5-y}Ni_y]O_2$ ($0 \leq y \leq 0.5$). The dashed vertical lines separate the initial sloping region A from the plateau region B [143].

Table 6.6 compares the first charge capacity values in the two plateau regions A and B, respectively, the total first charge capacity (region A + B), and the first discharge capacity for all the samples. Region A increases with increasing Ni content due to an increased amount of Ni^{2+} and its subsequent oxidation to Ni^{4+} during the first charge. However, it is apparent that the first charge profiles in plateau region B and the first discharge capacity decrease with increasing nickel content. The decrease in the discharge capacity with increasing Ni content is due to a decrease in the lithium content in the transition metal layer and a consequent decrease in the amount of oxygen irreversibly lost during the first charge as indicated by a structural and chemical characterization of the chemically delithiated samples (Table 6.6). The decreasing amount of oxygen loss is consistent with the decreasing first cycle charge/discharge capacity levels.

The decreasing levels of oxygen loss with increasing amounts of nickel could be understood by a mechanism proposed by Armstrong *et al.* (2006) [137] for the similarly structured $Li[Li_{0.2}Mn_{0.6}Ni_{0.2}]O_2$ system, a solid solution between $Li[Li_{1/3}Mn_{2/3}]O_2$ and $LiNi_{0.5}Mn_{0.5}O_2$, based on neutron diffraction studies. It is suggested that as oxygen is lost from the particle surface, it is accompanied by a migration of Li^+ ions from 3b octahedral sites in the transition metal layer into the 3a octahedral sites in the lithium layer. This migration generates cation vacancies in the transition metal layer that are subsequently filled by a cooperative displacement and diffusion of transition metal ions from the surface to the bulk of the particle resulting in the formation of a rearranged layered structure in which the 3b octahedral sites in the transition metal layer are occupied exclusively by the transition metal ions.

Based on the hypothesis detailed above, the evolution of oxygen from the lattice should cease when all the Li^+ ion vacancies generated in the transition metal layer (3b sites) are filled by the transition metal ions diffusing from the surface to the bulk. Thus, one would expect the limiting (or lowest) oxygen content value in the delithiated sample to be twice that of the transition metal ion content or the maximum amount of oxygen loss from the lattice to be twice the amount of lithium in the transition metal layer [143].

Based on the mechanism proposed by Armstrong *et al.* (2006) [137], Table 6.7 presents the calculated limiting oxygen content values along with the experimentally observed chemical compositions after rearrangement to a fully close-packed oxygen lattice (*i.e.* no oxygen vacancies). The calculated limiting oxygen content ($2-\delta$) values are in close agreement with the observed oxygen content values (before cation rearrangement) in the delithiated samples particularly in the case of samples with low Ni content. The slightly larger observed oxygen content values (or smaller amount of oxygen loss), as compared to the calculated value, in the samples containing more Ni could be due to the presence of a significant amount of Ni^{2+} ions in the lithium planes of the undelithiated parent samples due to a high degree of cation disorder and the consequent changes in the electronic environment and lithium and oxygen mobility [143].

Interestingly, despite the same transition metal ion content in the nominal compositions $Li[Li_{0.17}Mn_{0.33}Co_{0.5-y}Ni_y]O_2$ ($0 \leq y \leq 0.5$), both the calculated and observed amounts of oxygen loss from the lattice in Table 6.7 decrease with increasing Ni content. This is due to a volatilization of lithium during the synthesis of the parent samples and a consequent increase in the transition metal ion to lithium ratio in the experimentally determined parent compositions as seen in Table 6.6. Additionally, the decrease in the amount of oxygen loss with increasing Ni content accounts for the decrease in the plateau region B in Figure 6.23 as well as the total first charge and discharge capacity, respectively (Table 6.6). A decrease in the irreversible loss of oxygen during the first charge results in a lowering of the charge and discharge capacities [143].

Table 6.7: Chemical analysis data of chemically delithiated $Li[Li_{0.17}Mn_{0.33}Co_{0.5-y}Ni_{y}]O_2$ samples [143].

Observed parent composition	Observed composition after chemical delithiation[a]		M^{n+}	Limiting oxygen content $(2-\delta)$[b]
	Before rearrangement	After rearrangement		
$Li[Li_{0.17}Mn_{0.33}Co_{0.5}]O_2$	$Li_{0.04}H_{0.18}[Li_{0.17}Mn_{0.33}Co_{0.5}]O_{1.66}$	$Li_{0.25}H_{0.22}[Mn_{0.4}Co_{0.6}]O_2$	3.53	1.66
$Li[Li_{0.14}Mn_{0.34}Co_{0.39}Ni_{0.13}]O_2$	$Li_{0.09}H_{0.15}[Li_{0.14}Mn_{0.34}Co_{0.39}Ni_{0.13}]O_{1.72}$	$Li_{0.27}H_{0.17}[Mn_{0.40}Co_{0.45}Ni_{0.15}]O_2$	3.56	1.72
$Li[Li_{0.12}Mn_{0.36}Co_{0.26}Ni_{0.26}]O_2$	$Li_{0.05}H_{0.18}[Li_{0.12}Mn_{0.36}Co_{0.26}Ni_{0.26}]O_{1.78}$	$Li_{0.18}H_{0.20}[Li_{0.01}Mn_{0.41}Co_{0.29}Ni_{0.29}]O_2$	3.65	1.76
$Li[Li_{0.10}Mn_{0.36}Co_{0.13}Ni_{0.41}]O_2$	$Li_{0.07}H_{0.18}[Li_{0.10}Mn_{0.36}Co_{0.13}Ni_{0.41}]O_{1.84}$	$Li_{0.16}H_{0.20}[Li_{0.02}Mn_{0.39}Co_{0.14}Ni_{0.45}]O_2$	3.70	1.80
$Li[Li_{0.08}Mn_{0.37}Ni_{0.55}]O_2$	$Li_{0.12}H_{0.15}[Li_{0.08}Mn_{0.37}Ni_{0.55}]O_{1.90}$	$Li_{0.18}H_{0.16}[Li_{0.03}Mn_{0.39}Ni_{0.58}]O_2$	3.75	1.84

[a] Determined based on the experimentally observed lithium and proton contents and oxidation state values.

[b] Calculated based on the maximum amount of oxygen the sample could lose.

6.3.3 Summary of Work

Layered $Li[Li_{0.17}Mn_{0.33}Co_{0.5-y}Ni_y]O_2$ cathodes with $0 \leq y \leq 0.5$ have been synthesized and characterized as cathode materials for lithium ion batteries. The charge and discharge capacities decrease with increasing Ni content due to a decrease in the amount of oxygen loss during the first charge, as indicated by the characterization of the chemically delithiated samples and calculations based on initial lithium contents and structural rearrangements during charge. While $Li[Li_{0.17}Mn_{0.33}Co_{0.5}]O_2$ offers a high discharge capacity of 269 mAh g^{-1}, $Li[Li_{0.17}Mn_{0.33}Ni_{0.5}]O_2$ exhibits a much lower capacity of 194 mAh g^{-1}. The study shows that the irreversible oxygen loss from the lattice and the reversible capacity values in the subsequent cycles could be tuned by appropriate choice of transition metal ions and contents as well as the lithium content present in the parent material [143].

Further, the data suggests a correlation between proton insertion and/or oxygen loss and the electrochemical nature of the transition metal ions present in the lattice. For example, when comparing the complex, lithium-rich layered oxide solid solution systems $Li[Li_{0.17}Mn_{0.33}Co_{0.5}]O_2$ and $Li[Li_{0.17}Mn_{0.33}Ni_{0.5}]O_2$, the only difference is the replacement of Co with Ni. While each system shows almost the same level of proton insertion, the Co containing compound shows a much larger loss of oxygen. The differences could be related to the position of the transition metal ion $M^{n+/(n+1)+}$:3d band relative to the top of the O^{2-}:2p band and the introduction of a significant amount of holes into the O^{2-}:2p band at deep lithium extraction. Significant overlap of the $Co^{3+/4+}$:3d band with the top of the O^{2-} 2p band could lead to an oxidation of the O^{2-} ions during deep lithium extraction. Moreover, the complex lithium-rich layered oxide solid solutions such as $Li[Li_{0.17}Mn_{0.33}Co_{0.5-y}Ni_y]O_2$ $(0 \leq y \leq 0.5)$ are known to exhibit a loss of oxygen at deep electrochemical charging during first charge as indicated by electrochemical studies as they involve oxidation beyond 4+ [137]. The oxygen loss in the first cycle leads to a realization of high capacities of 250 mAh g^{-1} in the subsequent cycles. The oxygen loss found in the chemically delithiated samples by way of this investigation is consistent with these prior findings [137].

Chapter 7: Conclusions and Recommendations

The primary objective of this investigation was to quantitatively determine the hydrogen content of various chemically delithiated oxide cathodes in a precise and accurate fashion by way of PGAA in order to assess their relative chemical stabilities. The determination of hydrogen content would identify the exact charge compensation mechanism(s) that occurs in order to accommodate the chemical instability arising during the extraction of lithium ions from the oxide cathodes and thus provide insight into the factors that limit the reversible capacity of practical lithium ion batteries. Given that hydrogen is a light element and the available techniques to precisely determine its content are limited, PGAA seemed to be a novel choice for its analysis.

However, the methodology used for the determination of hydrogen content had to first be validated. In an effort to identify prominent sources of error and observe the detection capabilities of the UT-PGAA system as it pertained to the analysis of delithiated lithium ion oxide cathodes, several proof of principle investigations were performed. In accordance, the analytical method used for the determination of hydrogen, the identified sources of error and the measures taken to reduce their impact (*e.g.* correction for cobalt spectral interference), the methodology employed for the calibration of the PGAA system, and the systematic measurement of hydrogen detection limits as a function of cobalt mass were presented here. Through these studies, it was shown that the PGAA facility at UT is suitable for use as an analytical tool for the purposes of precise and accurate detection of hydrogen.

The utilization of PGAA in combination with other, more traditional, characterization techniques has helped to develop a better understanding of the factors that may be limiting the reversible capacity values of lithium ion battery cathodes such as the differences in their chemical instability. More specifically, the possibility of hydrogen insertion into the cathode lattice during chemical delithiation has been fully investigated by way of the PGAA technique.

By way of this investigation, it was shown that the layered $LiCoO_2$ $LiNi_{0.5}Mn_{0.5}O_2$, and $LiNi_{1/3}Mn_{1/3}Co_{1/3}O_2$ cathodes, after undergoing chemical delithiation, incorporate a significant amount of hydrogen into their lattice. The $Li_{1-x}CoO_2$, $Li_{1-x}Ni_{0.5}Mn_{0.5}O_2$, and $Li_{1-x}Ni_{1/3}Mn_{1/3}Co_{1/3}O_2$ systems also show measurable levels of proton insertion during stepwise chemical charging. However, other oxide cathodes like layered $LiNiO_2$, o-$LiMnO_2$, spinel $LiMn_2O_4$, spinel $LiMn_{1.58}Ni_{0.42}O_2$, and olivine $LiFePO_4$ do not. The uptake of hydrogen occurs to alleviate the chemical instabilities that arise during deep lithium extraction and are thought to be linked to the overlap of the transition metal $M^{3+/4+}$:3d with the top of the O^{2-}:2p band.

The hydrogen is likely originating from decomposed acetonitrile that is used in conjunction with NO_2BF_4 to chemically extract lithium. It was previously theorized that oxygen loss was the primary mechanism occurring to alleviate the chemical instability associated with the respective cathodes but this investigation has clearly established the exchange of Li^+ with H^+ to be the dominate mechanism. Further, it is suggested that the differences in capacity for the respective oxide cathode materials is related to the instabilities arising during deep extraction. However, the exchange of Li^+ with H^+ may not occur in practical lithium ion cells since significant amounts of water may not be present in the electrolyte solvent. The application of PGAA to electrochemically charged oxide cathodes could settle this critical issue.

Further, layered $Li[Li_{0.17}Mn_{0.33}Co_{0.5-y}Ni_y]O_2$ $(0 \leq y \leq 0.5)$ showed significant levels of oxygen loss as calculated from the charge neutrality principle by way of the coupled PGAA, AAS, and titration data. Interestingly, the charge and discharge capacities decrease due to a reduction in the amount of oxygen loss during the first charge as $Li[Li_{0.17}Mn_{0.33}Co_{0.5}]O_2$ offers a large discharge capacity (269 mAh g^{-1}) while $Li[Li_{0.17}Mn_{0.33}Ni_{0.5}]O_2$ shows a lower capacity (194 mAh g^{-1}). Thus, it is apparent that proper tuning of lithium contents and transition metals could yield desired reversible capacity values via calculated levels of oxygen loss.

Overall, this study has helped establish a basic scientific understanding of the failure mechanisms of the lithium ion battery cathodes. However, future work with actual lithium ion cells and a comparison of the data obtained for chemically delithiated and electrochemically charged samples could help to establish a further firm understanding. Future work should include a comprehensive analysis of electrochemically charged cathodes with special attention placed on the charging and subsequent handling of the cathode to avoid sample contamination. Optimization of the cathode sample mass and geometry is important for obtaining reasonable results with PGAA and overcoming hydrogen detection limits.

This study has proven to be a unique approach to a non-trivial, multidiscipline, multivariable, realistic problem that is being intensely investigated by a number of leading groups. This type of investigative approach is the first of its kind and by way of this work has proven that PGAA is quite suitable for the nondestructive analysis of electrochemical materials. Further, PGAA at UT has proven to be a valuable instrument for analytical studies concerned with the advancement of alternative energy technologies.

Thus, with regards to improving the general usage of the TCNS-PGAA facility, future work should include a complete characterization and comparison of the neutron beam with the both the TCNS in on and off mode, respectively. This should include study of the neutron spectrum through the installment and use of a neutron time-of-flight system. Measurements should also be conducted to quantify the impact of the cold moderator on the neutron beam flux, cadmium ratio, and effective neutron temperature. The increased sensitivities as a result of a lower energy neutron spectrum could dramatically improve the detection capabilities of the UT-PGAA system.

Future work ought to include a comprehensive study of the moderator chamber's geometry and relative location in order to optimize its thermalizing ability. A complete investigation of mesitylene's impact, in terms of neutron interactions, should be undertaken in order to verify that mesitylene is indeed the most effective moderating material for the purposes of PGAA experiments. Deuterated-mesitylene, for example, might prove to be a better moderator because of deuterium's lower capture cross-section as compared to hydrogen. Further work should also be conducted in order to determine which solid mesitylene phase would be most beneficial as a cold moderator as part of the TCNS and how to best obtain that phase by way of cooling techniques and temperature control.

Improvements to the thermosyphon loop should be considered in order to verify whether or not neon is the most effective working fluid for adequately cooling the moderator. These experiments, along with the recent characterization of the reconstructed PGAA facility, would greatly enhance the analytical capabilities of the TCNS-PGAA facility and at the same time provide a baseline for future university reactor based cold neutron PGAA facilities.

Appendix A. TCNS Wire Diagram

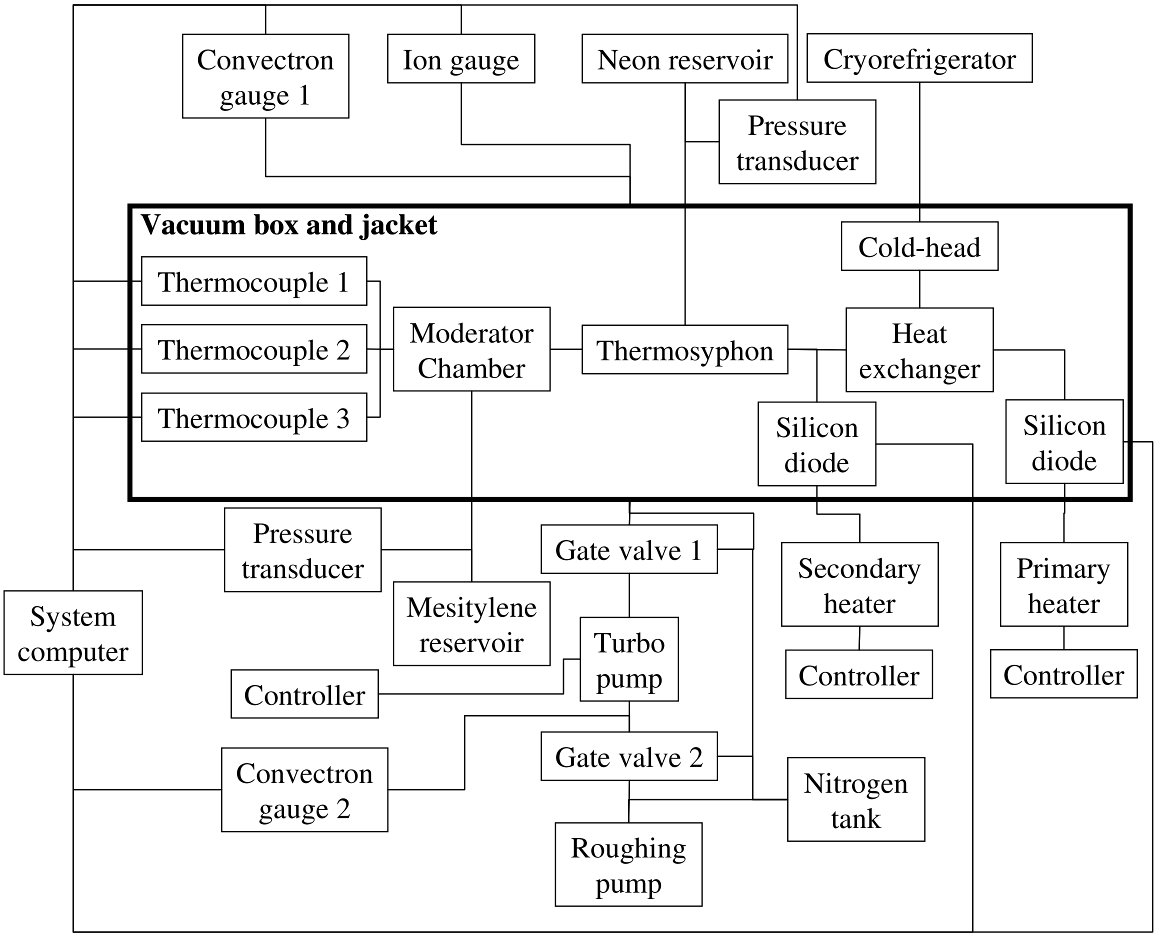
Convectron gauge 1
Ion gauge
Neon reservoir
Cryorefrigerator
Pressure transducer
Vacuum box and jacket
Cold-head
Thermocouple 1
Thermocouple 2
Thermocouple 3
Moderator Chamber
Thermosyphon
Heat exchanger
Silicon diode
Silicon diode
Pressure transducer
Gate valve 1
Secondary heater
Primary heater
System computer
Mesitylene reservoir
Turbo pump
Controller
Controller
Controller
Convectron gauge 2
Gate valve 2
Nitrogen tank
Roughing pump

Appendix B. HPGe Quality Assurance Data Sheet

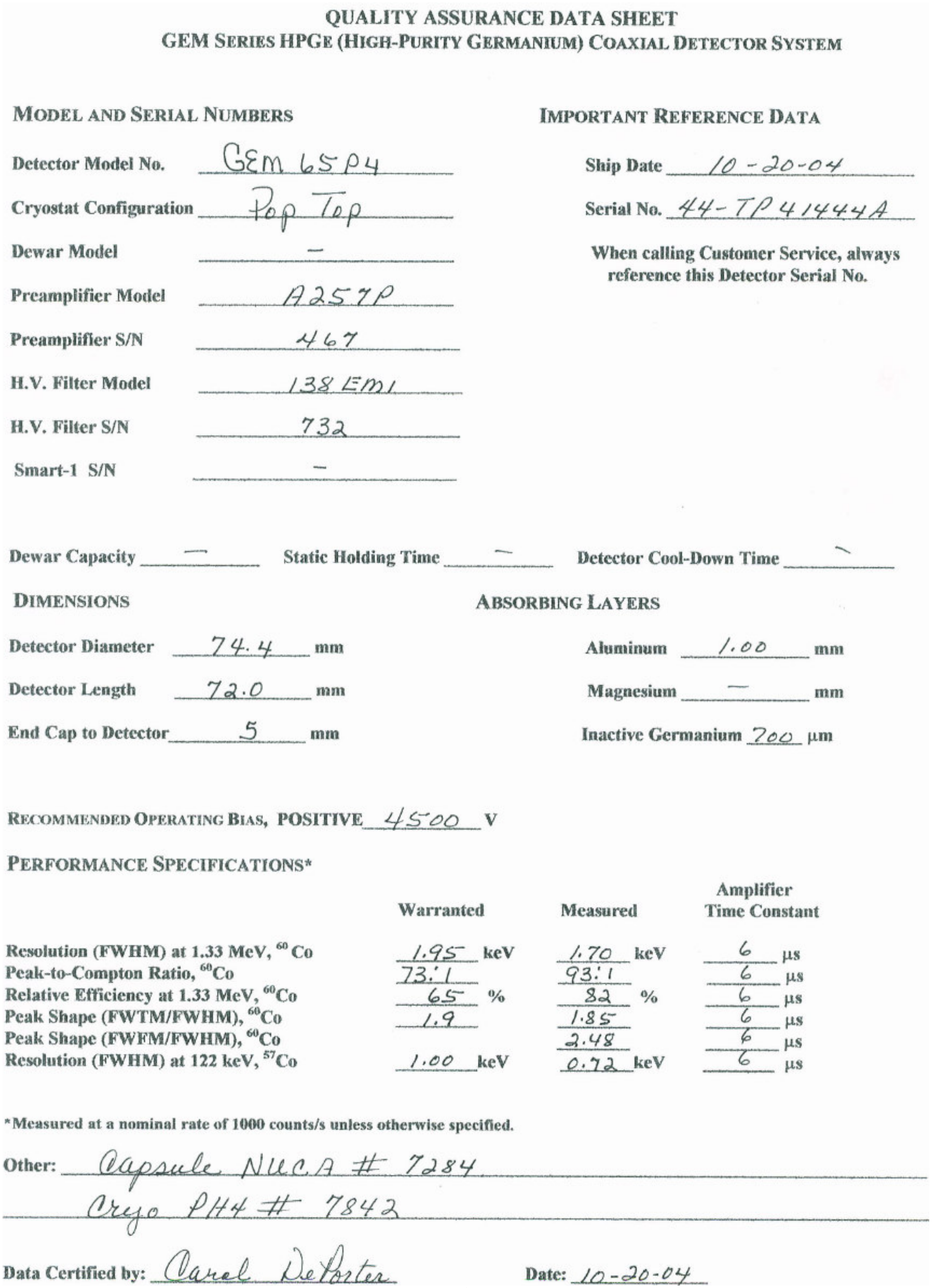

QUALITY ASSURANCE DATA SHEET
GEM SERIES HPGE (HIGH-PURITY GERMANIUM) COAXIAL DETECTOR SYSTEM

MODEL AND SERIAL NUMBERS

Detector Model No. GEM 65P4

Cryostat Configuration Pop Top

Dewar Model –

Preamplifier Model A257P

Preamplifier S/N 467

H.V. Filter Model 138EM1

H.V. Filter S/N 732

Smart-1 S/N –

IMPORTANT REFERENCE DATA

Ship Date 10-20-04

Serial No. 44-TP41444A

When calling Customer Service, always reference this Detector Serial No.

Dewar Capacity – **Static Holding Time** – **Detector Cool-Down Time** –

DIMENSIONS

Detector Diameter 74.4 **mm**

Detector Length 72.0 **mm**

End Cap to Detector 5 **mm**

ABSORBING LAYERS

Aluminum 1.00 **mm**

Magnesium – **mm**

Inactive Germanium 700 **µm**

RECOMMENDED OPERATING BIAS, POSITIVE 4500 **V**

PERFORMANCE SPECIFICATIONS*

	Warranted	Measured	Amplifier Time Constant
Resolution (FWHM) at 1.33 MeV, ^{60}Co	1.95 keV	1.70 keV	6 µs
Peak-to-Compton Ratio, ^{60}Co	73:1	93:1	6 µs
Relative Efficiency at 1.33 MeV, ^{60}Co	65 %	82 %	6 µs
Peak Shape (FWTM/FWHM), ^{60}Co	1.9	1.85	6 µs
Peak Shape (FWFM/FWHM), ^{60}Co		2.48	6 µs
Resolution (FWHM) at 122 keV, ^{57}Co	1.00 keV	0.72 keV	6 µs

*Measured at a nominal rate of 1000 counts/s unless otherwise specified.

Other: Capsule NUCA # 7284
Cryo PH4 # 7842

Data Certified by: Carol DePorter **Date:** 10-20-04

References

1. Argonne National Laboratory, Basic Research Needs for the Hydrogen Economy, in: Report of the Basic Energy Sciences Workshop on Hydrogen Production, Storage, and Use, May 13–15, 2003.

2. U.S. Department of Energy, *Hydrogen Storage "Think Tank" Report*, Office of Hydrogen, Fuel Cells and Infrastructure Technologies, Washington, D.C., March 14, 2004.

3. U.S. Department of Energy, *Annual Energy Outlook 2003*, DOE/EIA-0383, Energy Information Administration, January 2003.

4. A. Manthiram, Materials Aspects: An Overview, in: G.-A. Nazri and G. Pistoia (eds.), Science and Technology of Lithium Batteries, Kluwer Academic Publishers, Boston, 2003, pp. 3-41.

5. Lithium Battery Energy Storage (LIBES) Publication, Technological Research Association, Tokyo, 1994.

6. C. Delmas, C. Fouassier, and P. Hagenmuller, "Structural Classification and Properties of Layered Oxides," *Physica*, **99B**, 81 (1980).

7. M. Butel, L. Gautier, and C. Delmas, "Cobalt Oxyhydroxides Obtained by 'Chemie Douce' reactions: Structure and Electronic Conductivity Properties," *Solid State Ionics*, **122**, 271 (1999).

8. R. V. Chebiam, F. Prado, and A. Manthiram, "Soft Chemistry Synthesis and Characterization of Layered $Li_{1-x}Ni_{1-y}Co_yO_{2-\delta}$ ($0 \le x \le 1$ and $0 \le y \le 1$)," *Chem. Mater.*, **13**, 2951 (2001).

9. Y. Makimura and T. Ohzuku, "Lithium insertion material of $LiNi_{1/2}Mn_{1/2}O_2$ for advanced lithium-ion batteries," *J. Power Sources*, **119**, 156 (2003).

10. T. Ohzuku and Y. Makimura, "Layered Lithium Insertion Material of $LiNi_{1/2}Mn_{1/2}O_2$: A Possible Alternative to $LiCoO_2$ for Advanced Lithium-Ion Batteries," *Chem. Lett.*, **30**, 744 (2001).

11. K. M. Shaju, G. V. Subba Rao, and B. V. R. Chowdari, "Performance of Layered $Li(Ni_{1/3}Co_{1/3}Mn_{1/3})O_2$ as Cathode for Li-Ion Batteries," *Electrochim. Acta*, **48**, 145 (2002).

12. T. Ohzuku and Y. Makimura, “Layered Lithium Insertion Material of $LiCo_{1/3}Ni_{1/3}Mn_{1/3}O_2$ for Lithium-Ion Batteries,” *Chem. Lett.*, **30**, 642 (2001).

13. X. -Q. Yang, J. McBreen, W. -S. Yoon, and C. P. Grey, “Crystal Structure Changes of $LiMn_{0.5}Ni_{0.5}O_2$ Cathode Materials during Charge and Discharge Studied by Synchrotron Based In Situ XRD,” *Electrochem. Commun.*, **4**, 649 (2002).

14. W. -S. Yoon, Y. Paik, X. -Q. Yang, M. Balasubramanian, J. McBreen, and C. P. Grey, “Investigation of the Local Structure of the $LiNi_{0.5}Mn_{0.5}O_2$Cathode Material during Electrochemical Cycling by X-Ray Absorption and NMR Spectroscopy,” *Electrochem. Solid State Lett.*, **5**, A263 (2002).

15. I. Belharouak, Y. K. Sun, J. Liu, and K. Amine, “$Li(Ni_{1/3}Co_{1/3}Mn_{1/3})O_2$ as a Suitable Cathode for High Power Applications ,” *J. Power Sources*, **123**, 247 (2003).

16. W. Yoon, S. Iannopollo, C. P. Grey, D. Carlier, J. Gorman, J. Reed, and G. Ceder, “Local Structure and Cation Ordering in O3 Lithium Nickel Manganese Oxides with Stoichiometry $Li[Ni_xMn_{(2-x)/3}Li_{(1-2x)/3}]O_2$,” *Electrochem. Solid State Lett.*, **7**, A167 (2004).

17. Z. Lu, D. D. MacNeil, and J. R. Dahn, “Layered Cathode Materials $Li[Ni_xLi_{(1/3-2x/3)}Mn_{(2/3-x/3)}]O_2$ for Lithium Ion Batteries,” *Electrochem. Solid State Lett.*, **4**, A191 (2001).

18. Z. Lu, L. Y. Beaulieu, R. A. Donaberger, C. L. Thomas, and J. R. Dahn, “Synthesis, Structure, and Electrochemical Behavior of $Li[Ni_xLi_{(1/3-2x/3)}Mn_{(2/3-x/3)}]O_2$,” *J. Electrochem. Soc.*, **149**, A778 (2002).

19. Z. Lu and J. R. Dahn, “Understanding the Anomalous Capacity of $Li[Ni_xLi_{(1/3-2x/3)}Mn_{(2/3-x/3)}]O_2$ Cells using In Situ X-Ray Diffraction and Electrochemical Studies,” *J. Electrochem. Soc.*, **149**, A815 (2002).

20. J. R. Reimers and J. R. Dahn, “Electrochemical In Situ X-Ray Diffraction Studies of Lithium Intercalation in Li_xCoO_2,” *J. Electrochem. Soc.*, **139**, 2091 (1992).

21. J. Cho, J. J. Kim, T. J. Kim, and B. Park, “Zero-Strain Intercalation Cathode for Rechargeable Li-ion cell,” *Angew. Chem. Int. Ed. Engl.*, **40**, 3367 (2001).

22. A. M. Kannan, L. Rabenberg, and A. Manthiram, “High Capacity Surface Modified $LiCoO_2$ Cathodes for Lithium-ion Batteries,” *Electrochem. Solid State Lett.*, **6**, A16 (2003).

23. J. Cho, Y. J. Kim, and B. Park, “$LiCoO_2$ Cathode Material that does not Show a Phase Transition from Hexagonal to Monoclinic Phase,” *J. Electrochem. Soc.*, **148**, 1110A (2001).

24. Z. Chen and J. R. Dahn, "Effect of a ZrO_2 Coating on the Structure and Electrochemistry of Li_xCoO_2 When Cycled to 4.4 V," *Electrochem. Solid State Lett.*, **5,** A213 (2002).

25. Z. Chen and J. R. Dahn, "Studies of $LiCoO_2$ Coated with Metal Oxides," *Electrochem. Solid State Lett.*, **6**, A221 (2003).

26. R. V. Chebiam, A. M. Kannan, F. Prado, and A. Manthiram, "Comparison of the Chemical Stability of High Energy Density Cathodes of Lithium-ion Batteries," *Electrochem. Commun.*, **3**, 624 (2001).

27. S. Venkatraman, Y. Shin, and A. Manthiram, "Phase Relationships and Structural and Chemical Stabilities of Charged $Li_{1-x}CoO_{2-\delta}$ and $Li_{1-x}Ni_{0.85}Co_{0.15}O_{2-\delta}$ Cathodes," *Electrochem. Solid State Lett.*, **6**, A9 (2003).

28. S. Venkatraman and A. Manthiram, "Structural and Chemical Characterization of Layered $Li_{1-x}Ni_{1-y}Mn_yO_{2-\delta}$ ($y = 0.25$ and 0.5 and $0 \le (1-x) \le 1$) Oxides," *Chem. Mater.*, **15**, 5003 (2003).

29. S. Venkatraman and A. Manthiram, "Investigation of the Possible Incorporation of Protons into Oxide Cathodes during Chemical Delithiation," *J. Solid State Chem.***,** **177**, 4244 (2004).

30. J. Choi and A. Manthiram, "Role of Chemical and Structural Stabilities on the Electrochemical Properties of Layered $LiNi_{1/3}Mn_{1/3}Co_{1/3}O_2$ Cathodes," *J. Electrochem. Soc.*, **152**, A1714 (2005).

31. A. R. Wizansky, P. E. Rauch, and F. J. DiSalvo, "Powerful Oxidizing Agents for the Oxidative Deintercalation of Lithium from Transition-metal Oxides," *J. Solid State Chem.*, **81**, 203 (1989).

32. A. Manthiram, S. Swinnea, Z. T. Sui, H. Steinfink, and J. B. Goodenough, "The Influence of Oxygen Variation on the Crystal Structure and Phase Composition of the Superconductor $YBa_2Cu_3O_{7-x}$," *J. Am. Chem. Soc.*, **109**, 6667 (1987).

33. J. Choi, E. Alvarez, T. A. Arunkumar, and A. Manthiram, "Proton Insertion into Oxide Cathodes during Chemical Delithiation," *Electrochem. Solid State Lett.*, **9**, A241-A244 (2006).

34. A. D. Robertson and P. G. Bruce, "Mechanism of Electrochemical Activity in Li_2MnO_3," *Chem. Mater.*, **15**, 1984 (2002).

35. A. D. Robertson, A. R. Armstrong, and P. G. Bruce, Extracting Lithium Beyond Mn^{4+} in Lithium Manganese Oxides, in: Lithium Battery Discussion: Electrode Materials Conference, Arcachon, France, September 14-19, 2003, Abstract No. 57.

36. A. R. Armstrong and P. G. Bruce, “Electrochemistry Beyond Mn^{4+} in $Li_xMn_{1-y}Li_yO_2$,” *Electrochem. Solid State Lett.*, **7**, A1 (2003).

37. G. L. Molnár (ed.), Handbook of Prompt Gamma Activation Analysis with Neutron Beams, Kluwer Academic Publishers, London/Boston/Dordrecht, 2004.

38. R. L. Paul and R. M. Lindstrom, “Prompt gamma-ray activation analysis: Fundamentals and applications,” *J. Radioanal. Nucl. Chem.*, **243**, 181-189 (2000).

39. R. L. Paul, “Hydrogen Measurement by Prompt Gamma-ray Activation Analysis: A Review,” *Analyst*, **122**, 35R-41R (1997).

40. R. L. Paul and R. M. Lindstrom, “Nondestructive Measurement of Hydrogen and Other Elements by Cold Neutron Prompt Gamma-ray Activation Analysis,” *American Laboratory*, February, 15-20 (2002).

41. R. L. Paul, H. H. Chen-Mayer, and G. R. Myneni, “Determination of Hydrogen in Niobium by Cold Neutron Prompt Gamma-Ray Activation Analysis and Neutron Incoherent Scattering,” *American Institute of Physics*, **CP671**, Hydrogen in Materials Vacuum Systems (2003).

42. B. W. Wehring, J. Kim, and K. Ünlü, “Neutron Focusing System for the Texas Cold Neutron Source,” *Nucl. Instr. Meth.*, **A353**, 137 (1994).

43. H. Chen, D. F. R. Mildner, R. G. Downing, R. L. Paul, R. M. Lindstrom, C. J. Zeissler, Q. F. Xiao, and V.A. Sharov, “Prompt Gamma Activation Analysis Enhanced by a Neutron Focusing Capillary Lens,” *Nucl. Instr. Meth.*, **B95**, 107 (1995).

44. F. J. Webb, “Cold Neutron Beams from Small Low-Temperature Moderators in Reactors,” *Nucl. Sci. Eng.*, **9**, 120 (1961).

45. R. L. Paul, R. M. Lindstrom, and A. E. Heald, “Cold Neutron Prompt Gamma-Ray Activation Analysis at NIST – Recent Developments,” *J. Radioanal. Nucl. Chem.*, **215**, 63-68 (1997).

46. E. A. Mackey and J. R. D. Copley, “Scattering and Absorption Effects in Neutron Beam Activation Analysis Experiments,” *J. Radioanal. Nucl. Chem.* **167**, 127 (1993).

47. R. L. Paul and E. A. Mackey, “Neutron Scattering by Hydrogen in Cold Neutron Prompt Gamma-Activation Analysis,” *J. Radioanal. Nucl. Chem.* **181**, 321 (1993).

48 R. M. Lindstrom, R. L. Paul, D. H. Vincent, and R. R. Greenberg, “Measuring Hydrogen by Cold-Neutron Prompt-Gamma Activation-Analysis,” *J. Radioanal. Nucl. Chem.* **180**, 271 (1994).

49. E. A. Mackey, D. L. Anderson, P. J. Liposky, R. M. Lindstrom, H. Chen-Mayer, and G. P. Lamaze, "New thermal neutron prompt γ-ray activation analysis instrument at the National Institute of Standards and Technology Center for Neutron Research," *Nucl. Instr. Meth.*, **B226**, 426–440 (2004).

50. E. Alvarez II, R. M. Lindstrom, R. L. Paul, J. Cook, and I. Schröder, "Redesign of the Cold-Neutron Analytical Chemistry Instruments at NIST Center for Neutron Research," *Trans. Am. Nucl. Soc.*, **91**, 823-824 (2004).

51. R. L. Paul, "Determination of boron in materials by cold neutron prompt gamma-ray activation analysis," *Analyst*, **130**, 99-103 (2005).

52. T. Belgya, Z. Révay, B. Fazekas, I. Hejja, L. Dabolczi, G. L. Molnár, Z. Kis, J. Ostor, and G. Kaszas, The New Budapest Capture Gamma-ray Facility, in: Proc. 9th Int. Symp. Capture Gamma-ray Spectroscopy and Related Topics, Budapest, Hungary, 1996, pp. 826.

53. G. Molnár, Z. Révay, and T. Belgya, "The New Prompt Gamma-Activation Analysis Facility at Budapest," *J. Radioanal. Nucl. Chem.*, **215**, 111 (1997).

54. Zs. Révay, T. Belgya, Zs. Kasztovszky, J. L. Weil, and G. L. Molnár, "Cold neutron PGAA facility at Budapest," *Nucl. Instr. Meth.*, **B213**, 385–388 (2004).

55. H. D. Choi, R. B. Firestone, R. M. Lindstrom, G. L. Molnar, A. V. R. Reddy, V. H. Tan, C. M. Zhou, R. Paviotti-Corcuera, A. Trkov, Development of a database for prompt gamma-ray neutron activation analysis, in: Int. Conf. Nuclear Data for Science and Technology (ND2001), Tsukuba, Japan, 7 - 12 October 2001, J. Nucl. Sci. and Technol., Supplement 2, pp. 1372-1375.

56. Z. Révay, G. L. Molnár, T. Belgya, Z. Kasztovszky, and R. B. Firestone, "A New Gamma-Ray Spectrum Catalog for PGAA," *J. Radioanal. Nucl. Chem.*, **244**, 383-389 (2000).

57. G. L. Molnár, Z. Révay, T. Belgya, and R. B. Firestone, "The new prompt gamma-ray catalogue for PGAA," *Appl. Radiat. Isotopes*, **53 (4-5)**, 527-533 (2000).

58. G. L. Molnár, "Nuclear Data for Activation Analysis," *J. Radioanal. Nucl. Chem.*, **244**, 27-33 (2000).

59. K. Tompa, P. Bánki, M. Bokor, G. Lasanda, and L. Vasáros, "Diffusible and Residual Hydrogen in Amorphous Ni(Cu)–Zr–H alloys," *J. Alloys and Compounds* **350**, 52-55 (2003).

60. Z. Kasztovszky, Z. Révay, T. Belgya, and G. L. Molnár, "Nondestructive analysis of metals by PGAA at the Budapest Research Reactor," *J. Radioanal. Nucl. Chem.* **244**, 379 (2000).

61. Z. Kasztovszky, Z. Révay, G. Molnár, A. Wootsch, and Z. Paál, "Assay determination in supported Pt catalysts by prompt-gamma activation analysis (PGAA)," *Catal. Commun.*, **3**, 553 (2002).

62. S. H. Byun, G. M. Sun, and H. D. Choi, "Prompt gamma activation analysis of boron in reference materials using diffracted polychromatic neutron beam," *Nucl. Instr. Meth.*, **B213**, 535–539 (2004).

63. S. H. Byun, G. M. Sun, and H. D. Choi, "Beam Characteristics of Polychromatic Diffracted Neutrons Used for Prompt Gamma Activation Analysis," *J. Korean Nucl. Soc.*, **34**, 30-41 (2002).

64. S. H. Byun and H. D. Choi, "Design Features of a Prompt Gamma Neutron Activation Analysis System at HANARO," *J. Radioanal. Nucl. Chem.*, **244**, 413-416 (2000).

65. S. H. Byun, G. M. Sun, and H. D. Choi, "Development of a prompt gamma activation analysis facility using diffracted polychromatic neutron beam," *Nucl. Instr. Meth.*, **A487**, 521-529 (2002).

66. R. Paviotti-Corcuera and R. M. Lindstrom, Development of a Database for Prompt γ-ray Neutron Activation Analysis, in: Summary Report of the First Research Coordination Meeting IAEA Headquarters, Vienna, Austria, November 2-4, 1999, http://www-nds.iaea.org/pgaa/annex1/indc_nds_411.pdf, accessed 2004.

67. C. Yonezawa, A. Khalik, H. Wood, M. Hoshi, Y. Ito, and E. Tachikawa, "The Characteristics of the prompt Gamma-ray Analyzing System at the Neutron Beam Guides of JRR-3M," *Nucl. Instr. Meth.*, **A329**, 207-216 (1993).

68. S. Miyamoto, M. Sutoh, A. Shlomoto, S. Yamazaki, K. Nishimura, C. Yonezawa, H. Matuse, and M. Hoshi, "Determination of Boron in Animals by Reactor Neutron Induced Prompt Gamma-ray Analysis," *J. Radioanal. Nucl. Chem.*, **244**, 307-309 (2000).

69. C. Yonezawa, "Prompt gamma-ray analysis using cold and thermal guided neutron beams at JAERI," *Biol. Trace Elem. Res.*, **71-2**, 407-413 (1999).

70. K. Tanoi, H. Iikura, and T. M. Nakanishi, "Elemental Analysis in Cultured Cells, Tobacco and Grape, Treated with Aluminum," *J. Radioanal. Nucl. Chem.*, **249**, 519-522 (2001).

71. C. Yonezawa, H. Matsue, K. McKay, and P. Povinec, "Analysis of Marine Samples by Neutron-induced Prompt Gamma-ray Technique and ICP-MS," *J. Radioanal. Nucl. Chem.*, **248**, 719-725 (2001).

72. Y. Oura, S. Enomoto, H. Nakahara, H. Matsue, and C. Yonezawa, "Prompt Gamma-ray Analysis of Rats," *J. Radioanal. Nucl. Chem.*, **244**, 311-315 (2000).

73. M. Crittin, J. Kern, and J. L. Schenker, "The new prompt gamma-ray activation facility at the Paul Scherrer Institute, Switzerland," *Nucl. Instr. Meth.*, **A449**, 221-236 (2000).

74. S. Baechler, P. Kudejova, J. Jolie, J. L. Schenker, and N. Stritt, "Prompt Gamma-ray Activation Analysis for Determination of Boron in Aqueous Solutions," *Nucl. Instr. Meth.*, **A488**, 410-418 (2002).

75. M. Crittin, J. Jolie, J. Kern, S. J. Mannanal, and R. Schwarzbach, "Hydrogen detection by prompt gamma-ray activation analysis (PGAA)," *J. Alloys and Compounds*, **253-254**, 156-157 (1997).

76. F. Krug, T. Schober, R. Paul, and T. Springer, "Investigation of the Hydrogen Uptake of Doped $SrCeO_3$ by TEM, Thermogravimetry, and Cold Neutron Prompt Gamma Activation Analysis (CNPGAA)," *Solid State Ionics*, **77**, 185-188 (1995).

77. R. L. Paul, H. M. Privett, R. M. Lindstrom, W. J. Richards, and R. R. Greenberg, "Determination of Hydrogen in Titanium Alloys by Cold Neutron Prompt Gamma Activation Analysis," *Met. Mater. Trans.*, **27A**, 3682 (1996).

78. C. Y. Jones and B. H. Toby, "Cold Neutron Prompt-Gamma Activation Analysis of Hydrogen in H-ZSM-5," *Trans. Am. Nucl. Soc.*, **87**, 482 (2002).

79. R. B. Firestone and V. Zerkin, PGAA Database Viewer, IAEA, http://www-nds.iaea.org/pgaa/pgaa7/index.html, accessed 2006

80. B. W. Wehring and T. L. Bauer, "Status of the University of Texas Research Reactor Program," *Trans. Am. Nucl. Soc.*, **64**, 242 (1991).

81. D. S. O'Kelly, D. J. O'Kelly, W. S. Pennington, and T. Tipping, Minimizing Personnel Radiation Dose During Major Reactor Repairs at The University of Texas at Austin, in: International Topical Meeting on Operating Nuclear Facility Safety, Embedded Topical Meeting, ANS Winter Meeting, Washington, D.C., November 14-18, 2004.

82. K. Ünlü, C. Ríos-Martínez, and B. W. Wehring, "Prompt Gamma Activation Analysis with the Texas Cold Neutron Source," *J. Radioanal. Nucl. Chem.*, **193**, 145-154 (1995).

83. K. Ünlü, T. Emoto, and B. W. Wehring, "Design Features of the Texas Cold Neutron Source," *Trans. Am. Nucl. Soc.*, **65**, 134 (1992).

84. A. R. Köymen, K. Ünlü, F. M. Jacobsen, S. Göktepeli, and B. W. Wehring, "Development of Texas intense positron source," *Nucl. Instr. Meth.*, **A422**, 479-483 (1999).

85. K. Ünlü and B. W. Wehring, "Neutron depth profiling at the University of Texas," *Nucl. Instr. Meth.*, **A353**, 402-405 (1994).

86. S. M. Whitney, R. G. Downing, and S. R. Biegalski, "Advancement of Light-Element Neutron Depth Profiling at the University of Texas," *J. Radioanal. Nucl. Chem.*, in press (2006).

87. S. Whitney, E. Alvarez, D. Haas, K. Jackman, S. Wilson, and S. Biegalski, "The Design of a Fast Neutron PGAA Facility at The University of Texas at Austin," *J. Radioanal. Nucl. Chem.*, in press (2006).

88. D. J. Dorsey and W. S. Charlton, "Recent developments and applications for the University of Texas Thermal Neutron Imaging Facility," *Appl. Radiat. Isotopes*, **61**, 525–528 (2004).

89. S. O'Kelly, D. Beller, and W. Charlton, "Accelerator Driven Subcritical System Experiments at The University of Texas," *Trans. Am. Nucl. Soc.*, **93**, 903 (2005).

90. K. Ünlü, C. Ríos-Martínez, and B. W. Wehring, "The University of Texas Cold Neutron Source," *Nucl. Instr. Meth.*, **A353**, 397-401 (1994).

91. E. Alvarez II, "Characterization of the University of Texas at Austin Nuclear Engineering Teaching Laboratory Beam Port 3 Texas Cold Neutron Source – Prompt Gamma-ray Activation Analysis Facility," Masters Thesis, The University of Texas at Austin (2005).

92. Zs. Révay, R. K. Harrison, E. Alvarez, S. R. Biegalski, and S. Landsberger, "Construction and characterization of the redesigned PGAA facility at the University of Texas at Austin," *Nucl. Instr. Meth.*, **A577**, 611–618 (2007).

93. E. A. Mackey, R. L. Paul, R. M. Lindstrom, D. L. Anderson, and R. R. Greenberg, "Sources of uncertainties in prompt gamma activation analysis," *J. Radioanal. Nucl. Chem.*, **265**, 273-281 (2005).

94. C. Ríos-Martínez, "Prompt Gamma Activation Analysis using the Texas Cold Neutron Source," Ph.D. Dissertation, The University of Texas at Austin (1995).

95. E. Kulagin, S. Kulikov, V. Melikhov, and E. Shabalin, "Radiation effects in cold moderator materials: Experimental study of accumulation and release of chemical energy," *Nucl. Instr. Meth.*, **B215,** 181–186 (2004).

96. M. Prager, H. Grimma, and I. Natkaniec, "Rotational tunneling of methyl groups in low temperature phases of mesitylene: potentials and structural implications," *Phys. Chem. Chem. Phys.*, **7**, 2587-2593 (2005).

97. I. Natkaniec, K. Holderna-Natkaniec, J. Kalus, I. Majerz, Vibrational Spectra of Selected Methyl Derivatives of Benzene and Their Solutions as Potential Materials for Cold Moderators, in: Proc. 16th Meeting of the International Collaboration on Advanced Neutron Sources (ICANS-XVI), Düsseldorf-Neuss, Germany, May 12-15, 2003.

98. H. Conrad, W. F. Kuhs, K. Nünighoff, C. Pohl, M. Prager, Inelastic neutron scattering and spectral measurements of advanced cold moderator materials, in: Proc. 16th Meeting of the International Collaboration on Advanced Neutron Sources (ICANS-XVI), Düsseldorf-Neuss, Germany, May 12-15, 2003.

99. K. Ünlü and C. Ríos-Martínez, "Cold neutron PGAA facility developments at university research reactors in the USA," *J. Radioanal. Nucl. Chem.*, **265**, 329-338 (2005).

100. B. W. Wehring, K. Ünlü, and C. Ríos-Martínez, "Application of Cold-neutron Prompt Gamma Activation Analysis at the University of Texas Reactor," *Appl. Radiat. Isotopes*, **48**, 1343 (1997).

101. C. Ríos-Martínez, K. Ünlü, and B. W. Wehring, "Performance of the University of Texas cold-neutron prompt gamma activation analysis facility," *J. Radioanal. Nucl. Chem.*, **234**, 119 (1998).

102. S. K. Aghara, S. Venkatraman, A. Manthiram, and E. Alvarez II, "Investigation of hydrogen content in chemically delithiated lithium-ion battery cathodes using prompt gamma activation analysis," *J. Radioanal. Nucl. Chem.*, **265**, 321 (2005).

103. http://www.kingplastic.com/Products/PlastiShield.aspx

104. G. L. Molnár, Zs. Révay, and T. Belgya, "Wide energy range efficiency calibration method for Ge detectors," *Nucl. Instr. Meth.*, **A489**, 140 (2002).

105. Zs. Révay, T. Belgya, and G. L. Molnár, "Application of Hypermet-PC in PGAA," *J. Radioanal. Nucl. Chem.*, **265**, 261 (2005).

106. B. Fazekas, J. Östör, Z. Kis, G. L. Molnár, and A. Simonits, The new features of Hypermet-PC, in: G. Molnár, T. Belgya, Zs. Révay (eds.), Proc. 9th International Symposium on Capture Gamma-Ray Spectroscopy and Related Topics, Budapest, Hungary, October 8-12, Springer Verlag, Budapest/Berlin/Heidelberg, 1997, pp. 774.

107. B. Fazekas, Zs. Révay, J. Östör, T. Belgya, G. Molnár, and A. Simonits, "A new method for determination of gamma-ray spectrometer non-linearity," *Nucl. Instr. Meth. in Phys. Res.*, **A422**, 469 (1999).

108. B. Krusche, K. P. Lieb, H. Daniel, T. Von Egidy, G. Barreau, H. G. Börner, R. Brissot, C. Hofmeyr, and R. Rascher, "Gamma ray energies and ^{36}Cl level scheme from the reaction ^{35}Cl(n,γ)," *Nucl. Phys.*, **A386**, 245 (1982).

109. E. Alvarez II and S. K. Aghara, "Time Dependent Neutron Fluence Measurements at UT-NETL PGAA Facility," *Trans. Am. Nucl. Soc.*, **91**, 815-816 (2004).

110. D. J. Dorsey and W. S. Charlton, "Recent developments and applications for the University of Texas Thermal Neutron Imaging Facility," *Appl. Radiat. Isotopes*, **61**, 525 (2004).

111. S. R. Biegalski, L. Cao, D. A. Haas, and D. S. O'Kelly, "Neutron Radiography Development at The University of Texas at Austin TRIGA Reactor," *Trans. Am. Nucl. Soc.*, **93**, 880 (2005).

112. Zs. Revay, "Characterization of the wavelength spectrum of guided neutron beams," *J. Radioanal. Nucl. Chem.*, **264**, 283 (2005).

113. C. N. Grant, G. C. Lalor, and M. K. Vutchkov, "In situ Gamma spectroscopy measurement of Ar-41 during neutron activation analysis with the SLOWPOKE II reactor in Jamaica," *Health Phys.*, **87**, S68 (2004).

114. M. Stepišnik, B. Pucelj, T. Vidmar, and M. Vencelj, Analysis of the Dose-Rate Time Development, in: Proc. International Conference on Nuclear Energy for New Europe, Portorož, Slovenia, September 8-11, 2003.

115. L. A. Currie, "Limits for qualitative detection and quantitative determination. Application to radiochemistry," *Anal. Chem.*, **40**, 586-593 (1968).

116. L. A. Currie, "Nomenclature in Evaluation of Analytical Methods Including Detection and Quantification Capabilities," *Pure Appl. Chem.*, **67**, 1699-1723 (1995).

117. W. Li and J. C. Currie, "Morphology Effects on the Electrochemical Performance of $LiNi_{1-x}Co_xO_2$," *J. Electrochem. Soc.*, **144**, 2773 (1997).

118. N. Yabuuchi and T. Ohzuku, "Novel lithium insertion material of $LiCo_{1/3}Ni_{1/3}Mn_{1/3}O_2$ for advanced lithium-ion batteries," *J. Power Sources*, **119-121**, 171 (2003).

119. J. Choi and A. Manthiram, “Comparison of the Electrochemical Behaviors of Stoichiometric $LiNi_{1/3}Co_{1/3}Mn_{1/3}O_2$ and Lithium Excess $Li_{1.03}(Ni_{1/3}Co_{1/3}Mn_{1/3})_{0.97}O_2$,” *Electrochem. Solid-State Lett.*, **7**, A365 (2004).

120. J. Kim and H. Chung, “The first cycle characteristics of $Li[Ni_{1/3}Co_{1/3}Mn_{1/3}]O_2$ charged up to 4.7 V,” *Electrochim. Acta*, **49**, 937 (2004).

121. R. V. Chebiam, F. Prado, and A. Manthiram, “Comparison of the Chemical Stability of $Li_{1-x}CoO_2$ and $Li_{1-x}Ni_{0.85}Co_{0.15}O_2$ Cathodes,” *J. Solid State Chem.*, **163**, 5 (2002).

122. S. Venkatraman and A. Manthiram, “Synthesis and Characterization of P3-Type $CoO_{2-\delta}$” *Chem. Mater.*, **14**, 3907 (2002).

123. R. J. Gummow, M. M. Thackeray, W. I. F. David, and S. Hull, “Structure and electrochemistry of lithium cobalt oxide synthesized at 400°C,” *Mater. Res. Bull.*, **27**, 327 (1992).

124. R. J. Gummow, D. C. Liles, and M. M. Thackeray, “Spinel versus layered structures for lithium cobalt oxide synthesized at 400°C,” *Mater. Res. Bull.*, **28**, 235 (1993).

125. S. Choi and A. Manthiram, “Synthesis and Electrochemical Properties of $LiCo_2O_4$ Spinel Cathodes,” *J. Electrochem. Soc.*, **149**, A162 (2002).

126. S. Choi and A. Manthiram, “Chemical Synthesis and Properties of Spinel $Li_{1-x}Co_2O_{4-\delta}$,” *J. Solid State Chem.*, **164**, 332 (2002).

127. T. S. Meng, G. Ceder, C. P. Grey, W.-S. Yoon, and Y. Shao-Horn, “Understanding the Crystal Structure of Layered $LiNi_{0.5}Mn_{0.5}O_2$ by Electron Diffraction and Powder Diffraction Simulation,” *Electrochem. Solid-State Lett.*, **7**, A155 (2004).

128. J. Choi, “Crystal chemistry, chemical stability and electrochemical properties of layered oxide cathodes of lithium ion batteries,” Ph.D. Dissertation, The University of Texas at Austin (2006).

129. S. C. Sweetman (ed.), Martindale: The Complete Drug Reference, 34th ed., The Pharmaceutical Press, London, 2005.

130. A. D. Robertson and P. G. Bruce, “Overcapacity of $Li[Ni_xLi_{1/3-2x/3}Mn_{2/3-x/3}]O_2$ Electrodes,” *Electrochem. Solid-State Lett.*, **7**, A294 (2004).

131. K. Kanamura, “Anodic oxidation of nonaqueous electrolytes on cathode materials and current collectors for rechargeable lithium batteries,” *J. Power Sources*, **81-82**, 123 (1999).

132. D. Aurbach, "Review of selected electrode-solution interactions which determine the performance of Li and Li ion batteries," *J. Power Sources*, **89**, 206 (2000).

133. V. E. Henrich and P. A. Cox, in: The Surface Science of Metal Oxides, Cambridge University Press, Cambridge, 1994, pp. 288.

134. Y. Paik, C. P. Grey, C. S. Johnson, J. S. Kim, and M. M. Thackery, "Lithium and deuterium NMR studies of acid-leached layered lithium manganese oxides," *Chem. Mater.*, **14**, 5109 (2002).

135. S. H. Kang, Y. K. Sun, and K. Amine, "Electrochemical and *Ex Situ* X-Ray Study of $Li(Li_{0.2}Ni_{0.2}Mn_{0.6})O_2$ Cathode Material for Li Secondary Batteries," *Electrochem. Solid-State Lett.,* **6**, A183 (2003).

136. Y. J. Park, Y. S. Hong, X. Wu, K. S. Ryu, and S. H. Chang, "Structural investigation and electrochemical behaviour of $Li[Ni_xLi_{(1/3-2x/3)}Mn_{(2/3-x/3)}]O_2$ Compounds by a simple combustion method," *J. Power Sources,* **129**, 288 (2004).

137. A. R. Armstrong, M. Holzapfel, P. Novak, C. S. Johnson, S. Kang, M. M. Thackeray, and P. G. Bruce, "Demonstrating Oxygen Loss and Associated Structural Reorganization in the Lithium Battery Cathode $Li[Ni_{0.2}Li_{0.2}Mn_{0.6}]O_2$," *J. Am. Chem. Soc.,* **128**, 8694 (2006).

138. Y. Wu and A. Manthiram, "High Capacity, Surface-Modified Layered $Li[Li_{(1-x)/3}Mn_{(2-x)/3}Ni_{x/3}Co_{x/3}]O_2$ Cathodes with Low Irreversible Capacity Loss," *Electrochem. Solid State Lett.*, **9**, A221 (2006).

139. K. Numata, C. Sakaki, and S. Yamanaka, "Synthesis and characterization of layer structured solid solutions in the system of $LiCoO_2$–Li_2MnO_3," *Solid State Ionics,* **117**, 257 (1999).

140. Y. J. Park, X. Wu, Y. S. Hong, K. S. Ryu, and S. H. Chang, "Structural and electrochemical properties of $Li[Co_xLi_{(1/3-x/3)}Mn_{(2/3-2x/3)}]O_2$ cathode materials," *Solid State Ionics,* **175**, 305 (2004).

141. L. Zhang, H. Noguchi, and M. Yoshio, "Synthesis and electrochemical properties of layered Li–Ni–Mn–O compounds," *J. Power Sources,* **110**, 57 (2002).

142. P. S. Whitfield, S. Niketic, and I. J. Davidson, "Effects of synthesis on electrochemical, structural and physical properties of solution phases of Li_2MnO_3–$LiNi_{1-x}Co_xO_2$," *J. Power Sources,* **146**, 617 (2005).

143. T. A. Arunkumar, E. Alvarez, and A. Manthiram, "Structural, Chemical, and Electrochemical Characterization of Layered $Li[Li_{0.17}Mn_{0.33}Co_{0.5-y}Ni_y]O_2$ Cathodes," *J. Electrochem. Soc.*, **154**, A770-A775 (2007).

Vita

Emilio Alvarez II was born on January 16, 1981 in McAllen, Texas. Emilio is the first born son of Emilio and Arcelia Alvarez. He has one younger brother named Edrick Alvarez. Emilio married Daniella Peña on December 18, 2004 in Peñitas, Texas. . Emilio and his wife welcomed their twin daughters Isabella and Olivia into this world on December 21, 2006. Emilio attended elementary, junior high, and high school in La Joya, Texas. He graduated as valedictorian of his high school class and enrolled at the University of Texas at Austin in 1999. In August, 2003 he completed his Bachelor of Science in Mechanical Engineering. In September, 2003 Emilio was accepted into the Mechanical Engineering Nuclear and Radiation Engineering Program and earned his Master of Science in Engineering from the University of Texas at Austin in May, 2005. As an undergraduate Emilio worked as an intern at Applied Materials, Inc. located in Austin, Texas and as a graduate student participated in an internship at the National Institute of Standards and Technology based in Gaithersburg, Maryland.

List of publications the author has contributed to:

E. Alvarez, S. R. Biegalski, and S. Landsberger, "Methodologies for Hydrogen Determination in Metal Oxides by Prompt Gamma Activation Analysis," *Nucl. Instr. Meth. B*, in press (2007).

Zs. Révay, R. K. Harrison, E. Alvarez, S. R. Biegalski, and S. Landsberger, "Construction and characterization of the redesigned PGAA facility at the University of Texas at Austin," *Nucl. Instr. Meth.*, **A577**, 611–618 (2007).

E. Alvarez, S. R. Biegalski, and S. Landsberger, "Hydrogen Determination in Metal Oxides by Prompt Gamma Activation Analysis," *Trans. Am. Nucl. Soc.*, in press (2007).

R. K. Harrison, Zs. Révay, E. Alvarez, S. Biegalski, and S. Landsberger, "Characterization and Reduction of the Gamma–Ray Background for PGAA Applications," *Trans. Am. Nucl. Soc.*, in press (2007).

T. A. Arunkumar, E. Alvarez, and A. Manthiram, "Structural, Chemical, and Electrochemical Characterization of Layered $Li[Li_{0.17}Mn_{0.33}Co_{0.5-y}Ni_y]O_2$ Cathodes," *J. Electrochem. Soc.*, **154**, A770-A775 (2007).

S. R. Biegalski, T. C. Green, E. Alvarez, and S. Aghara, "Background characterization of The University of Texas PGAA Facility," *J. Radioanal. Nucl. Chem.*, **271**, 413–417 (2007).

S. Whitney, E. Alvarez, D. Haas, K. Jackman, S. Wilson, and S. Biegalski, "The Design of a Fast Neutron PGAA Facility at The University of Texas at Austin," *J. Radioanal. Nucl. Chem.*, in press (2006).

E. Alvarez, D. Haas, K. Jackman, S. Whitney, and S. Wilson, "Investigation, Design and Analysis of a Fast Neutron Facility on Beam Port 4 at the University of Texas MARK II TRIGA Reactor," *Trans. Am. Nucl. Soc.*, **95**, 981 (2006).

J. Choi, E. Alvarez, T. A. Arunkumar, and A. Manthiram, "Proton Insertion into Oxide Cathodes during Chemical Delithiation," *Electrochem. Solid State Lett.*, **9**, A241-A244 (2006).

S. R. Biegalski, E. Alvarez, and T. Green, "Confirmation of germanium interference with hydrogen for prompt gamma–ray activation analysis," *Nucl. Instrum. Meth.*, **B243**, 253–255 (2006).

S. K. Aghara, S. Venkatraman, A. Manthiram, and E. Alvarez II, "Investigation of hydrogen content in chemically delithiated lithium-ion battery cathodes using prompt gamma activation analysis," *J. Radioanal. Nucl. Chem.*, **265**, 321 (2005).

E. Alvarez, A. Manthiram, S. Biegalski, and S. Landsberger, “Determination of Hydrogen Content by PGAA in Lithium Ion Battery Cathode Materials,” *Trans. Am. Nucl. Soc.*, **93**, 496 (2005).

E. Alvarez II, R. M. Lindstrom, R. L. Paul, J. Cook, and I. Schröder, “Redesign of the Cold−Neutron Analytical Chemistry Instruments at NIST Center for Neutron Research,” *Trans. Am. Nucl. Soc.*, **91**, 823 (2004).

E. Alvarez II and S. K. Aghara, “Time Dependent Neutron Fluence Measurements at UT−NETL PGAA Facility,” *Trans. Am. Nucl. Soc.*, **91**, 815 (2004).

Permanent address: 953 South King Street,

La Joya, Texas 78560

This dissertation was typed by the author.